Technische Universität München
Lehrstuhl für Werkstoffkunde und Werkstoffmechanik mit
Materialprüfamt für den Maschinenbau

Finite Element Simulation of Porous Nickel-Base Superalloys on Multiple Length Scales

Thomas M. Taxer

Vollständiger Abdruck der von der Fakultät für Maschinenwesen
der Technischen Universität München
zur Erlangung des akademischen Grades eines

Doktor-Ingenieurs (Dr.-Ing.)

Vorsitzender:	Univ.-Prof. Dr.-Ing. M. Hajek
Prüfer der Dissertation:	1. Univ.-Prof. Dr. mont. habil. E. Werner
	2. Univ.-Prof. Dr.-Ing. W. Volk

Die Dissertation wurde am 05.06.2012 bei der Technischen Universität München
eingereicht und durch die Fakultät für Maschinenwesen
am 16.10.2012 angenommen.

“The value of achievement lies in the achieving.”

Albert Einstein to D. Liberson, October 28th, 1950, Einstein Archive 60-297.

Thomas Taxer

Finite Element Simulation of Porous Nickel-Base Superalloys on Multiple Length Scales

key words nickel-base superalloys, porosity, micromechanical finite element simulation, volume element model, periodic boundary conditions, sequential multiscale model, concurrent multiscale model

abstract Finely dispersed porosity within castings of nickel base superalloys is inevitable. These microstructural defects influence the mechanical properties and thus the functionality of the castings. Computed tomography studies of porous samples allowed the development of a micromechanical computer generated finite element model to quantify the effect of the porosity on the deformation behavior of the material. To use the results gained on the microscopic scale for the component layout, a so-called multiscale model was implemented in which the constitutive law is provided from micromechanical finite element models. This allows to consider local variations in the microsturcture of the material and thus enables an optimized component layout with respect to variations in the load-bearing capacity of the material.

zusammenfassung Das Auftreten fein verteilter Poren in Nickel-Basis Struckturgussbauteilen lässt sich bei deren Herstellung nicht vermeiden. Diese Fehlstellen in der Mikrostruktur des Materials beeinträchtigen die Materialeigenschaften und damit auch die Funktionalität des Bauteils. Computertomographische Untersuchungen ermöglichen eine Charakterisierung der auftretenden Porosität hinsichtlich der Volumenverteilung der Einzelporen, der räumlichen Verteilung und der Form der Poren sowie des Porenvolumenanteils. Diese Charakteristika dienen als Grundlage zur Generierung mikromechanischer Finite Elemente Modelle mit deren Hilfe das Materialverhalten in Abhängigkeit der Porosität untersucht werden kann. Um die auf der mikromechanischen Ebene gewonnenen Erkenntnisse für die Bauteilauslegung nutzbar zu machen, wird im Rahmen dieser Arbeit ein Multiskalenmodell vorgestellt. Damit können bei der Bauteilauslegung lokale Unterschiede der Porosität berücksichtigt werden.

Acknowledgment

This dissertation has been carried out at the Institute of Materials Science and Mechanics of Materials at the Technische Universität München from 2008 to 2012.
First of all I would like to thank Prof. Ewald Werner for his guidance and for providing the opportunity to do my PhD under his supervision.
I owe many thanks to the workshop and metallography staff of our institute for their support in preparing my samples as well as to Yvone Jahn for her support with organizational matters. Furthermore I would like to thank my colleagues and friends at the Institue of Materials Science and Mechanics of Material, especially Matthias Dünckelmeyer, Alexander Fillafer, Florian Hairer, Jingming Lu, Benjamin Regener, Cornelia Schwarz and Robert Wesenjak for the many discussions and their ideas and input on how to proceed with and improve my work.
An especially big **THANK YOU** to Gerwin Riedl, Jingming Lu and my wife Jamie for the great job they did proof-reading this dissertation—I know it is the most thankless job of all.

> "In the first place God made idiots. This was for practice. Then he made proof-readers." - Mark Twain, 1893.

Last but not least I would like to express my thankfulness towards MTU-Aero Engines GmbH for the financial support of my project. I especially want to thank Dr. Wilfried Smarsly for his interest in my work and the many useful discussions we had over the past four years.

Thomas Taxer Munich, November 29, 2012

Contents

List of Figures

List of Tables

List of Symbols

Parameter	Description	Unit
α	Weibull parameter	–
β	Weibull parameter	–
γ	Surface energy	$\frac{\mathrm{J}}{\mathrm{m}^2}$
δ	Infinitesimal displacement	m
$\boldsymbol{\varepsilon}$	Strain tensor	–
η	Pore density	–
η_{th}	Thermal efficiency	–
λ	Coefficient	–
μ	Attenuation coefficient	$\frac{1}{\mathrm{m}}$
	Lognormal coefficient	–
ν	Poisson ratio	–
σ	Lognormal coefficient	–
σ_{y0}	Initial yield stress	$\frac{\mathrm{N}}{\mathrm{mm}^2}$
$\boldsymbol{\sigma}$	Stress tensor	$\frac{\mathrm{N}}{\mathrm{mm}^2}$
Ω_{m}	Micromechanical domain in reference state	m^3
Ω_{0m}	Micromechanical domain in current state	m^3
a	Major half axis dimension of Lame curve	m
b	Minor half axis dimension of Lame curve	m
$\mathbf{b}$	Base vector of volume element model	–
$\mathbf{b}_{\mathrm{hom}}$	Vector of homogenized stresses	$\frac{\mathrm{N}}{\mathrm{mm}^2}$
d	Pore distance	m
d_{min}	Nearest neighbor distance	m
$\mathbf{e}_i$	Cartesian unit vector	–
$\mathbf{f}$	External force vector	N
h_{a}	Major axis dimension of rotational ellipsoid	m
h_{b}	Minor axis dimension of rotational ellipsoid	m
m	Exponent of Lame curve	–

n	Number of pores within a Sample	–
p	Pressure	$\frac{\mathrm{N}}{\mathrm{m}^2}$
r	Residuum	–
r_{int}	Concave pore radius	–
r_{A}	Experimental mean nearest neighbor distance of pores	µm
r_{E}	Analytical mean nearest neighbor distance of randomly distributed points	µm
$\mathbf{u}$	Displacement	m
v_{p}	Pore volume fraction	vol. %
$\mathbf{x}$	Position vector in deformed state	–
$\mathbf{x}_{\mathrm{hom}}$	Components of stiffness tensor	$\frac{\mathrm{N}}{\mathrm{mm}^2}$
A	Crossectional area	m^2
$\mathbf{A}$	Strain matrix	–
$\mathbf{A}_{\mathrm{ve}}$	Set of volume element base vectors	–
A_{R}	Aspect ratio	–
$\mathbf{B}$	Set of linear combination vectors	–
$\mathbf{C}$	Stiffness tensor	$\frac{\mathrm{N}}{\mathrm{mm}^2}$
$D_{\mathrm{x,y,z}}$	Dummy node	–
E	Young's modulus	$\frac{\mathrm{N}}{\mathrm{mm}^2}$
E_{p}	Photon energy	eV
$\mathbf{F}$	Deformation gradient tensor	–
G	Shear modulus	$\frac{\mathrm{N}}{\mathrm{mm}^2}$
I	Number of photons	$\frac{\mathrm{N}}{\mathrm{mm}^2}$
$\mathbf{I}$	Unity tensor	–
K	Bulk modulus	$\frac{\mathrm{N}}{\mathrm{mm}^2}$
L_{VE}	Edge length of volume element	m
$\mathbb{L}^3$	Spatial lattice	–
$\mathbf{N}$	Set of neighboring locations	–
$\mathbf{P}$	1^{st} Piola Kirchhoff stress tensor	$\frac{\mathrm{N}}{\mathrm{mm}^2}$
R	Degree of randomness	–
$\mathbb{R}^3$	Three dimensional space	m^3
$\mathbf{R}$	Rigid rotation tensor	–
$\mathbf{S}$	Compliance tensor	–
T	Temperature	K
$\mathbf{U}$	Pure homogeneous deformation	–
V	Volume	m^3

V_{BB}	Bounding box volume	m^3
V_{Pore}	Pore volume	m^2
W	Net work	J
$\mathbf{X}$	Position vector in reference state	–

List of Operators

Symbol	Description
$\langle\,\rangle$	Homogenized/effective quantity
∇	Nabla operator
$(\,)^{-1}$	Inverse
$(\,)^{T}$	Transpose
$\mathbf{a} \otimes \mathbf{b}$	Dyadic product
$\det(\,)$	Determinant
δ	Variation
Δ	Difference operator

Chapter 1

Introduction

1.1 Significance of Nickel-Base Superalloys

The progress in engineering is inevitably linked to the employed materials. An important group of multiphase materials are nickel-base cast superalloys which are extensively used for turbo machinery components. Modern turbine engines significantly contribute to the cost-effectiveness of aircrafts and help to keep environmental pollution to a minimum. Together with the air frame, the fuel-efficiency of jet engines is crucial for the market success of aircrafts. Figure 1.1 depicts an advanced turbofan engine which powers modern aircrafts having a per passenger fuel consumption of typically 3 liters per 100 kilometers. One of the main goals of civil jet engine development is to reduce the per passenger fuel

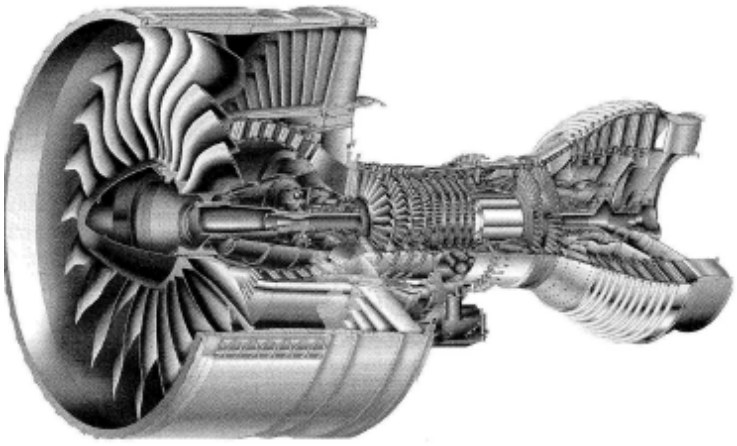

Figure 1.1: State of the art two shaft turbo machinery engine [1].

consumption even further by increasing the engines' efficiency. According to the laws of thermodynamics, this can be achieved by raising the turbine entry temperature (T_{TE}) of the gas streaming through the engine, which can be understood from Carnot's theo-

rem [4]. Using Carnot's theorem, the theoretical thermal efficiency η_{th} of heat engines can be calculated by

$$\eta_{\mathrm{th}} = 1 - \frac{T_0}{T_{\mathrm{TE}}} \tag{1.1}$$

where T_0 is the ambient gas temperature. Clearly raising the T_{TE} increases the turbine engines efficiency. However, the T_{TE} is limited by the capability of the turbo machinery components to withstand high temperatures [5]. In addition to increasing the T_{TE}, the efficiency of turbine engines can be increased by increasing the power to weight ratio. However, this implies increased stresses acting on the turbine components. High temperatures in combination with high mechanical loads clearly link the progress in modern jet engine design to advances in materials engineering. Materials engineering in turn necessitates a thorough understanding of the thermo-mechanical material properties which are determined by the materials microstructure [6]. Most industrial materials such as metal alloys exhibit a heterogeneous microstructure consisting of different phases and defects which can be distinguished at a sufficiently fine length scale [7] as shown in Figure 1.2. A phase is a region of the material wherein the physical material properties and chemical composition are only subject to slight fluctuations. Segregation and pores can be imagined as three dimensions defects within phases [8]. The physical phase properties and the morphology of the microstructural constituents of heterogeneous materials contribute to the overall (effective or homogenized) behavior of the material.[1]

As already mentioned nickel-base cast superalloys are used for turbo machinery components exposed to high thermal loads due to the alloys high temperature resistance and outstanding mechanical properties. A major problem casting these turbine parts is their complex geometry which gives rise to the formation of finely dispersed pores as shown in Figure 1.2 (c). The focus of this work is to determine the influence of porosity on the mechanical material properties of nickel-base cast superalloys. A thorough understanding of this influence is crucial to achieving a save component design while using the full mechanical potential of the material. An exclusively experimental investigation of the influence of pores on the mechanical materials behavior is neither practical nor feasible making the support of the experimental investigations by modeling strategies necessary. Modeling helps to investigate and understand the influence of porosity on the mechanical material properties. Furthermore, it provides the possibility to easily investigate parameter variations such as a different pore volume fraction.

[1] "Effective material properties" are deduced from the response of a statistically representative volume element of the heterogeneous material to loading, e.g. the effective Young's modulus, effective offset yield strength. "Homogenized material properties" are deduced from volume elements of the heterogeneous material which do not necessary have to be statistically representative.

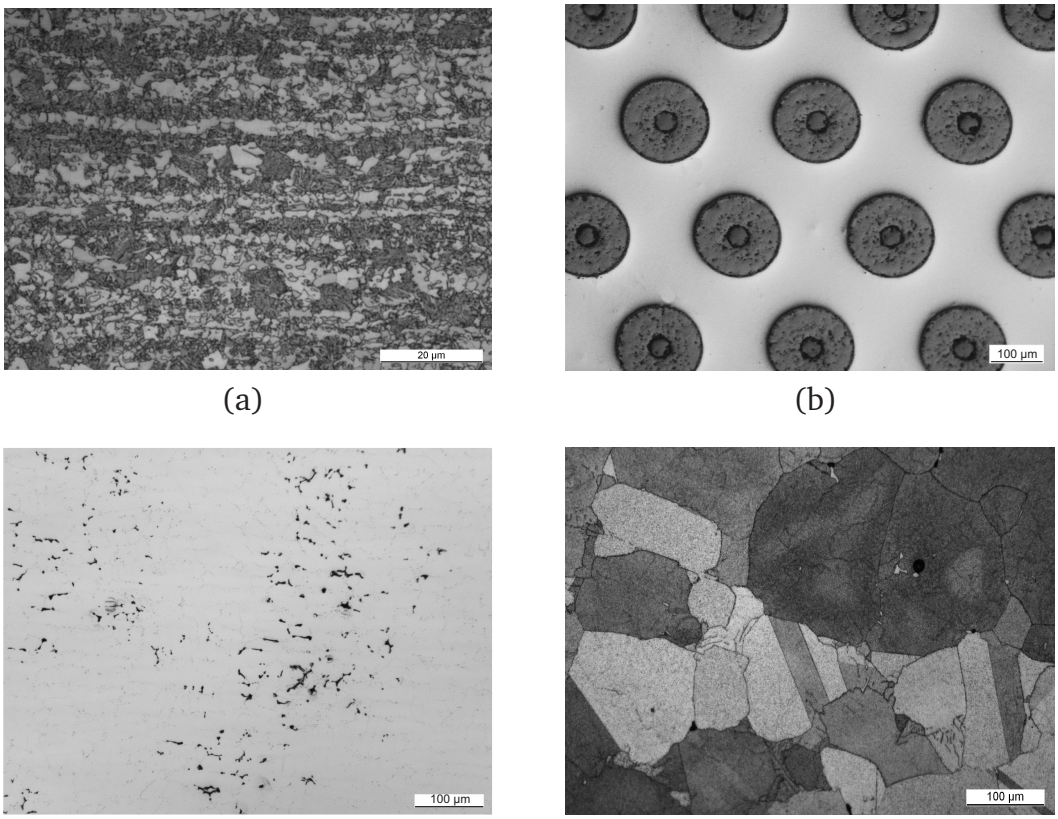

(a) (b)

(c) (d)

Figure 1.2: Various heterogeneous microstructures: (a) dual phase steel (DP 800) featuring ferrit (white), martensite (light grey) and bainite (grey); (b) Ti6Al4V matrix-coated fibre (MCF) composite [9]; (c) porous nickel-base cast alloy MAR-M247; (d) coarse grained IN-713 nickel-base alloy

1.2 Review of Modeling Strategies

Over the last century several approaches to capture the influence of a materials' microstructure on the effective material properties were developed. Voigt [10] and Reuss [11] were among the first to introduce analytical bounds estimating the elastic behavior of multiphase materials. They incorporated the phase volume fraction and phase specific properties into their calculations. Voigt introduced the linear rule of mixture [10] based on the assumption that the different phases are arranged parallel to the loading direction and are subjected to a uniform strain. He calculated the effective Young's modulus $\langle E \rangle$ as an average of the single phase moduli E_i weighted by their volume fraction v_i, which writes as

$$\langle E \rangle = E_1 v_1 + E_2 v_2 + \cdots + E_n v_n \,. \tag{1.2}$$

Voigt's assumption provides an upper bound for the elastic material properties. In contrast to Voigt, Reuss [11] derived a lower bound for the effective Young's modulus of

multiphase materials based on a uniform stress assumption for a serial arrangement of the phases, which is written as

$$\langle E \rangle = \frac{E_1 E_2 \cdots E_n}{E_1 v_1 + E_2 v_2 + \cdots + E_n v_n} \,. \tag{1.3}$$

Koutznetsova [7] pointed out that these approaches, strictly speaking, deny the influence of any morphological aspects apart from the phase volume fraction. Neither Voigt nor Reuss considered the case of a complex shape or a spatial arrangement of the phases.
Starting in the 1950s scientists have developed more sophisticated analytical methods to calculate the effective elastic materials properties of heterogeneous microstructures. Eshelby was the first to consider the effect of the shape of an inclusion on the stress and strain distribution. He derived the solution for the stress concentration caused by an ellipsoidal inclusion embedded in an infinite body [12]. Based on his contribution tighter analytical bounds as compared to Voigt and Reuss were proposed, which take the shape and spatial arrangement of phases into account. The Hashin-Shtrikman [13] bounds for example show especially accurate results for short fiber reinforced composite materials with a spatially random distribution of the fibers. The morphological assumptions considered by Hashin and Shtrikman closely match the real phase arrangement of short fiber reinforced materials as depicted in Figure 1.3. Hashin and Shtrikman derived

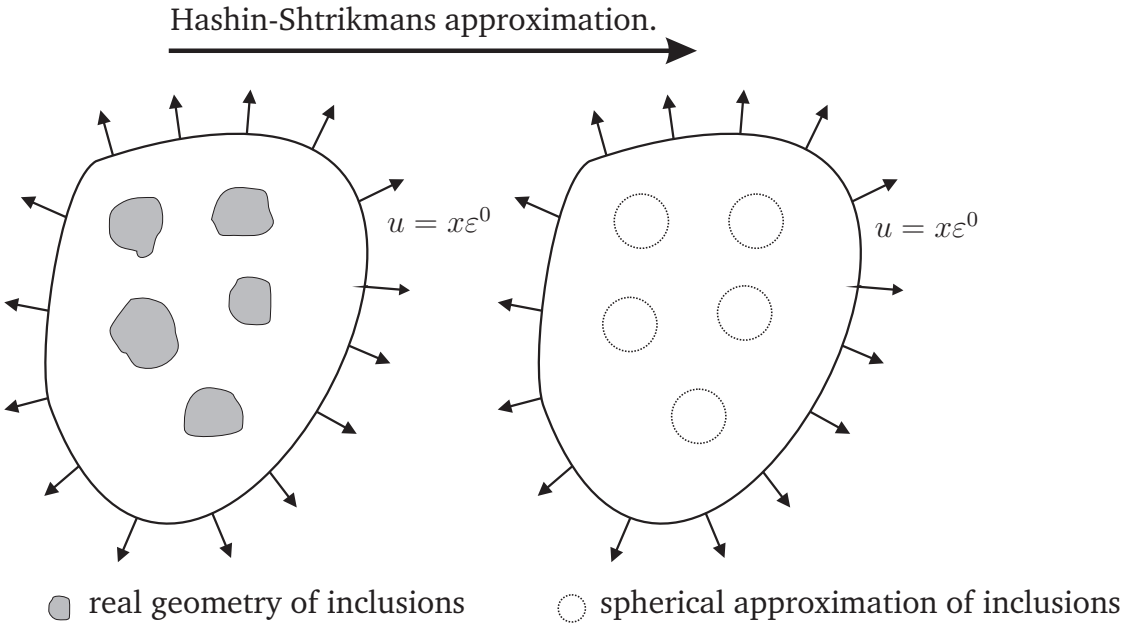

Figure 1.3: Schematic representation of the morphological approximation introduced by Hashin and Shtrikman. The inclusions are approximated by spatially randomly distributed spherical inclusions of constant eigenstrains (cf Patscheider [14]).

analytical expressions for the effective compression modulus as well as for the effective

shear modulus of multiphase materials. The effective Young's modulus can be derived using the effective compression modulus and the effective shear modulus as

$$\langle E \rangle = \frac{9\langle G \rangle \langle K \rangle}{3\langle K \rangle + \langle G \rangle}. \tag{1.4}$$

Further analytical bounds were proposed by a series of other scientists, among them Mori and Tanaka [15] and Hill [16]. Nemet-Nasser and Hori [17] provide a more complete overview of analytical homogenization methods. Although analytical bounds generally produce reliable results, there are some drawbacks to these methods. For example, the lower bounds degrade when there is a high contrast in the phase properties. This is especially unfavorable when investigating the influence of pores with an elastic modulus of $E_{\text{pore}} = 0$. In this case Reuss' assumption yields an effective elastic modulus of zero for any volume content of pores as can be seen by Equation (1.3). Apart from that the lower Hashin-Shtrikman bound is not defined for a porous material. Furthermore, analytical methods are limited in predicting the materials behavior in the plastic deformation regime and in analyzing the local stress and strain distribution within a specific phase.
Beginning in the late 1980s, the development of numerical methods and increasing availability of computational power offered a remedy for these problems. Many researchers used finite element methods to study effective materials properties as well as local phenomena. The finite element method (FEM) is a powerful tool to study and quantify local effects triggered by different phases. The potential to consider microstructural features such as the arrangement of the phases and their shape as well as to study complex loading paths is an advantage of FEM over analytical approaches. Furthermore, local stress and strain distributions can be investigated offering an additional benefit for fracture mechanical considerations.
Different volume element models which are used to investigate a variety of microstructural phenomena are known in literature. At the micro-scale level, there are two common types of geometry models: Real microstructure phase arrangements derived from 3D computed tomography (CT) and micrographs, and computer-generated geometries. An advantage of computer generated microstructure models as pursued in this work over geometries derived from the real microstructure is that the former enable parametric studies. The following review of some of these approaches is not exhaustive, but – as the objective of this work – points out relevant approaches for the investigation of porous materials.
In 1993 Nakamura and Suresh [18] studied the influence of residual stresses and fiber packing on the deformation behavior of metal matrix composites using volume element models. Later Sluis et al. [19] investigated the overall behavior of heterogeneous materials with microstructural finite element models. Werner et al. [20] studied the properties

of random polycrystalline two-phase materials focusing on the influence of contiguity and the cluster parameter using a finite element approach. Limitations of these early finite element approaches are that they are based on 2D models with simple phase geometries.

Böhm and Han [21] investigated the differences between two-dimensional and three-dimensional volume element models for particle reinforced metal matrix composites. They found that the phase averages of two-dimensional models differ noticeably from those of three-dimensional models. Two-dimensional models are generally too soft and underestimate the width of the distribution of microscale fields. Based on the work of Böhm and Han it is clear that reliable results can only be achieved using a 3D model. Three-dimensional volume element models are reported by e.g. Böhm [22], Ghosh [23], Shan [24] or Lee [25]. An overview of 3D volume element models is given e.g. by Suresh [26]. The purpose of finite element based volume element methods is twofold, namely to study local microstructural fields and to predict the effective stress-strain curves resulting from the micromechanical model using a phenomenological constitutive equation. These fitted constitutive models allow a more accurate macroscopic calculation of micro-heterogeneous materials.

However, such a straight forward approach to fit macroscopic constitutive laws to the results obtained from micromechanical models does not work for large deformations or complex loading paths of the macroscopic structure [7]. In this case so-called concurrent multiscale approaches are used, where the macroscopic constitutive law is updated at each increment and for each macroscopic integration point. Multiscale models provide the macroscopic constitutive material behavior based on the homogenization of a micromechanical model at a macroscopic point according to the local microstructure and loading path. Implementations of multiscale approaches have been reported by Temizer [27], Koutznetsova [7], Ghosh [28], Miehe [29, 30] and Ibrahimbegovich [31].

1.3 Scope of Work

The aim of this work is to implement a three dimensional micromechanical model predicting both the local microstructural fields as well as the effective material properties of porous nickel-base cast alloys. To use the results gained on the microscopic level for a finite element simulation of macroscopic structures a sequential multiscale model is introduced. Furthermore, for components undergoing large deformations and complex loading paths a basic framework of a concurrent multiscale approach is presented, which accounts for loading path dependencies.

Most multiscale implementations are based on non-commercial finite element codes abridging an industrial application. To address this shortcoming, within this work a multiscale approach, which couples three dimensional micro- and macro-structures is implemented in the commercial finite element code Abaqus.

1.4 Outline

In Chapter 2 the experimental methods are discussed. An overview on the development of nickel-base cast superalloys as well as a description of the MAR-M247 alloy is given. The industrial casting process used to produce turbine components is explained. A theoretical treatment of the formation of cast porosities is given. Furthermore, the methods of the microstructure characterization based on microscopy as well as on computed tomography are outlined.
In Chapter 3 the manufacturing of the samples is described. Furthermore, the experimental investigations are described. The samples are characterized in terms of pore volume fraction, pore volume distribution, pore shape and spatial pore distribution. These results provide the basis for the development of a three dimensional micromechanical volume element model capturing the characteristic features of porous cast alloys. Mechanical tests are performed in order to validate the mechanical modeling results.
Both the development of the micromechanical volume element model as well as the multiscale approach, which comprise the main focus of this work, are presented in Chapter 4. Based on the hypotheses outlined at the beginning of this chapter the implementation of the micromechanical model and the multiscale model is described.
In Chapter 5 the results gained from the experiments and from modeling are discussed.
Chapter 6 presents the conclusions drawn from this work. Furthermore, improvements of the micro- and multiscale models are proposed.

Chapter 2

Materials and Experimental Methods

2.1 Nickel-Base Superalloys

2.1.1 Fundamentals

Nickel-base superalloys are used for parts exposed to both high thermal and mechanical loads often in excess of 0.7 T_{M}[1] [32]. Furthermore, these alloys display excellent resistance to mechanical and chemical degradation. The suitability for high temperature applications of nickel-base superalloys can be explained by the properties of the materials' microstructure. The chemical composition of nickel-base superalloys promotes the formation of two predominant phases, namely the gamma (γ) and the gamma-prime (γ') phase. The γ phase is a solid solution with an fcc crystal lattice. Other than nickel it contains elements with similar atom radii, such as cobalt, chromium and molybdenum [5]. The atoms are randomly distributed on the lattice sites as depicted in Figure 2.2 (a). The γ phase forms a contiguous matrix embedding other phases [5] such as the γ' phase as shown in Figure 2.1. The γ' phase exhibits an fcc lattice with a strictly ordered arrangement of the atoms. As shown in Figure 2.2 (b) the nickel atoms are located at the face centers, whereas the larger Al respectively Ti atoms are located at the corners of the fcc lattice. Thus, the chemical formula of the γ' phase is Ni_3AL, Ni_3Ti or $Ni_3(Ti,Al)$. Even though the γ and γ' phases are coherent to each other, the γ' phase is largely responsible for the hight strength of the nickel-base superalloys. The ordered structure of the γ' phase aggravates the penetration of dislocations moving through the γ phase, since this would lead to an anti-phase boundary – the ordered crystal structure of the γ' phase would be disturbed. To avoid such anti-phase boundaries in the γ' phase, the passage of two dislocations from the γ phase is necessary. These dislocation pairs are called super

[1] T_{M} absolute melting temperature of the alloy.

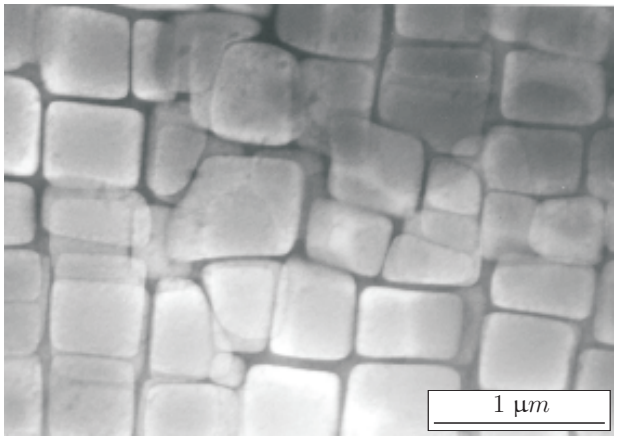

Figure 2.1: Transmission electron micrograph showing a large fraction of cubic γ' particles in a γ matrix [33].

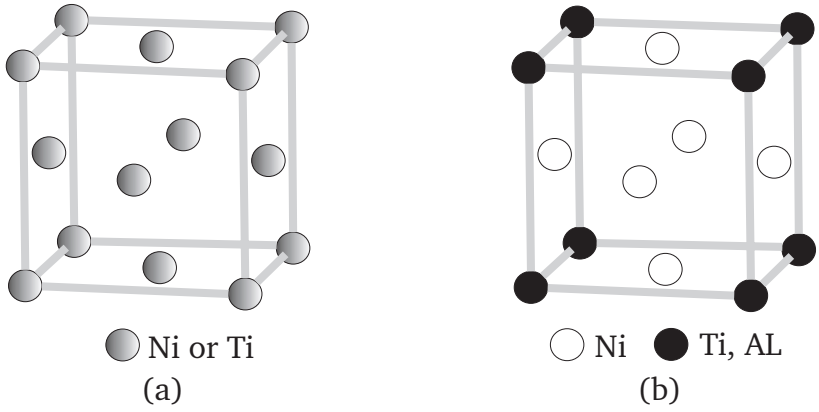

Figure 2.2: Crystal structure: (a) gamma (γ) phase with a random distribution of atoms in an fcc lattice; (b) gamma prime (γ') phase with an ordered arrangement of the atoms in the fcc latice – the Ni atoms are located at the face centers, whereas the Ti or Al atoms are located at the vertexes of the lattice (cf. [32]).

dislocations. The requirement for dislocations to pair up makes it more difficult for them to penetrate the γ' phase [32].

As mentioned in Chapter 1 the efficiency of gas turbine engines is closely linked to raising the T_{TE}. Thus, the alloy design of nickel-base superalloys is geared towards improving the creep life and yield stress of the alloys at elevated temperatures. A historical review of the nickel-base superalloy development regarding the temperature for 1000 hour creep life at 137 $\frac{\mathrm{N}}{\mathrm{mm}^2}$ is given in Figure 2.3. As can be seen, early nickel-base superalloys were used in wrought form only. The development of vacuum induction casting technologies in the 1950s drastically improved the materials' performance since it significantly enhanced the quality and cleanliness of the alloys [5]. Furthermore, new alloying concepts were developed.

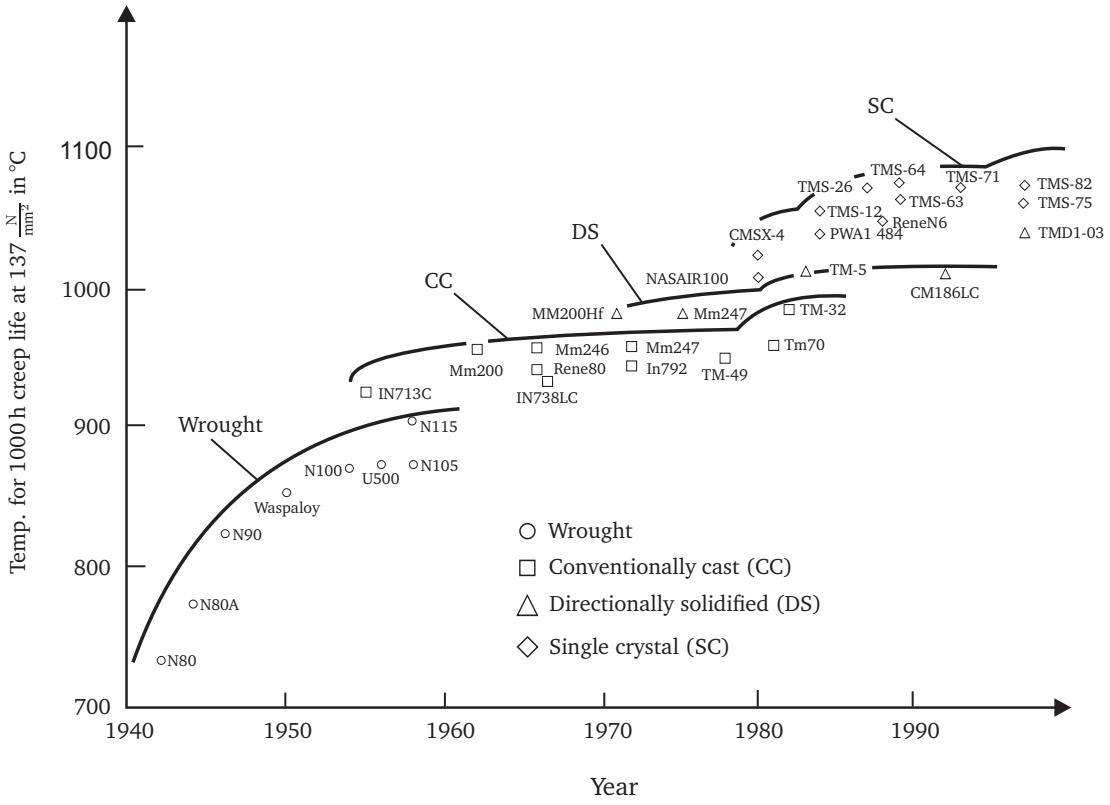

Figure 2.3: Improvement in temperature for 1000 h creep life at 137 $\frac{\mathrm{N}}{\mathrm{mm}^2}$ of Ni-base superalloys over a 60 year period (cf. [34]).

One widespread nickel-base superalloy focused on within this work is MAR-M247. The alloy was developed in the 1970s and is used for structural cast components in turbine engines.

2.1.2 The Nickel-Base alloy MAR-M247

The nickel base alloy MAR-M247 was developed aiming at optimized castability and high temperature resistance. The chemical composition of MAR-M247 according to the material data sheet [35] is given in Table 2.1, which also lists the effects of the individual alloying elements. Furthermore, the chemical composition of the sample material used within this work is presented. This is measured using energy-dispersive X-ray spectroscopy (EDX). As can be seen the measured alloy composition of the sample material closely matches the specification. According to the material data sheet [35] MAR-M247 contains a phase volume fraction of 60 % γ' particles embedded in the γ matrix (see Figure 2.1). Both phases are stable at high temperatures. In addition to the γ and the γ' phases, elemental segregation during solidification causes the formation of small amounts of an eutectic γ/γ' phase [35], which can be mitigated by an adequate heat treatment.

Table 2.1: Chemical composition of the MAR-M247 cast alloy as well as the effect of the alloying elements.

Alloying elements	Weight fraction (wt %) according to [35]	EDX measurement Sample material (wt %)	Effect
Ni	59	60.55 ±0.39	–
Co	10	10.37 ±0.2	corrosion resistance
W	10	10.05 ±0.31	solid solution hardening
Cr	8.25	8.65 ±0.14	enhanced corrosion resistance
Al	5.5	5.65 ±0.13	γ' former
Ta	3	2.34 ±0.35	solid solution hardening
Hf	1.5	–	enhanced hot cracking resistance
Ti	1	1.13 ±0.08	γ' former
Mo	0.7	–	solid solution hardening
C	0.15	–	carbide former
Zr	0.05	–	grain boundary hardening
B	0.015	–	grain boundary hardening

Next to these microstructural constituents, carbides are found mostly in inter-dendritic regions and at grain boundaries [5]. Several carbide morphologies, such as globular, blocky or script have been reported by Haruna [36] and Huangh and Koo [37]. Carbides are particularly beneficial for the high-temperature grain boundary creep properties. Furthermore, they have a positive influence on the rupture strength [5].

The manufacturing process has a significant effect on the phases and phase fractions present within an alloy. The phases in turn determine the mechanical material behavior. To gain an understanding of the production process of MAR-M247 components, the casting process is discussed in more detail in the following section.

2.1.3 Casting Process

Casting is one of the oldest forming processes and can be tracked back to 5000 BC [38] when it was used to form simple tools. Also today casting is still one of the most important forming processes and is widespread in industry. Also nickel-base superalloy components are commonly manufactured by casting, more precisely by vacuum induction melting (VIM) and subsequent vacuum investment casting. The vacuum prevents the formation of gas pores [39]. Furthermore the vacuum retains oxidation reactions of the melt with the atmosphere [40].

Investment casting, also known as *lost wax* process, involves several steps. First a model of the casting is produced by injecting wax into a metallic master mold [5]. This wax replica of the cast part including runners and feeders is surrounded - *invested* - with ceramic slurry to form a mold [41]. The slurry consists of binding agents and mixtures

of zirconium silicate $ZrSiO_4$, aluminum oxide Al_2O_3 and silicon dioxide SiO_2. After the wax model is covered with slurry it is baked in a multi step process. The wax within the mold is melted at moderate temperatures. Subsequently the mold is fired to increase its stability. The finished mold is preheated before the metal melt is poured into the cavity to prevent temperature induced cracking. The cast temperature of a nickel-base melt is approximately 1550 °C. After the casting is cooled down, the mold is removed from the cast part. A basic diagram of an investment casting process is provided in Figure 2.4. The

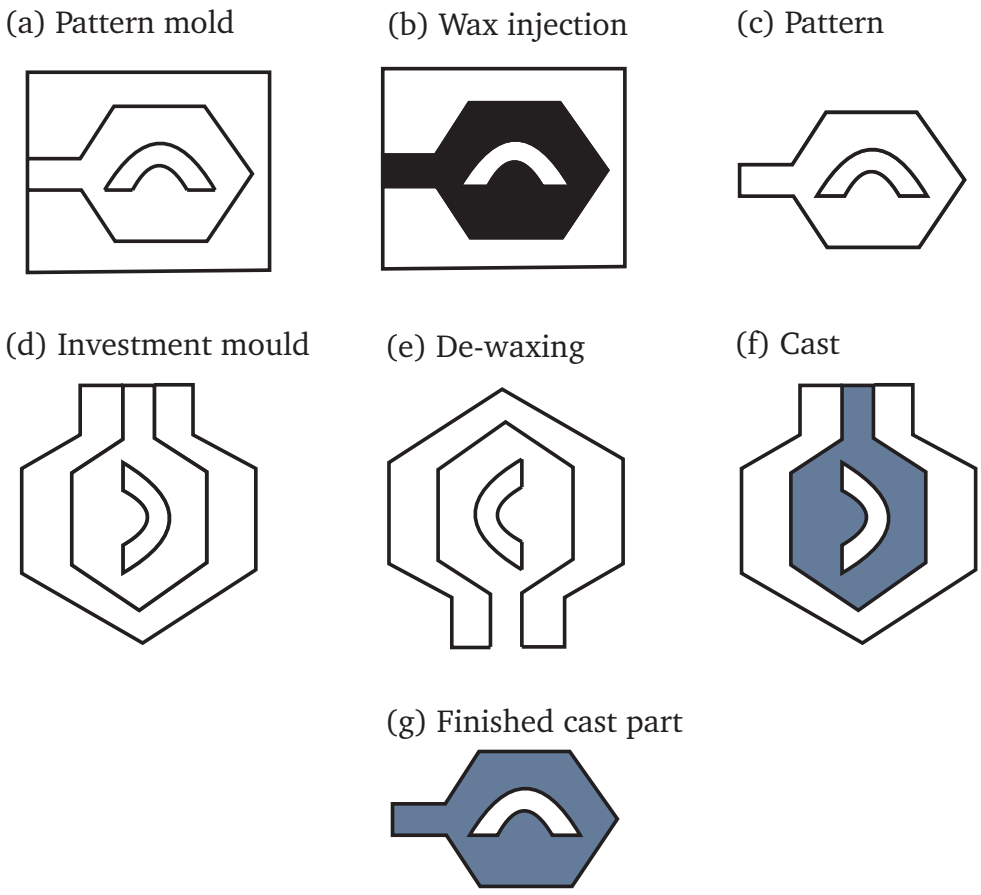

Figure 2.4: Basic principles of the investment casting process [2]. The pattern mold (a) is used to produce a wax replica of the casting (b & c). This wax replica is subsequently surrounded (invested) with a ceramic slurry (d). To obtain the final cast mold (e) the wax is melted at moderate temperatures and the mold is fired to increase its stability. The melt is then casted into the mold (f). Once the casting is solidified, the mold is removed.

quality of the casting is defined by a variety of parameters: Next to the temperature of the melt, the temperature of the mold and the cooling rate, the arrangement of runners and feeders is of high importance for the quality of the casting. Feeding is the process, which compensates the volume contraction during solidification. A feeder is a separate reservoir of melt attached to the casting that balances the volume contraction of the melt during solidification [3]. The contraction of the liquid upon solidification is due

to a rearrangement of the atoms from a near field arrangement in the liquid state to a regular crystalline array exhibiting a significantly denser packing in the solid state. Especially for the nickel base alloys exhibiting an fcc lattice feeding is of high importance since the rearrangement of the atoms during the face transformation from liquid to solid state causes a large volume contraction. As a consequence of the solidification process, different feeding mechanisms can be identified. A schematic representation of the main feeding mechanisms is given in Figure 2.5. The most common feeding mechanism is

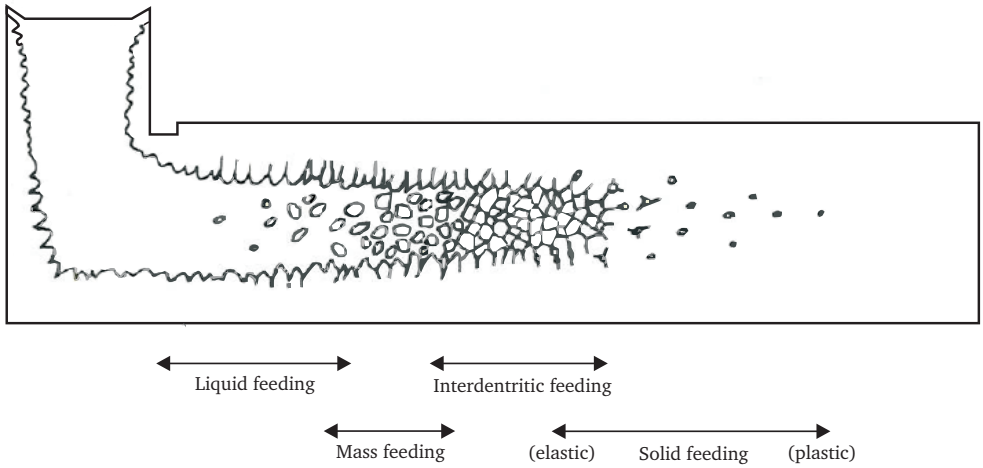

Figure 2.5: Schematic representation of the feeding mechanisms in a solidifying casting [3]. The more material is solidified, the harder becomes the feeding of liquid material to balance the volume contraction (liquid, mas and interdentritic feeding). If a liquid region is completely surrounded by solidified material, the only option of feeding is elastic or plastic deformation of the surrounding area. This causes the build up of hydrostatic tension. If the tension exceeds a critical limit shrinkage pores evolve (cf. Section 2.1.4).

liquid feeding. It occurs in regions where the casting has a fully liquid core. In regions, where up to 50 percent of the melt is already solidified, mass feeding is observed. Mass feeding denotes the movement of a slurry of solidified metal and residual liquid [3]. Once the solidified dendrite structure is not surrounded by liquid material the volume contraction can be balanced by inter dendrite feeding. Inter dendrite feeding describes the capillary flow of the melt between the dendrite arms. In case a liquid region is confined by solidified material the volume shrinkage can be balanced by elastic and plastic deformation of the casting. This occurs at a late stage in freezing, when sections of the casting can become isolated from liquid feeding. Solid feeding is accompanied by the buildup of hydrostatic tension within the material and a deformation of the casting. Pores are caused by both lack of the aforementioned mechanisms and the hydrostatic tension exceeding a critical limit. This will be investigated in more detail in the following section.

2.1.4 Formation of Cast Porosity

Campbell [3] states that in the absence of gas and with adequate feeding of the cast part no porosity should be found in the casting. However, castings for aerospace applications often exhibit complex shapes so that one or more regions of the part cannot be optimally fed until the whole part is solidified. This gives rise to the formation of shrinkage porosity. These pores can be exposed by light optical microscopy (LOM) inspections of structural cast parts as shown in Figure 2.6. The driving force for the initiation of

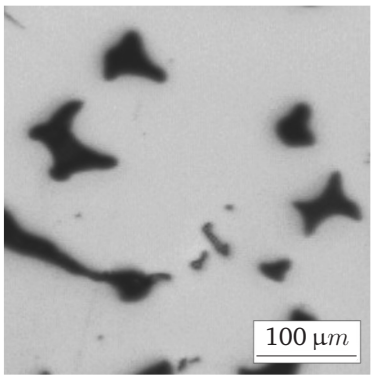

Figure 2.6: Cross sectional micrograph of a sample containing 4.9 vol. % of pores (black).The pores vary in size and shape and have concave as well as convex radii.

shrinkage porosity is the hydrostatic tension building up in regions where the feeding of metal during solidification is not ensured. If this hydrostatic tension reaches a critical limit pores may form in a number of ways. Shrinkage porosity is closely linked to the thickness of the section which is not well fed. Thin sections mainly exhibit a surface deformation called external porosity. When the internal shrinkage is not balanced by liquid feeding the lowering of the internal pressure causes an inward movement of the external surface of the casting. This inward movement constitutes a solid feeding with the effect that *sinks* or *draws* are found at the surface of the casting [3].

Thicker sections of a casting which are not well fed show internal porosity. At the early stages of solidification these sections form a sound, solid skin. Meanwhile liquid feeding is still assured in the center of the casting. By a further freezing of this region the internal pressure decreases. During the cooling of a liquid region embedded in an already solidified section of the casting, the liquid will be stretched while the surrounding solid will be drawn inwards first elastically, then plastically. Once the stress in the liquid phase reaches the critical limit of the fracture pressure p_{f} a pore will form and thereby release the stress in the surrounding liquid metal. A theoretical value for the fracture pressure needed for the initiation of internal shrinkage porosity is derived in the work

of Fisher [42]. He stated that the work required for the formation of a cavity within a liquid can be calculated by

$$W \;=\; \gamma\, A + p\, V - p_{\mathrm{r}}\, V \;=\; 4\pi r^2\gamma + \frac{4}{3}\pi r^3(p - p_{\mathrm{r}}) \tag{2.1}$$

where W is the net work associated with the formation of a spherical bubble of radius r, γ is the inter-facial energy per unit area needed to create the phase boundary between bubble and liquid p is the pressure of the liquid and p_{r} is the pressure in the bubble. In the case of shrinkage porosity the internal pressure is zero and Equation (2.1) simplifies to

$$W \;=\; 4\pi r^2\gamma + \frac{4}{3}\pi r^3 p. \tag{2.2}$$

In Figure 2.7 the net work W is plotted as a function of the pore radius. It can be seen

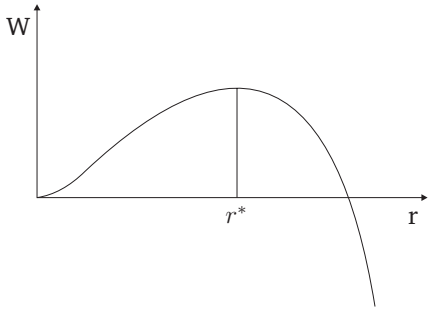

Figure 2.7: Required work for reversible formation of a bubble of radius r in a liquid under negative pressure.

that pores with a radius smaller that the critical radius r^* require free energy for further growth, whereas pores with $r > r^*$ grow with a decrease of free energy. According to [42] the curve has a maximum of $W_{\max} = 16\pi\gamma^3/3p^2$ at a critical radius of

$$r^* = -\frac{2\gamma}{p}\,. \tag{2.3}$$

According to Campbell [3] one atomic diameter is a reasonable assumption for the critical pore radius. Using Equation (2.3) and the experimentally determined surface energy γ for liquid metals, the theoretical value of the critical pressure p_c at which shrinkage porosity will nucleate can be calculated. The results of this theoretical critical pressure for various liquids are given in Table 2.2. According to the values given in Table 2.2 an extremely high hydrostatic tension is necessary to trigger the formation of pores. However, these are theoretical values for the formation of pores within pure liquids, whereas in reality, seeds for the formation of pores such as solidified dendrites, carbides or other solid particles, which are dispersed within the melt can be found. These seeds lower the required hydrostatic tension for the formation of pores [3].

Table 2.2: Fracture pressures of liquids. Surface tension and Atomic diameter except for nickel taken from [3].

Liquid	Surface tension $\left(\frac{\mathrm{N}}{\mathrm{m}}\right)$	Atomic diameter (nm)	p_c from Equation(2.3) $(\mathrm{atm/MPa})$	p_c from [42] $(\mathrm{atm/MPa})$
Water	0.072	–	–	1320 / 134
Mercury	0.5	0.30	16700 / 1692	22300 / 2259
Aluminum	0.9	0.29	31000 / 3141	30000 / 3039
Copper	1.3	0.26	50000 / 5066	50000 / 5066
Iron	1.9	0.25	76000 / 7700	70000 / 7092
Nickel	1.77 *)	0.25	70000 / 7080	–

*) from [43]

2.1.5 Effects of Porosity

Concerning effective mechanical material properties, the ductility and the fracture stress are strongly influenced by the volume fraction of pores. This has been investigated by Baldwin and Edelson [44]. Their results on the influence of pores on ductility and fracture of a copper alloy are presented in Figure 2.8. It shows that already low pore

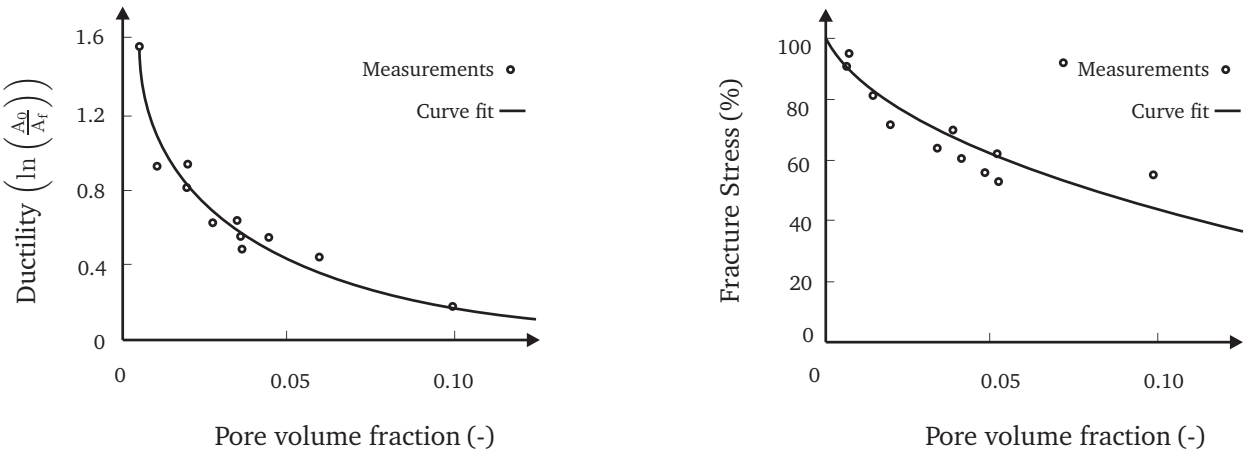

Figure 2.8: Effect of pores on ductility and fracture stress of copper. In the ductility measure A_0 is the original crossectional area of the specimen and A_f is the cross sectional are of the specimen after fracture. Data from Edelson and Baldwin [44].

volume fractions have a strong impact on fracture stress and ductility. This is because fracture is closely linked to stress concentrations. Such stress concentrations are caused by pores, where the shape of the pore governs the severity of the stress concentration. Therefore even small pore volume fractions are critical for the fracture toughness and ductility of a material.

Even though pores influence the material properties, the influence of pores on the functionality of castings has to be discussed individually depending on the location of the pores and the loads acting on that particular location. For example, a large pore located in a low stressed region of a casting will most likely have negligible effects on the properties of the casting, while a smaller pore located in a region subjected to high stresses may disqualify the casting as a structural component [3]. The discussion if a porous region within a casting is critical for the load bearing function of the part is crucial for the design and quality inspections and will be tackled in Chapter 4.3.

2.2 Destructive and Nondestructive Materials Testing

To characterize the morphology of pores in the cast MAR-M247 samples metallography and computed tomography is used. The goal is to derive a simplified parameterizable pore model based on primitive geometries offering the potential to perform parametric studies e.g. investigating the influence of a varying pore volume fraction on the mechanical behavior of the material.
Vice versa, the results gained by such a parametric study have to be experimentally validated. Therefore the influence of pores on the mechanical materials' behavior is studied using compression tests.

2.2.1 Metallography

The main goal of metallography is the qualitative and quantitative description of the microstructural constituents present in metallic materials. This includes the identification and determination of the

- amount
- size
- shape
- spatial distribution and
- texture

of the constituents by applying direct imaging techniques [45]. Through an accurate description of the microstructural constituents their influence on the physical material properties can be assessed. A main instrument of metallography is the light optical microscope (LOM). The preparation of samples for LOM analysis is important, since the true microstructure may be partially or fully obscured by a poor sample preparation [46]. A detailed description of the sample preparation can be found in [46, 45]. Certain fea-

tures of the microstructure such as pores can be observed in the as-polished condition if the constituents exhibit a sufficient difference in light reflectivity after polishing [46]. The analysis of crossectional planes (2D) is the most common approach to study the morphology, size and distribution of pores within cast metals [47].

2.2.2 Computed Tomography

Theoretical background

The basis for computed tomography is X-ray radiography where an X-ray beam is sent trough an object and the attenuation of the beam is recorded [48]. A schematic representation of an X-ray projection is shown in Figure 2.9. The attenuation of the X-ray beam

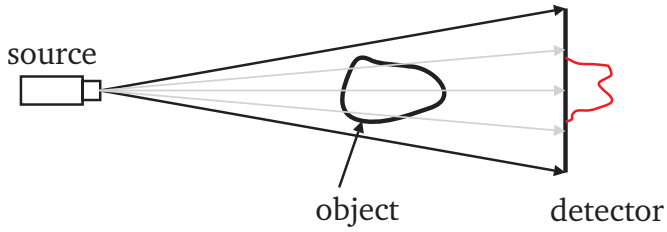

Figure 2.9: Schematic two dimensional representation of X-ray radiography with a conical beam (cf. Figure 2.11 (b)).

depends upon the interaction of the photons with the material by one of the following mechanisms:

- The photoelectric effect causes an absorption of a photon by an atom. The whole energy of the photon is transmitted to an electron of the atom it interacts with. As a consequence the electron is emitted from its shell [49]. The vacant electron spot is filled by either an electron from a higher shell or by a free electron.
- Compton scattering is similar to the photoelectric effect. As in the photoelectric effect the photon interacts with an electron in the absorbing material. However, the Compton effect describes an interaction of the photon with a free electron where the photon transmits part of its energy to the free electron [49] and the photon is deflected between 0 and 180° with respect to its original direction.
- Pair production can occur for photons with an energy exceeding 1.02 MeV. By pair production the energy of the photon is directly converted into matter which usually occurs in the vicinity of the atom nucleus. The photon is transformed into an electron and a positron. The photon energy in excess of the amount needed for the conversion into matter is converted into motion of the positron electron pair [50].

The ratio of the emitted (I_o) to incident (I) photons for X-ray radiography is described by the Beer-Lambert law for monochromatic X-ray beams as

$$I \;=\; I_o \, e^{\left(-\int_{\mathrm{path}} \mu(\mathbf{x},E_\mathrm{p})\,\mathrm{d}s\right)}\,, \tag{2.4}$$

where $\mathrm{d}s$ is the differential path length of the photons' trajectory and $\mu(\mathbf{x})$ is the attenuation coefficient of the point $p(\mathbf{x},\mathbf{y},\mathbf{z})$ and the photon energy E_p. In case of polychromatic X-rays with a broad energy spectrum Equation (2.4) can be generalized by integration over all energies. This is written as

$$I = \int_0^\infty I_\mathrm{o}(E_\mathrm{p})\; e^{\left(-\int_{\mathrm{path}}\mu(\mathbf{x},E_\mathrm{p})\mathrm{d}s\right)}\,\mathrm{d}E_\mathrm{p}\,. \tag{2.5}$$

However, the photon energy spectrum of polychromatic sources can be averaged and Equation (2.4) can be used yielding a good approximation [47]. As can be seen in Equations (2.4) and (2.5) the ratio of emitted to incident photons depends on the integrated attenuation coefficient and the photon energy. The attenuation coefficient describes to which extent the energy of a beam passing through an object is absorbed. The attenuation coefficient depends on the atomic number of the elements and the photon energy.
In contrast to X-ray radiography computed tomography (CT) enables a three dimensional representation of the attenuation coefficient [47]. For this purpose multiple radiographic projections of an object are taken at different angles as shown in Figure 2.10. The sample volume to be reconstructed is numerically divided into so-called voxels which is a coinage meaning volumetric pixels. Utilizing mathematical image reconstruction algorithms a specific attenuation coefficient is assigned to each of these voxels based on the radiographic projections (cf. [51]) which is then transformed into a grayscale value. To visualize pores a threshold for the greyscale value is defined deciding if a voxel is interpreted as material or as a pore.

Setup of CT Systems

X-ray CT systems consist of an X-ray source, an X-ray detector and a stage for the mechanical manipulation of either the object or the source and the detector. The stage allows the relative positioning of the sample with respect to the X-ray source and the detector. The sample is usually positioned in a way that the path length of the beam through the material is minimized. While all CT systems consist of the same components, there are different configurations for acquiring the CT data [47]. A brief description of the most common setups, which are depicted in Figure 2.11 is presented below. As can be seen in Figure 2.11, different beam geometries are used for CT scans. Either a conical beam

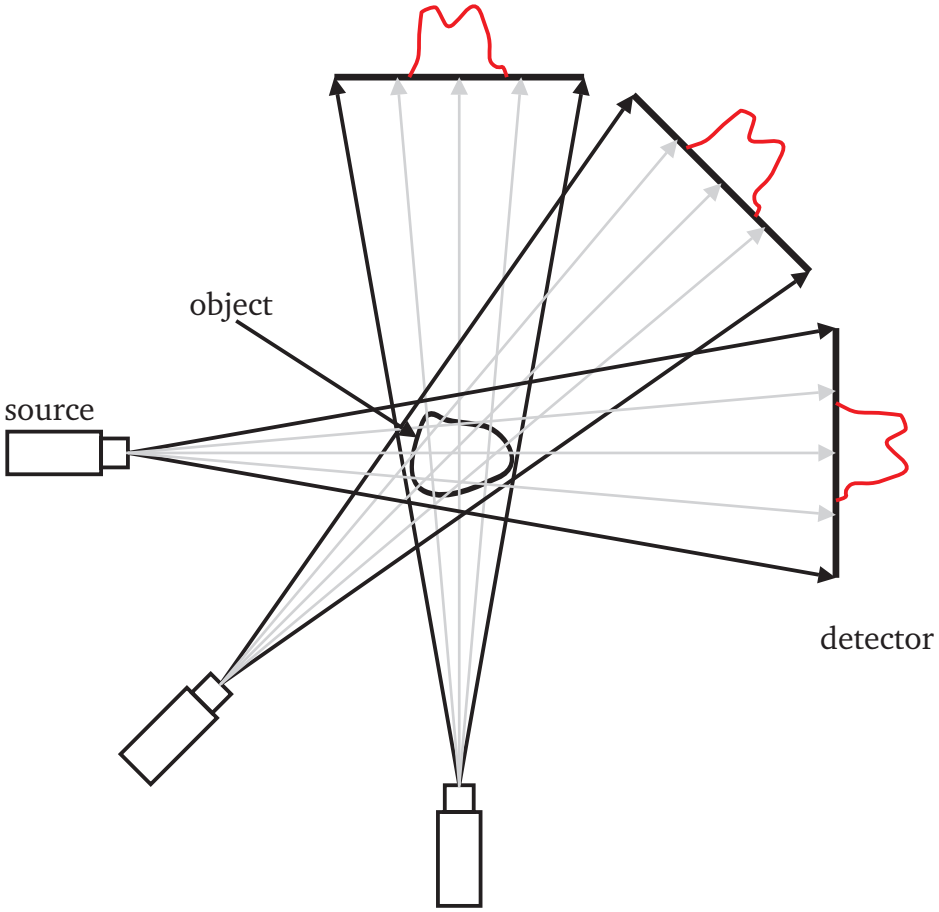

Figure 2.10: Schematic representation of multiple X-ray radiographic scans. The source and detector are mounted on a common stage. Either the stage holding the X-ray source and the detector, or the object is rotated incrementally. Based on multiple X-ray projections the three dimensional CT image can be reconstructed.

emitted by an X-ray tube or parallel beams as obtained by synchrotron sources is used. Since all CT scans in this work are acquired using conical beam sources, this setup is discussed in more detail. For a comprehensive treatment of synchrotron sources the reader is referred to [52]. X-ray tubes are the most common source to produce polychromatic X-rays [47]. The X-rays are emitted from a metallic target generating a polychromatic conical beam [48]. The sample is placed in between the X-ray source and the detector. When using a conical beam, the sample position relative to the X-ray source and the detector determines the magnification of the sample as can be seen in Figure 2.11 (a) and 2.11 (b). The closer the sample is positioned to the X-ray source, the higher is the resulting magnification on the detector. A detailed description of the different radiation detection technologies can be found in [53]. The most common detection technologies consist of a scintillator in combination with a charged coupled device (CCD) camera or with photodiodes. The scintillator converts the X-ray beam into visible light. The inten-

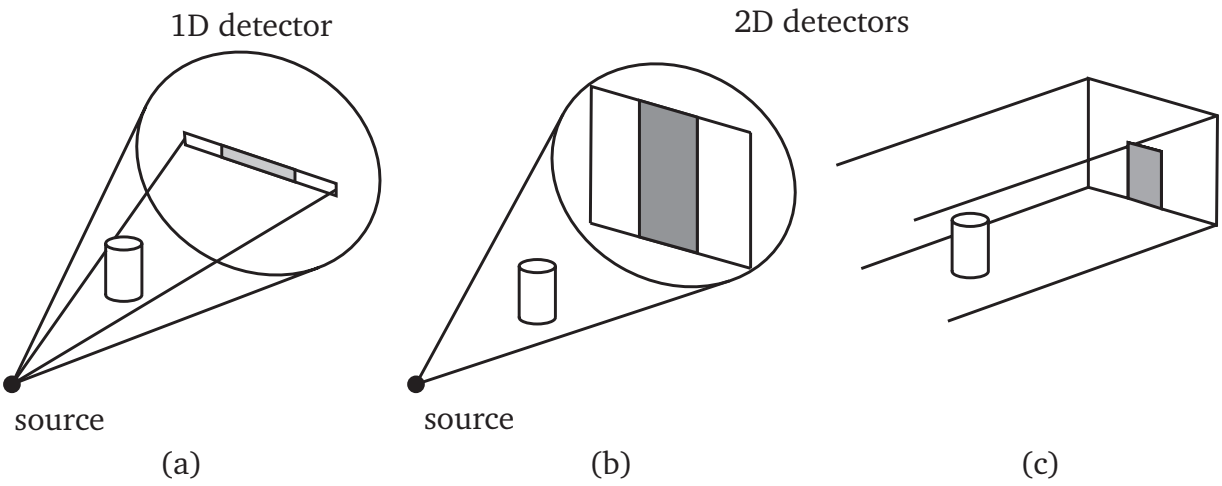

Figure 2.11: Main components of CT scanners: (a) conical beam X-ray source with 1D detector. (b) conical beam X-ray source with a 2D detector. (c) parallel beam X-ray source (e.g. synchrotron) with a 2D detector [48].

sity of the light is then measured by a CCD or photodiode detector. Based on the acquired data a three dimensional representation of the scanned volume is generated by means of image reconstruction.

According to Smith [54] there are four main approaches to reconstruct the slice image of a sample from the recorded data given a sufficient set of scans from different angles. The straight forward method is to solve a system of linear equations where the number of equations scales linearly with the number of voxel. More sophisticated reconstruction methods are the iterative technique, filtered back-projection or the Fourier reconstruction. A detailed theoretical treatment of the reconstruction techniques can be found in e.g. [55, 56]. Whichever technique is used, one has to beware of artifacts due to noise in the CT data, which can obscure the resulting image. An overview of the most commonly observed artifacts is given in the following.

- Ring artifacts are concentric rings to the axis of rotation of the sample. They originate from local sensitivity fluctuations of the detector or scintillator [52].
- Edge artifacts are due to a sharp density transition, e.g. at outer or inner surfaces of the material. Especially when evaluating pores within a material this artifact can be troublesome since pores represent inner surfaces of the material. The effect can be minimized by reducing the distance between sample and detector.
- Image noise results from energy spikes or from an unfavorable conversion rate of X-ray photons to visible light [52]. This can be reduced by employing median filters. This type of filter changes the greyscale value of a voxel to the median of the surrounding voxels greyscale value (cf. [57]) thus diminishing the noise in the measuring results.

- Positioning errors these errors might occur due to imprecise positioning of the sample on the stage. For example if the sample is moved during the data acquisition of one tomography view. These errors can be corrected by an adequate post-processing of the CT raw data.

2.2.3 Compression Test

The compression test is used to determine the offset yield stress of the sample material under uniaxial compressive loading. The test is standardized in the DIN 50 106 [58]. According to DIN 50 106 a specimen is loaded by an uniaxial compressive force with a loading rate below 30 $\frac{\mathrm{N}}{\mathrm{mm^2 s}}$. The load is increased until the yield stress of the material is exceeded. Next, an unloading – loading hysteresis is performed. The slope of the elastic regime is determined by the slope of a linear fit of the hysteresis loop as schematically shown in Figure 2.12. This line is then shifted parallel, to intersect the strain axis at 0.2 %. The offset yield stress $\mathrm{R_{p0.2}}$ is evaluated by determining the intersection of the shifted elastic line and the recorded load-displacement curve which is converted into a stress-strain curve taking the sample dimensions into account.

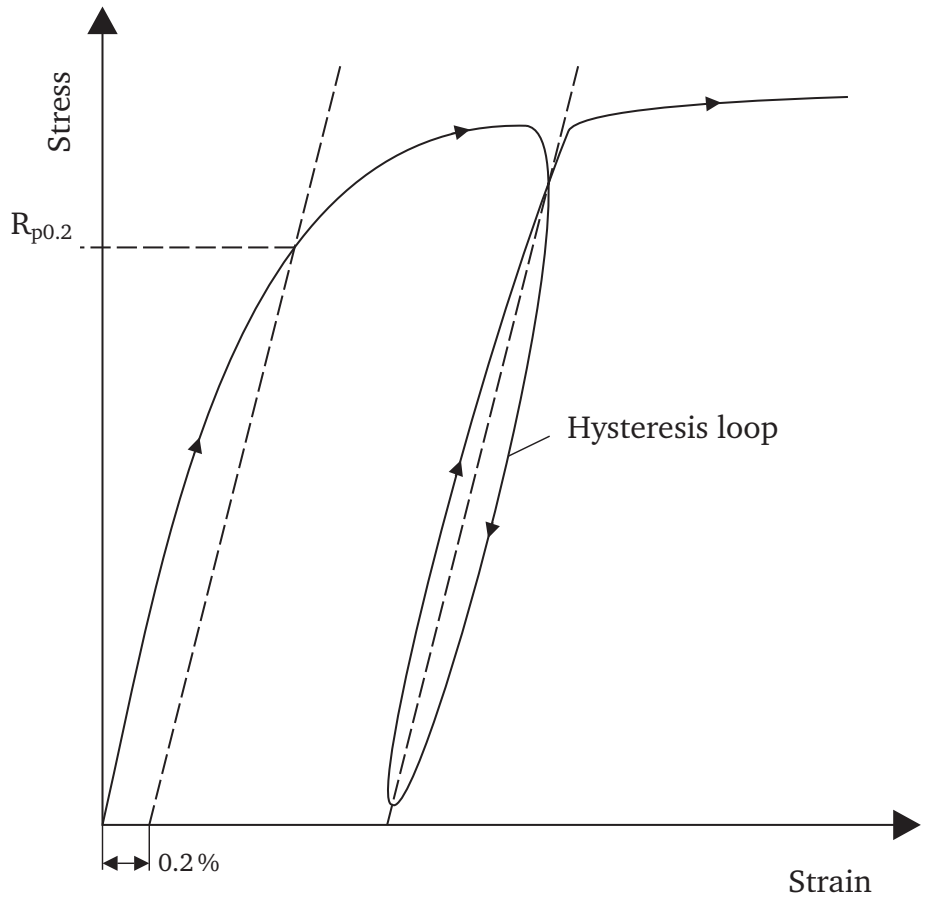

Figure 2.12: Schematic representation of the evaluation of the offset yield strength. Assuming isotropy the offset yield strength in compression and tension are equal. However, the evaluation of the offset yield stress within this work is based on compression tests. For this purpose the sample is loaded until the offset yield stress is exceeded. Then an unloading–loading hysteresis is performed, where the mean slope is evaluated and used to obtain the offset yield stress (cf. [58]).

Chapter 3

Experimental Procedure and Evaluation

> "In the matter of physics, the first lessons should contain nothing but what is experimental and interesting to see."
> *From "Einstein on Education", Nation and Anthenaeum, December, 3rd, 1921*

3.1 Production of Porous Samples

The castings to extract the samples are produced by VIM and subsequent investment casting under vacuum. The ingot material provided by a certified supplier was cast into rods with a length of 100 mm and a diameter of 30 mm by MaTeck[1] as shown in Figure 3.1 (a). The cooling of the melt triggers the formation of a large shrinkage cavity with an adjacent porous region which is depicted in Figure 3.1 (b). The samples are extracted from this porous region.
Next to the casting parameters the sample material has to match the material specification to gain relevant results for turbine cast parts. A comparison of the sample material

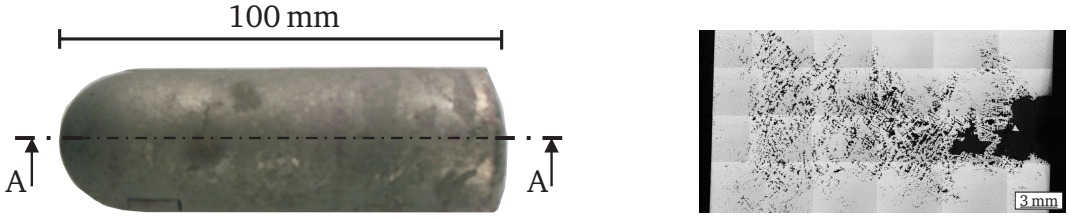

(a) (b)

Figure 3.1: Sample material: (a) Cast rod; (b) Cross sectional micrograph of the cast rod (A-A). Note the macroscopic cavity and the adjacent porous region.

to the material specification is presented in Table 3.1. The specification is in good agree-

[1] Experimental foundry located in Jülich, Germany

ment with the alloy contents measured within the sample material. The contents of C, Zr and B could not be verified due to their low mass content.

Table 3.1: Chemical composition of MAR-M247 as defined in the material specifications and as found in the sample material in wt %.

Phase	Ni	Co	W	Cr	Al	Ta	Hf	Ti	Mo	C	Zr	B
Specification	balance	10.0	10.0	8.25	5.5	3.0	1.5	1.0	0.7	0.15	0.05	0.015
Samples	60.24	10.35	10.26	9.06	5.68	1.63	0.95	0.96	0.86	–	–	–

3.2 Sample Preparation

The samples are extracted from the cast rods using electric discharge machining (EDM). The rods are cut into slices perpendicular to their longitudinal axis with a slice thickness of 6 mm as depicted in Figure 3.2 (a). These slices are subsequently milled to ensure parallel faces. The final slice thickness is 5 mm. From these slices, rectangular samples are cut by electric discharge machining as presented in Figure 3.2 (b). The pore volume

(a) (b)

Figure 3.2: (a) Slice from the cast rod. The samples extracted from the rod can be seen. They are labeled 01-12 starting at the top left sample. (b) Three dimensional representation of a porous prismatic sample. The sample was reconstructed from CT data.

fraction of a sample depends on the location of extraction. Samples from slices closer to the shrinkage cavity (cf. Figure 3.1 (b)) tend to exhibit higher pore volume fractions.
After the samples are extracted, they are labeled according to their location of extraction. The first number in the label indicates the slice, where the sample is extracted from. The higher the slice number, the closer it is located to the shrinkage cavity. The slice numbers range from 1 to 5. The second two numbers count the samples extracted from a particular slice as depicted in Figure 3.2 (a). So the sample labeled 1-02 originates from

the slice furthest from the shrinkage cavity, and is the second sample extracted from this slice.
The porous samples are investigated using metallography and computed tomography, which will be discussed in the following.

3.3 Metallographical Investigation

Metallography is used in a twofold way. Firstly, cross sectional micrographs of the cast rods are taken providing an overview of the porosity found in the rods as well as on the reproducibility of the porous pattern within the cast rods. Secondly metallography is employed to validate the greyscale threshold to identify pores based on CT scans as will be shown later. The micrographs were taken with the light optical microscope Olympus AX70. The preparation of the samples to take micrographs is briefly explained in the following:
First the burr from the sample, which originates from the electric discharge machining is eliminated by grinding. Next the sample is placed in a plastic embedding form and embedded in epoxy resin. While the resin hardens the form is exposed to a vacuum atmosphere to eliminate voids within the embedding compound. Once the resin has hardened the embedded sample is labeled to avoid a wrong attribution of results. Now the sample is ground and polished. The samples are not etched before taking the micrographs since the contrast between pore and metal matrix is sufficient.

3.4 Computed Tomography of the Samples

3.4.1 Setup and Scanning Parameters

The CT scans presented within this work are taken at the Fraunhofer Institute in Fürth. The used CT system is shown in Figure 3.3. It consists of an YXLON FXE 225.99 panchromatic microfocus X-ray tube with a maximum voltage of 225 kV. The YXLON FXE 225.99 is equipped with a true X-ray intensity (TXI) control system, which ensures a high stability of the beam intensity over time by an adequate adjustment of the voltage applied to the X-ray tube. The X-ray tube is located 818 mm from the detector. The detector used in the CT setup is a *Perkin Elmer XRD 1620 AN Digital X-Ray Detector*. The detailed technical specification of the detector is presented in Table 3.2. The mechanical stage (cf. Section 2.2.2) enables a high precision manipulation of the sample. It allows to adjust the placement of the sample relative to the X-ray tube and the detector, as well as a rotation of the sample in order to acquire projections from different angels (cf. Figure 2.11).

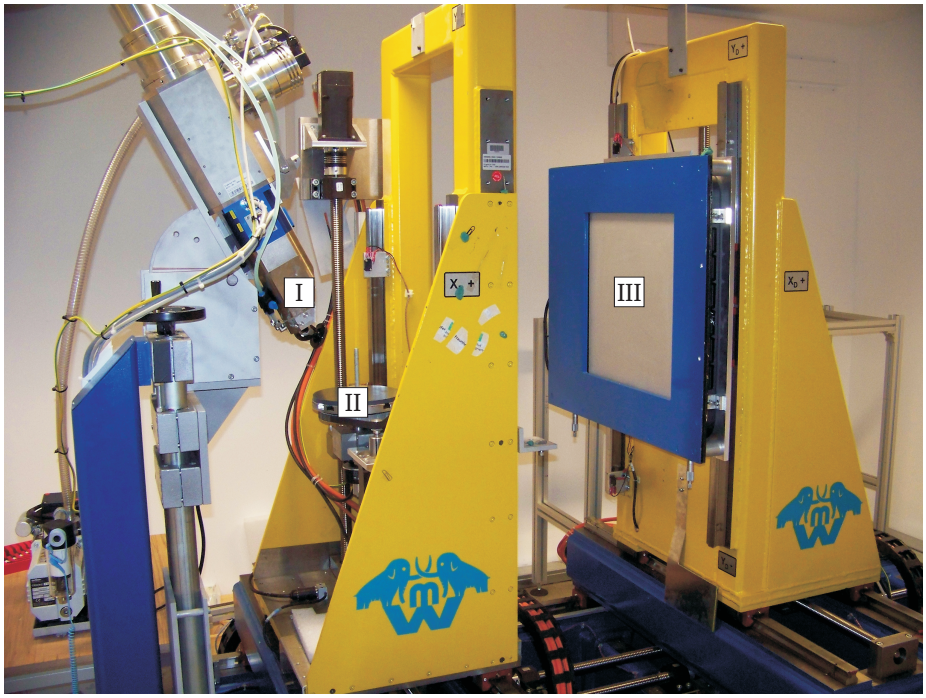

Figure 3.3: X-ray computed tomography setting at the Fraunhofer institute in Fürth. (I) YXLON FXE microfocus X-ray tube; (II) stage for the mechanical positioning of the sample; (III) Perkin Elmer XRD 1620 AN Digital X-Ray Detector.

Table 3.2: Technical Specifications of the XRD 1620 AN Digital X-Ray Detector.

Detector Specifications	
Scintillator screen	Lanex® Fine/Lanex® Fast
Pixel number	2048 x 2048
Active pixel number	2024 x 2024
Total area	409.6 x 409.6 mm^2
Diode capacity	2.1 pF
Integration time (minimum)	285.6 ms
Frame rate (max)	3.5 Hz
Radiation energy	40 keV - 15 MeV
Detector housing	672 x 599 x 44 mm^3

The dimensions of the investigated samples are $4\times4\times5\,mm^3$. For the CT scan a burr originating from the electrical discharge machining is left on one side of the sample (cf. Figure 3.2 (b)). The irregular geometry of the burr allows to relate the CT data to the sample. For the CT scans the samples were placed 18 mm from the focus and 800 mm from the detector resulting in a magnification of 44.4 times. From each sample 1600 projections were acquired over an angular range of 360 degrees. The spatial resolution of the CT scans was approximately 4.4 µm. Within this work a total of 10 samples were evaluated based on CT scans. An overview of the scan parameters is given in Table 3.3.

The accuracy of the CT scans is evaluated by comparing them with micrographs which is discussed in Section 3.4.2.

Table 3.3: Scan parameters for the CT scans.

Scan parameters	
Tube voltage	220 kV
Tube current	120 μA
Integration time	999 ms
Pre-filter	1 mm Cu
Number of projections	1600
Focus-Detector-Distance FDD	ca. 800 mm
Focus-Object-Distance FOD	ca. 18 mm
Magnification	ca. 44,4 times
Geometric resolution	ca. 4,4 μm
Ambient temperature	22 °C

3.4.2 Comparison of CT and Micrography Evaluation

As explained in Chapter 2, the grayscale threshold for the evaluation of the CT data decides if a voxel is interpreted as matrix material or as a pore. To validate the grayscale threshold for the evaluation of the CT data, a sample is scanned by means of CT and subsequently a cross sectional micrograph perpendicular to the longitudinal sample axis is taken at a predefined position. The position of the micrograph is chosen on the basis of the CT data analysis. It is crucial to select a slice of voxel from the CT data that exhibits noticeable features so that similarities can be identified in the cross sectional micrograph. After the CT scan, the sample is embedded and grinded to the predefined plane.
The micrograph shown in Figure 3.4 (a) is scaled to the same size as the slice extracted from the CT scan shown in Figure 3.4 (b). However, due to the sample preparation for the micrography minimal deviations in the location of the micrography plane compared to the CT plane are inevitable. Nevertheless a qualitative judgment of the accuracy of the grayscale threshold used to evaluate the CT data is possible. The pores detected within the CT scan (black regions) are also identifiable within the micrograph. The differences in the shape of the pores within the micrograph and the CT scan are due to the deviation of the cross sectional plane.

3.4.3 Pore Analysis and Detection Limits

The pores are identified and characterized based on the CT data. The projection of the sample does not cover the whole detector as shown in Figure 2.11, thus the CT data is

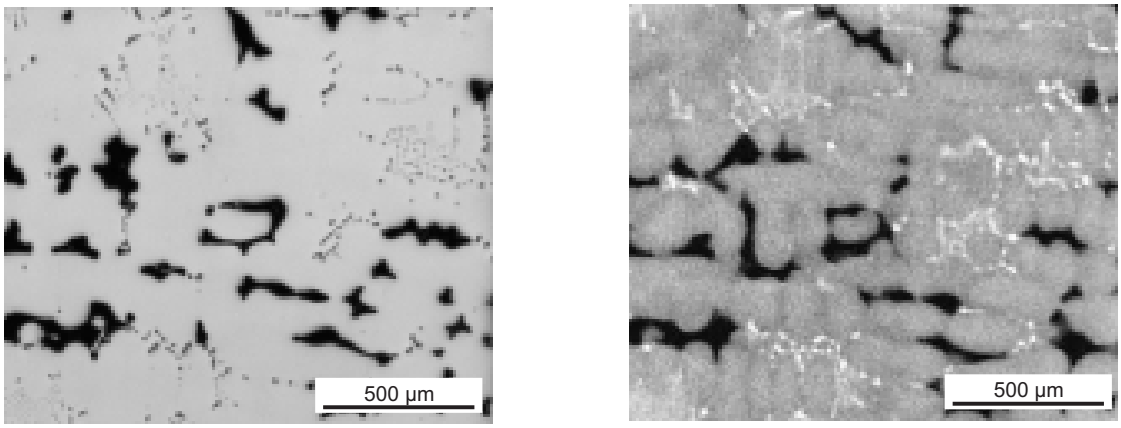

(a) (b)

Figure 3.4: Comparison of a cross sectional micrograph and a CT image of the same sample. The investigated cross sections slightly deviate due to the preparation of the micrograph: (a) Cross sectional micrograph obtained by LOM; (b) Cross sectional image obtained by CT (cf. [59]). The same pores can be identified within the two images. The slight deviation in the pore shape is due to the sample preparation, which hinders to evaluate exactly the same cross section.

preprocessed decreasing the size of the raw data file by eliminating the area surrounding the sample. This allows for an efficient evaluation of the CT scan.

After reducing the file size of the CT data, an algorithm to identify pores is applied. The voxels are separated into matrix and pore voxels using a grayscale threshold. This results in a binarized graph of black and white voxel. A region is recognized as a pore if a minimum of at least 40 adjacent voxel are identified as pore-voxel. For two voxel to be termed adjacent they have to share one face. The threshold of 40 adjacent pore-voxel to actually be counted as a pore represents a minimum volume for recognizable pores of just over 3400 μm^3. This prevents measuring noise from being interpreted as a pore.

The results of this data analysis are written to a text file, where the centroid coordinates, the pore volume as well as the bounding box dimensions are stored for each pore. This data provides the basis to evaluate the pore volume distribution, the spatial pore distribution as well as the pore shape which will be discussed in the following.

3.4.4 Pore Volume Distribution

The pore volume distribution is evaluated based on the CT data of the porous samples with a minimum identifiable pore volume of 3400 μm^3. The identification of smaller pores is hindered by the measuring noise of the CT data.

The relative frequency of single pore volumes is analyzed using histograms with a bin width of 40 voxel or 3400 μm^3. The bin height is normalized by the total number of pores

found within the sample so that the bin height corresponds to the probability of a pore to be found in a particular bin. The pore volume distribution is fitted using analytical probability density curves. The Lognormal distribution

$$f(x) = \frac{e^{\left(-\frac{1}{2}\left(\frac{lnx-\mu}{\sigma}\right)^2\right)}}{x\sigma\sqrt{2\pi}}\,, \tag{3.1}$$

which is commonly used for an analytical description of the volume distribution of inclusions as well as the Weibull distribution

$$f(x) = \frac{\alpha}{\beta}\left(\frac{x}{\beta}\right)^{\alpha-1} e^{-\left(\frac{x}{\beta}\right)^{\alpha}}\,, \tag{3.2}$$

which Waters [47] found adequate to describe pore volume distributions, are fitted to the experimentally determined pore volume distribution. In Equations (3.1) and (3.2) $f(x)$ is the probability density; (μ, σ) and (α, β) are the parameter pairs to fit the distributions. The experimentally obtained histogram and the fitted probability density curves of the Weibull and Lognormal distribution for the pores identified within sample 4-04 are shown in Figure 3.5. Both distributions match the histogram. A comprehensive overview

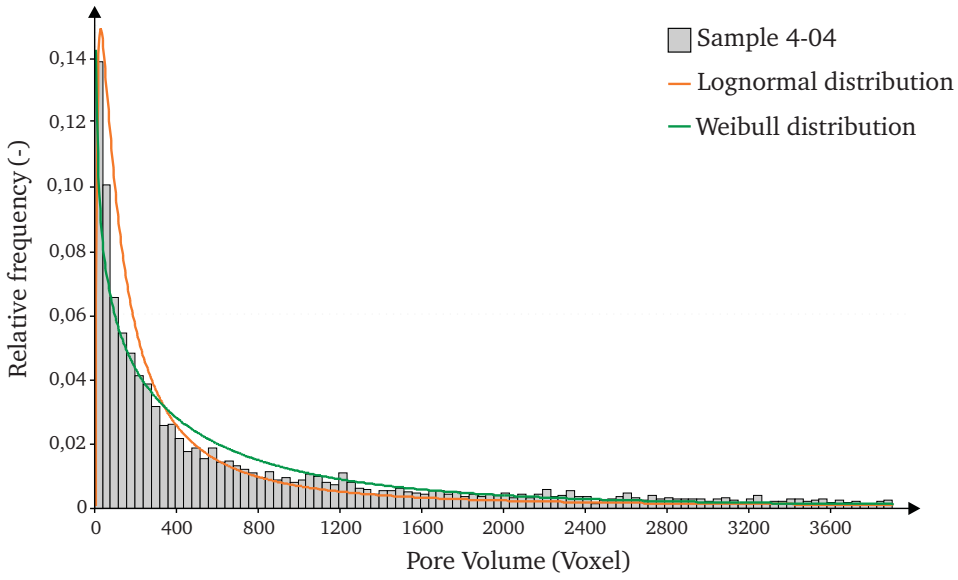

Figure 3.5: Pore volume distribution in sample 4-04. The relative pore volume density resulting from the experimental investigation is fitted by a Lognormal distribution and a Weibull distribution.

of the Lognormal and Weibull parameters to fit the pore volume distributions of all samples investigated by CT along with the pore volume fraction of the particular sample is presented in Table 3.4. The accuracy of the Weibull and the Lognormal fit to the observed pore volume distribution is compared based on the Kolmogorov Smirnov statistics. The

Kolmogorov Smirnov statistics identifies the maximum vertical deviation between the experimental and theoretical cumulative distribution function. In case of the investigated samples the Lognormal distribution provides the better fit to the observed pore volume distribution. A graphical representation of the relation between fitting parameters and

Table 3.4: Weibull (Wb) and Lognormal (Ln) fit parameters for the pore volume distribution. The accuracy of the fitted distributions is compared based on the Kolmogorov - Smirnov statistic which is based on the maximum vertical difference of the fitted and the experimental cumulative distribution function.

Sample number	Pore volume fraction (vol. %)	Weibull params. α	β	Lognormal params. μ	σ	Kolmogorov - Smirnov (Wb/Ln)
2-01	5.31	0.65	1788.3	6.61	1.74	0.13/0.06
3-01	8.97	0.64	2075.7	6.73	1.81	0.12/0.08
3-02	7.88	0.65	1190.7	6.47	1.79	0.13/0.09
3-03	7.60	0.69	523.8	5.43	1.40	0.24/0.18
4-01	9.56	0.59	1205.3	6.12	1.81	0.18/0.14
4-02	12.37	0.65	2197.0	6.81	1.79	0.12/0.07
4-03	11.83	0.61	2086.1	6.70	1.87	0.14/0.09
4-04	5.75	0.70	1461.4	6.47	1.63	0.13/0.08
5-01	26.22	0.63	1133.8	6.25	1.49	–

the pore volume fraction for the Lognormal distribution is presented in Figure 3.6. The dependencies of μ and σ on the pore volume fraction is shown in Figure 3.6 (a) and Figure 3.6 (b), respectively which can be adequately described by linear regressions,

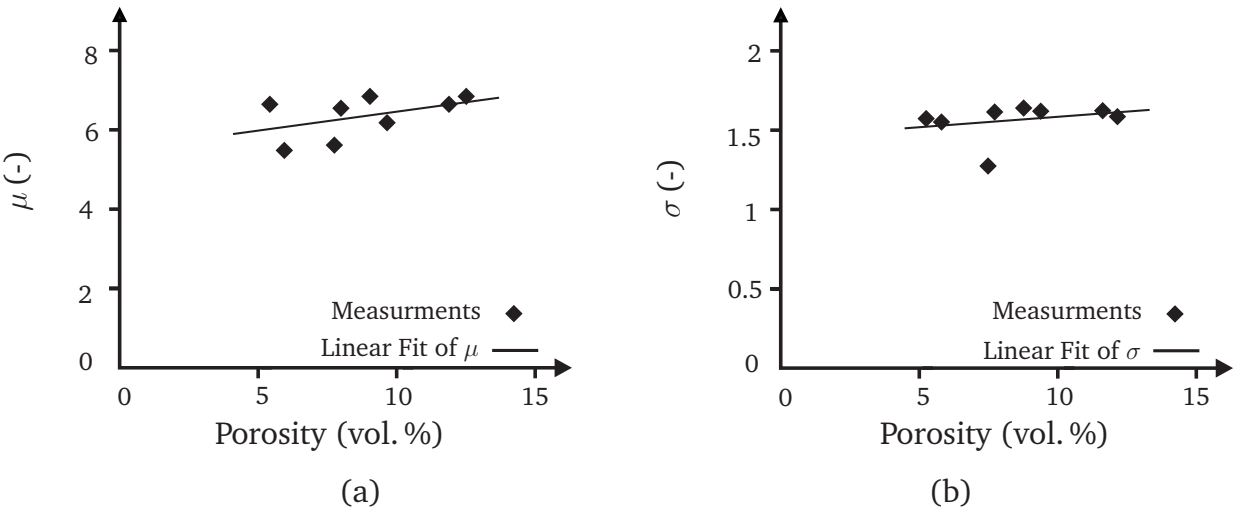

Figure 3.6: Parameters for the fit of a Lognormal distribution to experimentally obtained pore volume distributions: (a) Correlation of the parameter μ with the volume porosity; (b) Correlation of the parameter σ with the volume porosity.

$$\mu = 5.968 + 0.052 \cdot v_{\mathrm{p}} \tag{3.3}$$

and

$$\sigma = 1.484 + 0.028 \cdot v_{\mathrm{p}} \; . \tag{3.4}$$

The dependency of the Weibull parameters on the pore volume fraction is presented in Figure 3.7. Again the parameters are approximated by a linear regression. The parameter β exhibits a large scatter. The maximum deviation of the measured parameters compared to the linear fit is 17.5 % for the parameters of the Lognormal distribution and 64.0 % for the parameters of the Weibull distribution. Based on the accuracy of the Weibull and Lognormal fit and the scatter of the fit parameters the Lognormal distribution is favored to describe the pore volume distribution in this study. A small scatter of the fit parameters is important for running parameter studies (cf. Chapter 4.2), since this means that the observed pore volume distribution does not significantly deviate from the input data for the model generation which is defined according to the linear regressions given above.

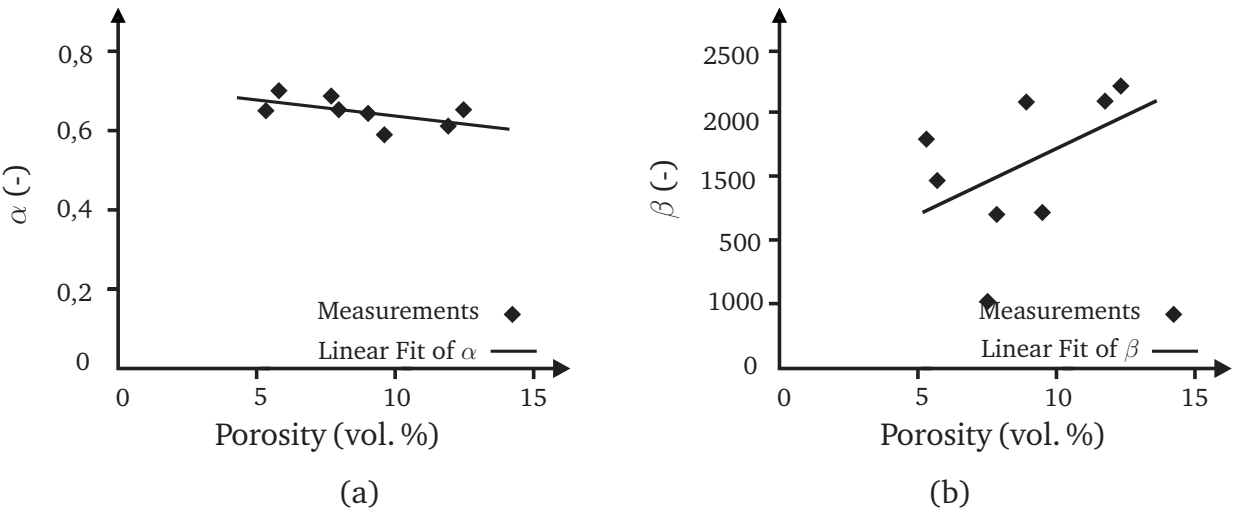

Figure 3.7: Parameters for the fit of a Weibull distribution to experimentally obtained pore volume distributions: (a) Correlation of the parameter α with the volume porosity; (b) Correlation of the parameter β with the volume porosity.

3.4.5 Nearest Neighbor Distance

The nearest neighbor distance is an easily accessible quantity to characterize the spatial distribution of particles. In the present study, the deviation of the observed pore distribution from a random distribution is measured. For this purpose the nearest neighbor distance of individual pores is evaluated. The observed mean nearest neighbor distance of the pores is then compared to a the mean nearest neighbor distance of a set of ran-

domly distributed points. This approach has been used by Clark and Evans [60] to analyze spatial distributions in 2D, but it can be generalized to 3D.

The distance d between two individual pores is calculated by using the Euclidean metric

$$d = \sqrt{(x_i - x_j)^2 + (y_i - y_j)^2 + (z_i - z_j)^2}\,, \tag{3.5}$$

where the subscript i denotes the centroid coordinates of the i^{th} pore, and the subscript j denotes the centroid coordinates of the j^{th} pore. The centroid coordinates are evaluated for each pore based on the CT data. The distance of the i^{th} pore to any other pore is calculated using Equation (3.5). The shortest distance is called nearest neighbor distance d_{min}. After calculating the nearest neighbor distance for every individual pore i in a sample, the mean nearest neighbor distance r_{A} is obtained by

$$r_{\text{A}} = \frac{1}{n}\sum_{i=0}^{n} d_{\text{min}}\,, \tag{3.6}$$

where n is the number of pores.

The calculation of the mean nearest neighbor distance of randomly distributed points is based on the nearest neighbor distribution density function $p(r)$. According to Torquato [61], $p(r)$ can be written as

$$p(r) = \eta 4\pi r^2\, e^{(-\eta\frac{4}{3}\pi r^2)}\,, \tag{3.7}$$

in 3D where η is the pore density (cf. Table 3.5). The mean nearest neighbor distance r_{E} for randomly distributed points is defined as

$$r_{\text{E}} = \int_0^\infty r\, p(r)\, \mathrm{d}r \;=\; \int_0^\infty r 4\eta\pi r^2\, e^{(-\eta\frac{4}{3}\pi r^2)}\, \mathrm{d}r\,. \tag{3.8}$$

Following Waters [47], solving Equation (3.8) yields

$$r_{\text{E}} = 0.812(\pi\eta)^{-\frac{1}{3}}\,. \tag{3.9}$$

The mean nearest neighbor distance r_{E} is a function of the pore density η obtained by dividing the number of pores by the sample volume.

With the aid of r_{E} and r_{A}, the degree of randomness

$$R = \frac{r_{\text{A}}}{r_{\text{E}}} \tag{3.10}$$

is calculated as the ratio between the two values. A random pore distribution yields $R = 1$ where the observed mean nearest neighbor distance coincides with the mean nearest neighbor distance of randomly distributed points. Furthermore $R < 1$ indicates

an aggregation of pores within the evaluated volume. In this case the mean nearest neighbor distance of the pores found within the sample volume is below the mean nearest neighbor distance of randomly distributed points. A degree of randomness $R > 1$ indicates an ordered distribution of pores. This can be imagined e.g. as pores located at the corners of a cubic lattice. The ratio R is evaluated for each sample (Table 3.5). Furthermore the results for the observed mean nearest neighbor distance r_{A} of pores and the mean nearest neighbor distances r_{E} for randomly distributed points are presented in Table 3.5. The distribution of the pores is nearly random in all cases except for sample 5-01. The evaluation of sample 5-01 was generally difficult, since the large pore volume fraction hindered the identification of individual pores. However, regarding the evaluation of the spatial pore distribution one needs to keep in mind that the randomness of spatially distributed pores largely depends on the boundaries of the evaluated space. Within a confined region of a cast part, porosity might be distributed fairly random as e.g. in the cast samples investigated within this study. If one considers the whole casting the pore distribution will be markedly non-random. This problem will be tackled in more detail in Chapter 4.3.

Table 3.5: Evaluation of the distribution of the porosities within the samples based on the nearest neighbor distance.

Sample number	Pore volume (vol. %)	Pore density $\left(\frac{1}{\mathrm{mm}^3}\right)$	Evaluated mean distance (μm)	Calculated mean distance (μm)	Degree of randomness R
2-01	5.31	80.92	121.54	128.18	1.05
3-01	8.97	47.71	140.87	152.86	1.09
3-02	7.88	77.74	120.92	130.47	1.08
3-03	7.60	181.54	83.24	97.92	1.18
4-01	9.56	61.44	120.66	140.51	1.16
4-02	12.37	40.83	139.85	161.01	1.15
4-03	11.83	40.80	144.79	161.05	1.11
4-04	5.75	79.51	128.93	114.17	1.13
5-01	26.22	13.11	166.75	235.11	1.41

3.4.6 Pore Shape

As mentioned in Chapter 2.2 the goal is to develop a parameterizable pore model based on primitive geometries. The identification of a parameter describing the real pore geometry is vital to derive such a model geometry. Many micromechanical finite element approaches use spheres [47] or ellipsoids to represent the geometry of the inclusions within a matrix material [62, 63, 22, 24].
However, the pores in the nickel base cast alloy MAR-M247 have complex geometries with both convex and concave radii as shown in Figure 3.8. Thus a more complex ge-

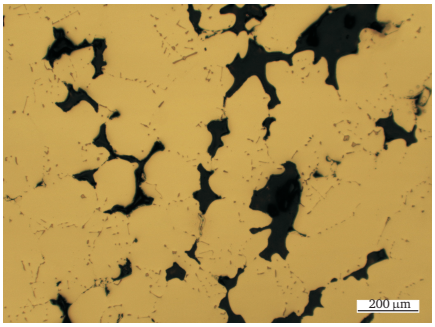

Figure 3.8: The micrograph shows the complex geometries of the pores present in the MAR-M247 cast alloy. It can be seen that the pore geometry is highly irregular.

ometry to represent the pores, which is still parameterizable is sought after. To represent both convex and concave radii a Boolean model of intersecting ellipsoids is proposed to model the pores, which consists of three identical rotational ellipsoids arranged mutually perpendicular around a common center as presented in Figure 3.9. A further advantage of the proposed pore model is its capability to represent the spatial ramification of pores by adequately adjusting the aspect ratios of the ellipsoids. The ramification of real pores

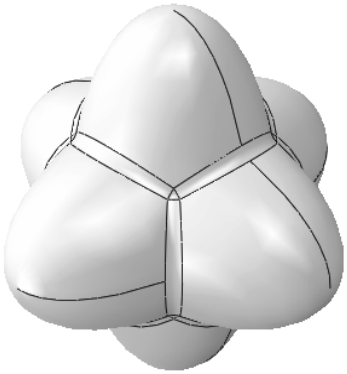

Figure 3.9: Proposed three dimensional Boolean pore model. Three equal rotational ellipsoids are arranged mutually perpendicular to each other around a common center. The pore model allows the representation of both convex and concave radii as well as the spatial ramification of pores found within MAR-M247.

is characterized by the ratio of the bounding box volume V_{BB} to the actual pore volume V_{Pore} as schematically presented in Figure 3.10. The bounding box is the smallest cube enclosing a pore. The dimensions of the bounding box as well as the pore volume are obtained from the CT data. The volume ratio

$$\mathrm{V_R} = \frac{V_{\mathrm{BB}}}{V_{\mathrm{Pore}}} \tag{3.11}$$

increases with an increasing ramification of the pore. It is represented by the Boolean pore model through adjusting the aspect ratio of the individual ellipsoids (cf. Chap-

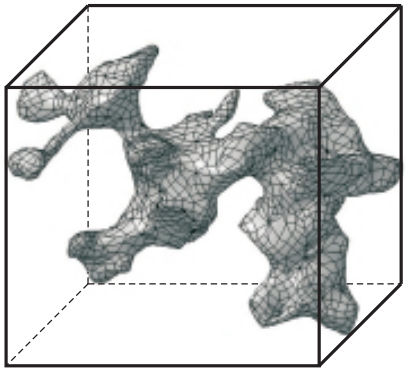

Figure 3.10: Schematic representation of bounding box and pore volume. The bounding box is the smallest cube enclosing the pore. The ratio of bounding box and pore volume is used to characterize the spatial ramification of the pore.

ter 4.2). The higher the volume ratio, the higher is the aspect ratio of the ellipsoids used for the Boolean pore model.

The limit volume ratio, which can be represented by the proposed Boolean pore model is given by a spherical pore. It can be calculated as

$$\mathrm{V_R} \;=\; \frac{a^3}{\frac{4}{3}\,\pi\,(\frac{a}{2})^3} \;=\; 1.91\;. \tag{3.12}$$

A histogram of the volume ratio of pores within the sample 4-04 is presented in Figure 3.11. The relation of the volume ratio and the aspect ratio of the model pore geometry is presented in Figure 3.12. With the use of this relation, each volume ratio obtained from the experimental evaluation of pore volume and bounding box volume is converted into an aspect ratio of the model pore. The resulting distribution of aspect ratios for the pore model is again characterized using a Lognormal distribution. The results obtained for the porous cast samples investigated within this work are given in Table 3.6. It can be seen that the parameters to fit a Lognormal distribution characterizing the aspect ratios only slightly vary for pore volume fractions between approximately 5 % to 13 %. This seems not to be the case for considerably higher pore volume fractions (cf. the Lognormal parameter μ for the aspect ratio distribution of pores within sample 5-01). However, based on the evaluation of the aspect ratios the parameters

$$\mu = 0.712 - 0.009 \cdot v_\mathrm{p} \tag{3.13}$$

and

$$\sigma = 0.456 + 0.003 \cdot v_\mathrm{p}\,, \tag{3.14}$$

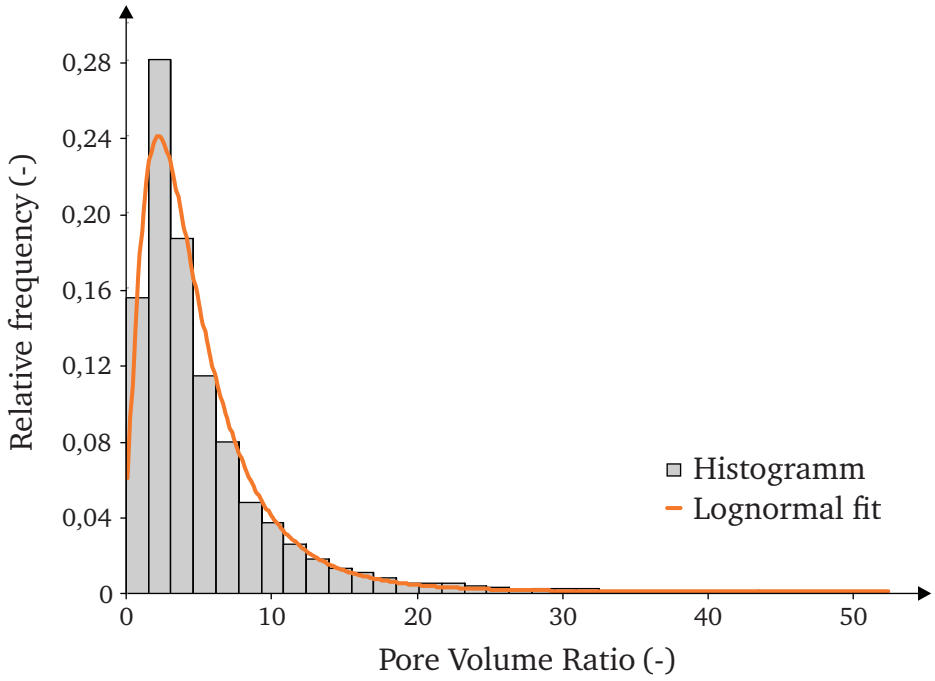

Figure 3.11: Histogram of pore volume ratios evaluated from CT data of the sample 4-04. The higher the pore volume ratio, the more spatially ramified is the pore.

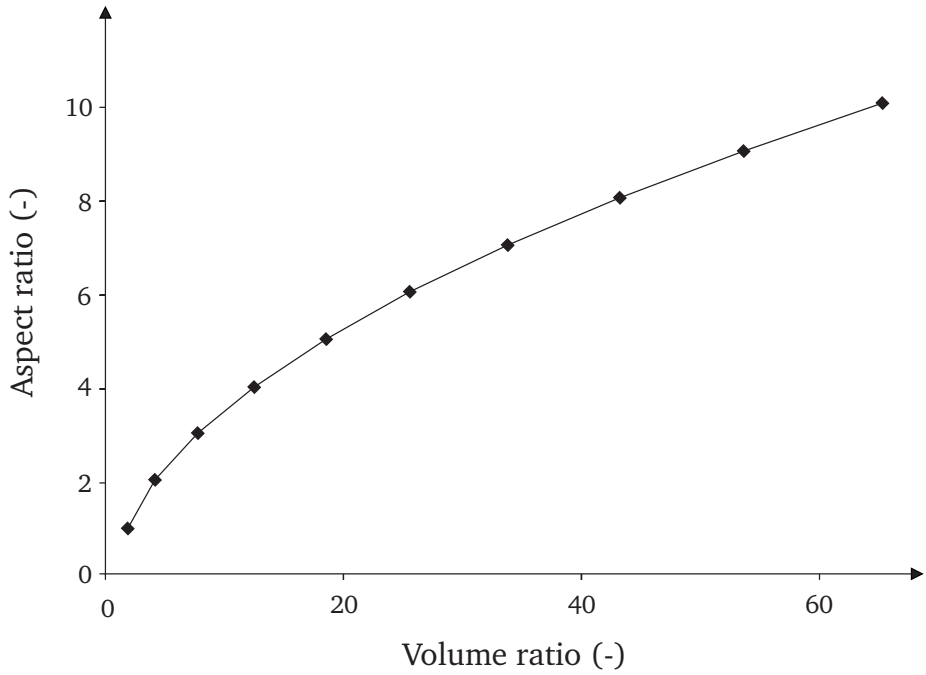

Figure 3.12: Correlation of Volume and aspect ratio: The volume ratio of a pore obtained from the experimental evaluation can be represented by the proposed three dimensional Boolean pore model (cf. Figure 3.8) by adjusting the aspect ratio of the three rotational ellipsoids. The diagram shows the correlation of the volume ratio of pores found in the sample and the aspect ratio of the ellipsoids for the Boolean pore model.

Table 3.6: Evaluation of the pore shape based on the aspect ratios of pores within the investigated samples.

Sample number	Pore volume fraction (vol. %)	Lognormal distribution parameters μ	σ
2-01	5.31	0.64	0.53
3-01	8.97	0.70	0.50
3-02	7.88	0.75	0.46
3-03	7.60	0.61	0.42
4-01	9.56	0.58	0.48
4-02	12.37	0.59	0.50
4-03	11.83	0.58	0.51
4-04	5.75	0.62	0.47
5-01	26.22	1.14	0.67

defining the Lognormal distribution of model pore aspect ratios for materials with pore volume fractions between 5 % and 15 % are calculated by linear regressions.

3.5 Mechanical Testing of the Samples

Compression tests are performed to capture the influence of pores on the offset yield stress and the plastic behavior of the sample material. The compression tests are carried out with the deformation dilatometer DIL 805 developed by *Bähr Thermoanalyse* (see Figure 3.13).

The sample is clamped between two aluminum oxide Al_2O_3 rams. The length change

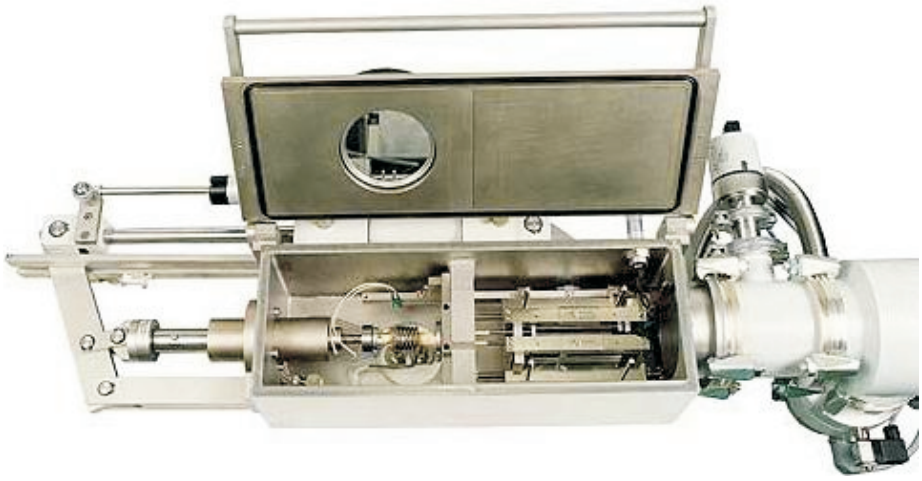

Figure 3.13: Deformation dilatometer from *Bähr Thermoanalyse* used for the compression tests presented within this work.

of the sample during testing is recorded by push rods, which are propped against the rams. To reduce the jigging of the sample, a preload of 3.000 N is applied for a duration of 30 seconds. Then the preload is reduced to 200 N and the actual experiment starts. The sample is loaded at a loading rate of 20 $\frac{\mathrm{N}}{\mathrm{mm}^2}$. The compression force is continuously ramped up to 14.400 N. Taking the sample dimensions into account this equals a first Piola Kirchhoff stress of 900 $\frac{\mathrm{N}}{\mathrm{mm}^2}$ which exceeds the initial yield stress as required by the DIN standard [58]. Next, an unloading and loading hysteresis is performed. The compression force is decreased to 6.000 N before the load is increased again to the final compression load of 16.000 N. A schematic representation of the loading curve over time is presented in Figure 3.14. Due to the slight jigging of the sample while loading, the

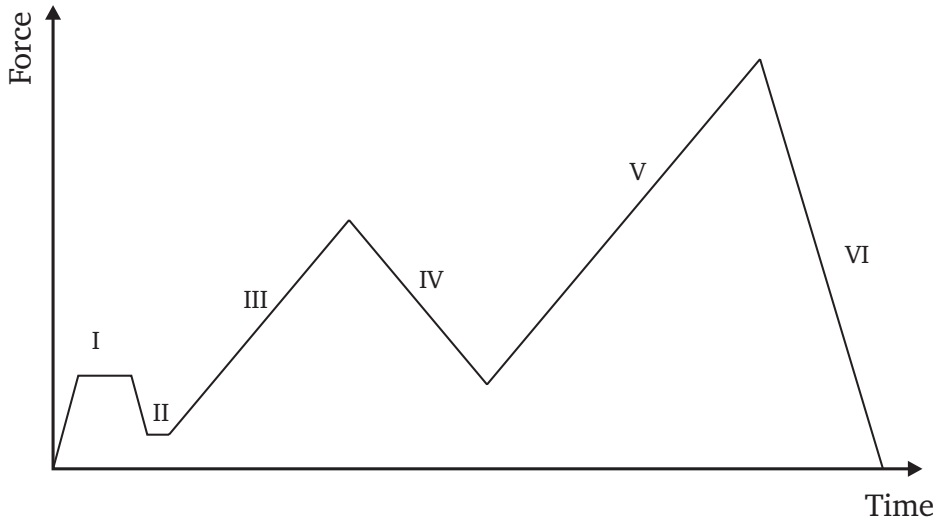

Figure 3.14: Schematic representation of the load vs. time curve for the compression tests: (I) preload sample with 3000 N to minimize jigging ; (II) reduce preload before mechanical testing to 200 N; (III) ramp force to 14.400 N; (IV) unloading; (V) increase load to final force of 16.000 N; (VI) final unloading and end of experiment.

slope of the linear elastic region cannot be determined accurately. Thus the slope of the linear elastic range of the stress-strain curve is obtained from the mean slope of the unloading-loading hysteresis as stipulated in [58] (cf. Section 2.2.3). The jigging of the sample observed at stress values below 400 $\frac{\mathrm{N}}{\mathrm{mm}^2}$ is eliminated by an extrapolation using the slope obtained from the hysteresis. This procedure leads to a stress strain curve as is depicted in Figure 3.15. To evaluate the offset yield stress, the elastic slope determined from the hysteresis is shifted to a strain of 0.002. The offset yield stress is evaluated using the method described in Section 2.2.3. The evaluation of the recorded data is automated using Python scripting. The offset yield stresses obtained from the tested samples are given in Table 3.7. In Figure 3.16 the stress strain curves from three different samples are compared. It can be seen that the offset yield stress is significantly influenced by the

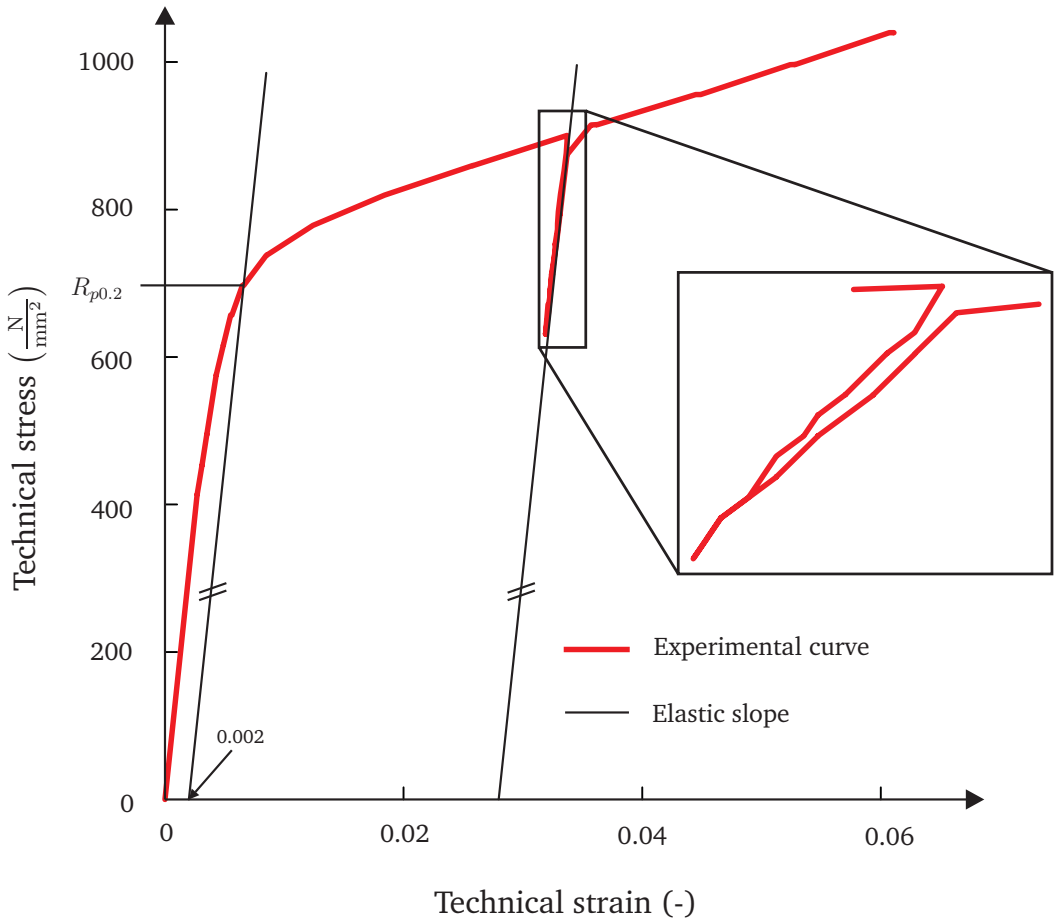

Figure 3.15: Stress Strain curve obtained from the compression tests. The slope of the elastic regime is determined as the mean slope of the unloading – loading hysteresis shown in the detail of the graph. The yield stress is obtained from the intersection of the experimental stress strain curve with the parallel translated elastic slope.

pore volume fraction of the tested sample. The dependency of the offset yield stress on the pore volume fraction for a larger set of samples is shown in Figure 3.17.

Table 3.7: Offset yield stress determined from the compression tests.

Sample number	Pore volume fraction (vol. %)	$R_{p0.2}$ $\left(\frac{N}{mm^2}\right)$
1-01	0.00	860
2-01	5.31	800
3-01	8.97	620
3-02	7.88	600
3-03	7.60	720
4-01	9.56	610
4-02	12.37	520
4-03	11.83	580
4-04	5.75	720
5-01	26.22	–

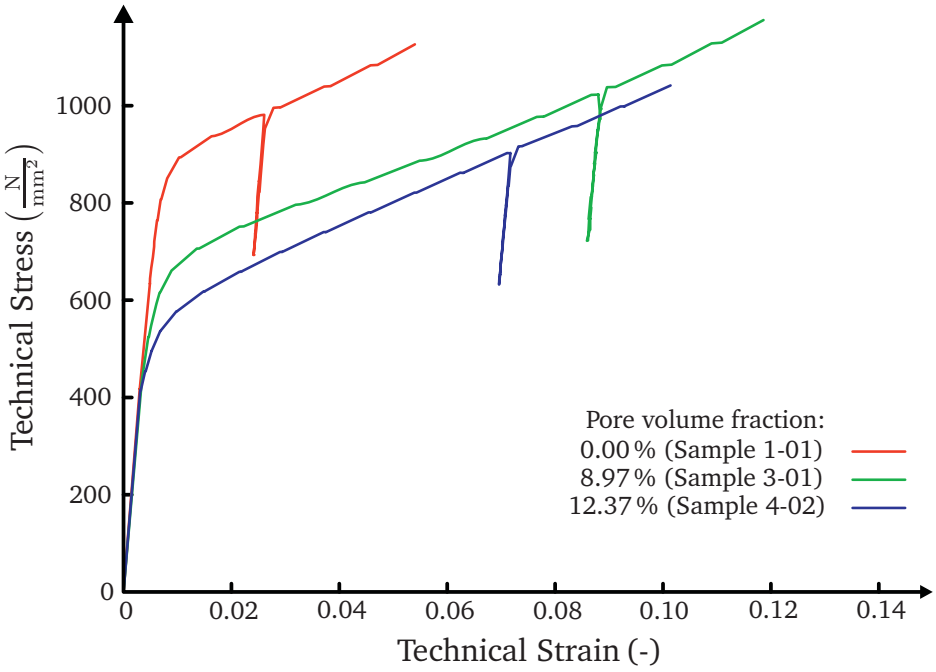

Figure 3.16: Stress strain curves obtained from compression tests at room temperature for three samples featuring different pore volume fractions. The yield stress is significantly influenced by the pore volume fraction, whereas the elastic region as well as the hardening behavior is quite similar for the three samples.

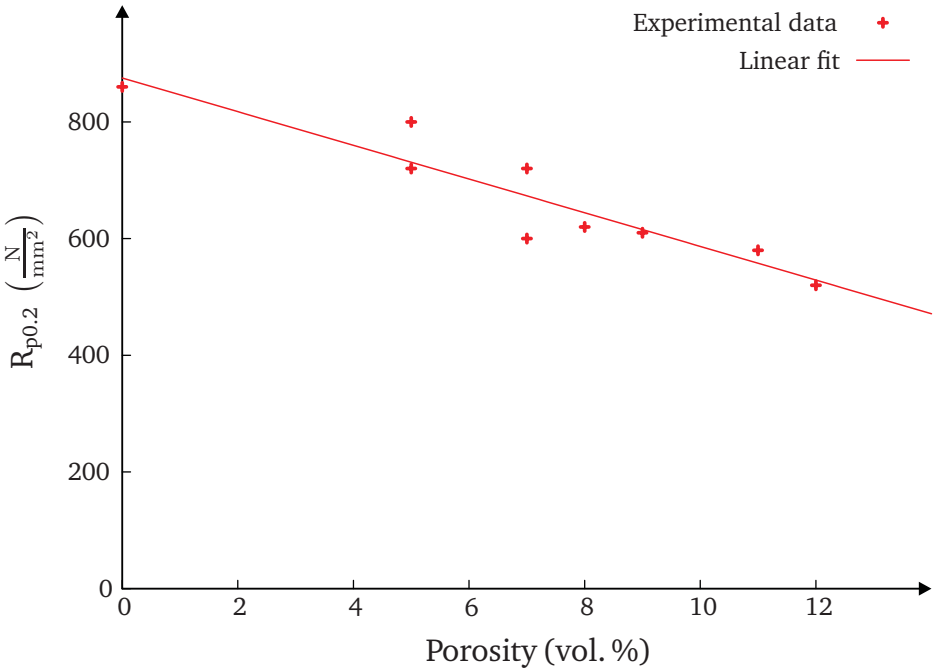

Figure 3.17: The dependence of the 0.2 % offset yield stress on the volume porosity of the samples. Clearly, the yield stress decreases with increasing porosity.

Chapter 4

Finite Element Models – Development and Evaluation

The heterogeneous microstructure of engineering materials has a substantial influence on their mechanical behavior. The finite element method (FEM) is a powerful tool to study this influence by modeling a sufficiently large section of the material microstructure, which can then be called a representative volume element (RVE) [7, 29, 30].
The macroscopic constitutive behavior of a heterogeneous material is derived employing so-called computational homogenization to the RVE models [7]. However, one has to be careful when using homogenized constitutive laws for macroscopic component layouts. The homogenized constitutive laws are only valid as long as the microstructure is invariant within the component. Furthermore, the constitutive behavior has to be independent from the loading path. These limitations can be overcome by employing a so called concurrent multiscale approach. The idea is to run macroscopic and microscopic FE models in parallel, where the macroscopic constitutive response is provided by the underlying RVE models accounting for the local microstructure and loading path.
In this chapter the microscopic FEM model examining the influence of pores on the mechanical behavior of nickel-base cast alloys is presented. Furthermore, a concurrent multiscale approach to incorporate the micromechanical model in a macroscopic FE calculation as well as a sequential multiscale model is introduced.

4.1 Definitions and Modeling Assumptions

The nickel base cast alloy MAR-M247 is assumed to be homogeneous on the macroscopic level. On the microscopic level however, MAR-M247 is heterogeneous consisting of the metal matrix and finely dispersed pores as schematically represented in Figure 4.1. Depending on the location on the macroscopic level, the respective microstructure can vary,

but there is no abrupt change of the microstructure in the near surrounding of a macroscopic point. The assumption of a homogeneous macro and heterogeneous microscale

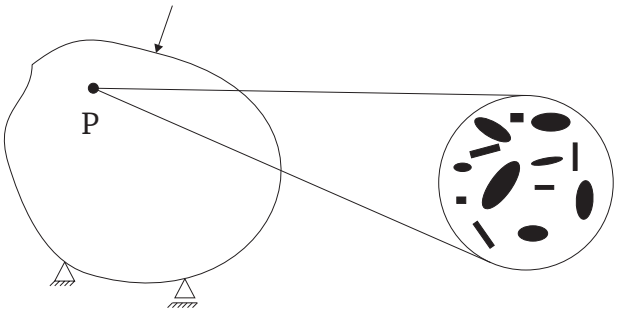

Figure 4.1: The macroscopic component is assumed to be homogeneous. However the continuum exhibits a heterogeneous microstructure consisting of matrix material and pores (cf. [7]) as shown for an arbitrary point **P**. Depending on the location, the microstructure can vary, but there is no abrupt change of the microstructure in the near surrounding of any point in the macroscopic structure.

relies on the principle of scale separation where the – actually heterogeneous – material is imagined as homogeneous on a macroscopic level because the heterogeneities cannot be resolved by the eye of the observer [64]. To characterize this statement mathematically Ostoja-Starzewski [64] introduced three distinct length scales:

- the characteristic length of the component L_{C},
- the size of the modeled volume element L_{VE},
- the average dimension of the microscopic inclusions L_{m}.

The principle of scale separation requires for the characteristic component length L_{C} to be much larger than the modeled micromechanical volume element length L_{VE},

$$L_{\mathrm{C}} \gg L_{\mathrm{VE}} \,. \tag{4.1}$$

The necessary scale separation between L_{VE} and L_{m} to obtain converged results from a micromechanical model depends on the microstructure of the considered material. For a strictly periodic microstructure the inequality $L_{\mathrm{VE}} > L_{\mathrm{m}}$ is sufficient to obtain convergent results. Unfortunately, the pore distribution within MAR-M247 is spatially random, which requires a more strict scale separation between L_{VE} and L_{m} written as

$$L_{\mathrm{VE}} \gg L_{\mathrm{m}} \,. \tag{4.2}$$

The micromechanical model to capture the influence of pores on the macroscopic material behavior of the cast alloy considers two phases – the metal matrix phase and the pore

phase. To model the constitutive behavior of the metal matrix the von Mises plasticity (J_2 plasticity) theory is employed.

There are multiple ways to convey the results obtained by micromechanical modeling to the macroscale. An easy and industrially applicable way to proceed is to fit the constitutive behavior of the macroscale on the basis of homogenized results obtained from the heterogeneous micromechanical model (cf. Section 4.3.1). However, this straight forward approach of transferring the constitutive behavior from the microscale to the macroscale is only valid as long as

- the component's microstructure is invariant with certain regions, and
- the loading path does not influence the constitutive behavior.

Within this work a remedy to bypass these limitations is presented by introducing a concurrent multiscale approach (cf. Section 4.3.2). Each integration point of the macroscopic FE simulation is attached to a micromechanical volume element model, which provides the macroscopic constitutive behavior according to the loading path and microstructure at the respective location. This accounts for a differing microstructure on different macroscopic points, where in the vicinity of the point the microstructure is still assumed periodic as presented in Figure 4.2. Furthermore, the concurrent multiscale approach enables to considers loading path dependencies in the constitutive behavior. The multiscale framework of both, the concurrent and the sequential approach are pre-

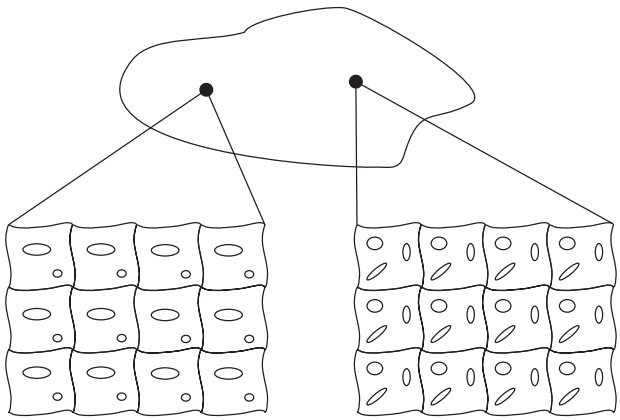

Figure 4.2: Representation of a microstructure with local periodicity. Different macroscopic material points exhibit a varying microstructure (cf. [7]).

sented in more detail in Section 4.3. The concurrent multiscale approach is computationally expensive; nevertheless, with increasing computer capacity and availability of cloud computing such elaborate analysis methods are becoming more and more attractive. Moreover, the computational cost can be limited by a selective use of the multiscale models at critical regions only, whereas a standard continuum approach is employed for the remaining structure as was proposed by Ghosh [62].

4.2 Micromechanical Finite Element Model

At the microscale level, there are two common ways to derive finite element geometry models: Real microstructure phase arrangements derived from three dimensional CT and micro-graphs, and computer-generated geometries. This work pursues the latter approach using computer-generated geometries. One advantage of computer-generated microstructure models over geometries derived from the real microstructure is that the former enable parametric studies. The goal of the micromechanical modeling approach is to replicate the characteristics of the pores utilizing a computer-generated pore model.

4.2.1 Volume Element Model Generation

To achieve reliable results it is important for the microstructure model to represent the relevant characteristics of the materials microstructure. Within this work the characteristics accounted for are limited to the accumulated volume of the inclusions, the volume distribution of individual inclusions, the shape of single inclusions in terms of the ratio between bounding box volume and pore volume, as well as the spatial distribution of the inclusions within the modeled volume element. These characteristics were obtained from detailed studies of 3D CT images of nickel-base cast alloy samples as presented in Section 3.4 with the results briefly summarized in the following. The volume distribution of single inclusions is statistically characterized utilizing Lognormal distributions with minimum and maximum thresholds. The pore topologies in the model are based on a Boolean union of parameterized rotational ellipsoids with their major axes arranged mutually perpendicular around their common geometric center, as presented in Figure 4.3. The abstract pore shape accounts for the ramification of interdentritic pores found in the MAR-M247 cast alloy samples. The ramification is characterized by the volume ratio V_{R} of the bounding box volume to the pore volume. The intersection of the ellipsoids representing the pores are rounded by concave radii to avoid singularities in the stress distribution of the finite element solution. The intersection radius

$$r_{\mathrm{int}} = \frac{1}{10}\, a_{\mathrm{ha}}\,, \tag{4.3}$$

depends on the major axis length a_{ha} of the rotational ellipsoids of the Boolean pore model. In addition to the shape and volume of individual pores, their spatial distribution is an important parameter that governs the resulting materials properties. The spatial distribution is experimentally characterized utilizing a coefficient for the spatial randomness of pores found in a sampled volume (cf. Section 3.4.5).

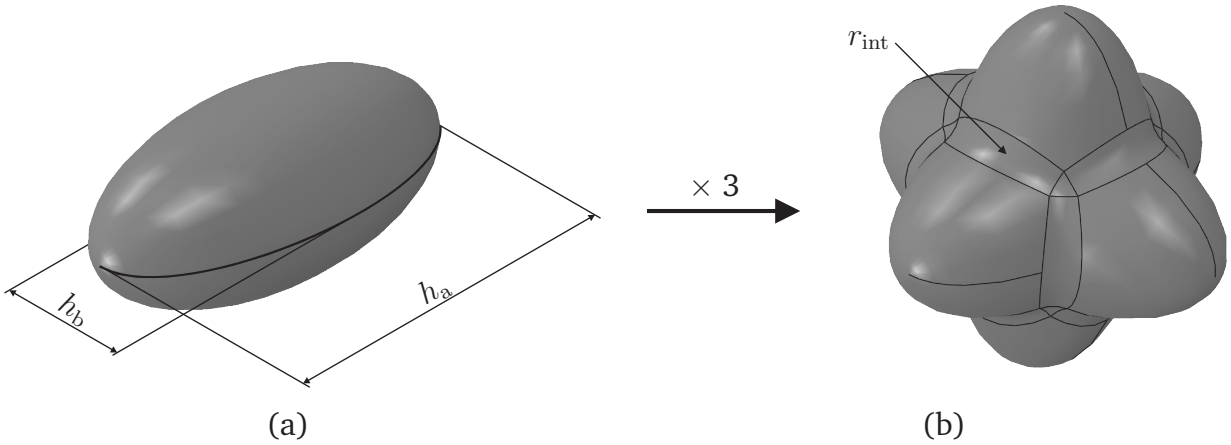

Figure 4.3: Representation of the Boolean pore model: a) The rotational ellipsoid with the axis lengths h_{a} and h_{b}; b) Boolean union of three equivalent rotational ellipsoids arranged mutually perpendicular around a common geometric center. The intersection of the individual ellipsoids are rounded by the concave radius (r_{int}) to avoid singularities in the stress distribution of the finite element solution (cf. [65]). The aspect ratio of the single rotational ellipsoids governs the volume ratio V_{RMP} of the smallest cube enclosing the model pore and the volume of the model pore.

An algorithm that automatically generates microstructures according to the aforementioned parameters is implemented using the programming language Python. The algorithm requires the experimentally determined shape and volume distributions of the pores, the pore volume fraction and information about the spatial distribution of the pores as input parameters. The generated geometry model is designed to be suitable for the periodic microfield approach (PMA) as described by Böhm [66]. PMA assumes that the whole material exhibits a geometric periodicity, which corresponds to a periodic arrangement of the modeled microstructural volume element. Therefore the spatial distribution of pores within the volume element model is governed by an algorithm similar to the random sequential adsorption described by e.g. Torquato [67], which is enhanced by taking the spatial periodicity into account. When a pore penetrates the surface of the modeled volume element, an equivalent pore with the same spacial orientation and aspect ratio is placed on the opposing side of the volume element as shown in Figure 4.4. The algorithm to generate the parameters required to set up the micromechanical volume element model can be divided into the following steps.

1. Definition of individual pore volumes: The volumes of individual pores are successively defined based on a Lognormal distribution with minimum and maximum thresholds. The cumulative pore volume is calculated after each definition of an individual pore volume. This procedure is repeated until the cumulative pore volume fraction is within the defined tolerance of the target pore volume fraction.

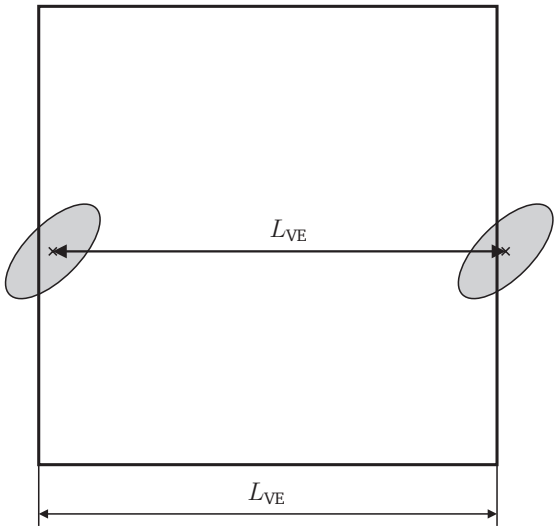

Figure 4.4: Periodic arrangement of inclusions penetrating the wall of the volume element. If a pore penetrates the wall of the volume element model, an equivalent inclusion with the same spatial orientation is placed on the opposing side of the volume element.

2. Definition of aspect ratio: After the individual pore volumes are defined, each pore is assigned an aspect ratio for the ellipsoids it consists of. The aspect ratios are generated according to the distribution of the ratio between bounding box volume to pore volume as described above. Thus a statistical variation of the spatial ramification of the pores is achieved.

3. Calculation of half-axis dimensions: Up to this step the individual pore volumes and the corresponding aspect ratios for the ellipsoids are defined. The remaining task is to calculate the half-axis dimensions conserving the half-axis ratio and leading to the desired pore volume. First, the maximum volume of a pore with a given half-axis ratio within the micromechanical model is calculated. For this purpose the pore is assumed to sprawl across the whole volume element with the major half-axis of the ellipsoids equal to L_{VE}. To calculate the volume, the Boolean pore model is divided into n slices. The cross sectional area of each slice is calculated and multiplied with the thickness of the slice. Adding up the volume of the individual slices results in the pore volume. Since the principle of scale separation as introduced in Equation (4.2) applies, the initial configuration with the pore sprawling across the whole volume element model yields a too larger pore volume. Thus the half-axis ratio has to be adjusted, which is achieved using a bisecting algorithm which readjusts the half-axes ratio of the model pore until the model pore volume V_{ha} is within a tolerance tol of the target pore volume V_{t}. This can be written as

$$|V_{\mathrm{ha}} - V_{\mathrm{t}}| < |tol| \, . \tag{4.4}$$

Within the first iteration the half-axis dimensions are divided by two and the pore volume is recalculated allowing three possible configurations:

(a) $|V_{\text{ha}} - V_{\text{t}}| < |tol|$: The desired pore volume is reached and no further adjustment is needed.

(b) $V_{\text{ha}} - V_{\text{t}} > +tol$: The pore volume is too large, thus the half-axis dimensions are decreased to the average of the last and second to last configuration.

(c) $V_{\text{ha}} - V_{\text{t}} < -tol$: The pore volume is too small, thus the half-axis dimensions are increased to the average of the last and second to last configuration.

This procedure is repeated until Equation (4.4) is fulfilled and the appropriate half-axis dimensions are determined.

4. Spatial pore distribution: By default a spatially random distribution of the pores within the micromechanical volume element is realized using the random number generation function of the programming language Python. A volume element model with a spatially random pore distribution is depicted in Figure 4.6 (a). The distribution algorithm is designed in such a way, that individual pores are non overlapping and spatially periodic (cf. Figure 4.4). A spatial clustering of pores can be provoked by defining normal distribution functions and thresholds, which influence the probability of a pore to be placed at a certain location. An example of a volume element model with clustered pores is presented in Figure 4.6 (b).

Based on the resulting parameters, the micromechanical geometry model is automatically generated using the programming language Python and the commercial finite element code Abaqus/CAE. In the following, the steps for the automated generation of the FE model are described in more detail.
First the individual parts of the microstructure, namely the cube with the dimensions of the desired volume element and the pores are generated in the Part-module of Abaqus/-CAE. The pores are generated individually. Thus an ellipsoid with the defined half-axis dimensions is generated. The ellipsoid is then imported three times into the Assembly-module of Abaqus/CAE arranging the major half-axis of the ellipsoids mutually perpendicular to a common center. To unite the ellipsoids to the Boolean pore model, the merge function of Abaqus/CAE is utilized. Once the cube and the individual pores are generated, the pores are spatially arranged within the cube in the Assembly-module of Abaqus/CAE. Again the merge functionality is used to subtract the pores from the cube. The operation results in a division of the cube into the matrix material representing the cast alloys' metal matrix structure presented in Figure 4.5 (a) and the enclosed pores presented in Figure 4.5 (b). Once the geometry model is constructed, the finite element

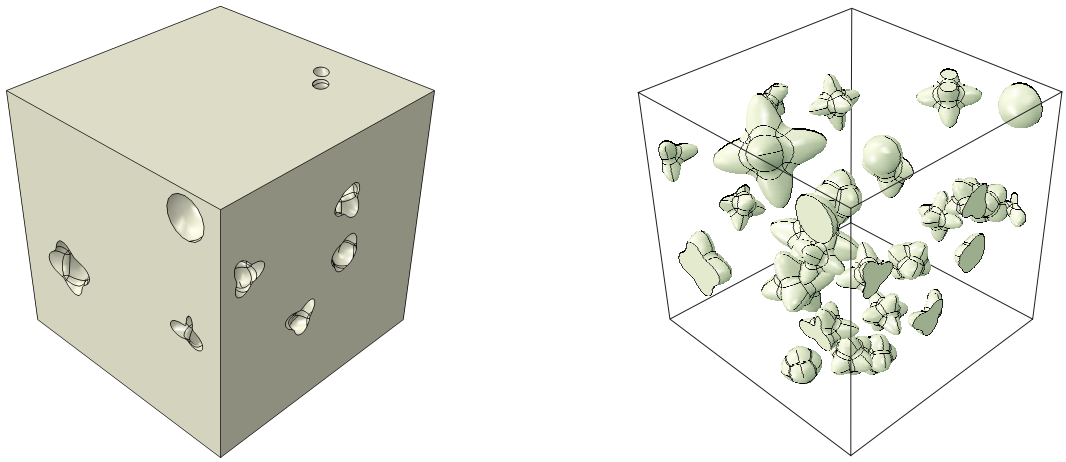

(a) (b)

Figure 4.5: Geometry of the volume element model exhibiting a pore volume fraction of 5%. The pores exhibit a spatially random distribution; (a) The surface of the volume element excluding the pores is depicted representing the cast alloys' microstructure; (b) The negative of the microstructure model is depicted representing the pores.

mesh has to be generated. The element size is defined by default as a fraction of the smallest ligament length[1] within the model. This ensures that slender morphological structures are resolved by a minimum number of finite elements over their cross section, which is vital to obtain reliable FE results. To mesh the microstructure model either the quadratic tetrahedral elements C3D10M or the linear tetrahedral elements C3D8 [68] can be utilized. The mesh is generated in the Mesh-module of Abaqus/CAE using the free mesh technique, which allows to mesh complex geometries. Figure 4.6 (a) shows a volume element model with a random pore distribution ($R \approx 1$), whereas Figure 4.6 (b) shows a volume element model exhibiting a clustered pore distribution ($R < 1$).

4.2.2 Micromechanical Problem Definition

4.2.2.1 Balance Equation

In this section the differential balance equation is formulated. According to [69], the equilibrium condition can be written as

$$\boldsymbol{\nabla}_{\mathrm{m}} \cdot \boldsymbol{\sigma}_{\mathrm{m}} = \mathbf{0} \qquad \text{in} \qquad \Omega_{\mathrm{m}} \tag{4.5}$$

with the subscript m denoting *micromechanical* quantities. Equation 4.5 is a simplified version of the equilibrium condition since the body forces are not considered within the presented finite element model. In Equation 4.5 Ω_{m} is the current domain of the

[1]The minimum ligament length denotes the shortest distance between two pores.

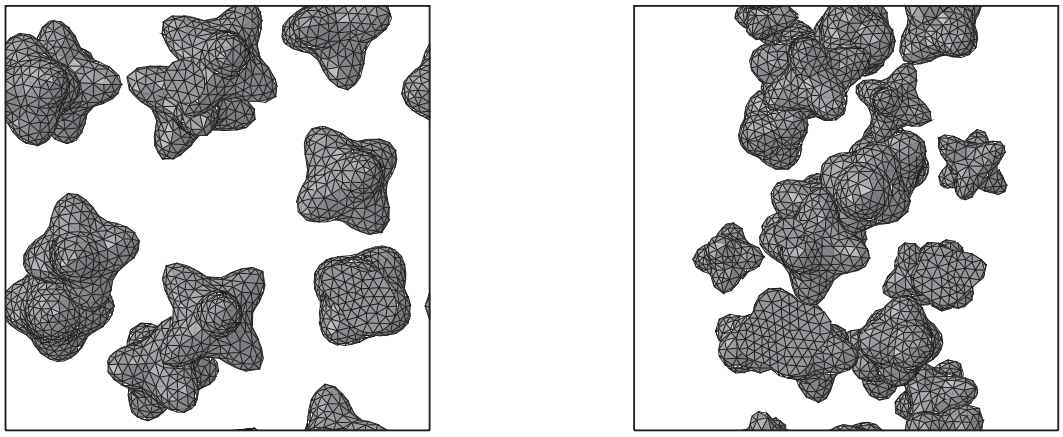

(a) (b)

Figure 4.6: Two distinct spatial distributions of the pores. (a) Uniformly random microvoid distribution ($R \approx 1.0$); (b) Clustered void distribution ($R \approx 0.5$).

volume element model and $\boldsymbol{\sigma}_{\mathrm{m}}$ is the micromechanical Cauchy stress tensor. There are three types of boundary conditions typically used for micromechanical models, namely periodicity, uniform displacement and uniform traction conditions [70]. All of these boundary conditions fulfill Hill's energy criterion [71]

$$\langle \boldsymbol{\sigma} \rangle \cdot \langle \boldsymbol{\varepsilon} \rangle = \langle \boldsymbol{\sigma} \boldsymbol{\varepsilon} \rangle \,. \tag{4.6}$$

Within this work the periodic as well as the uniform displacement boundary conditions are implemented and described in more detail in the following.

4.2.2.2 Periodic Boundary Condition

Periodic boundary conditions constitute Dirichlet type boundary conditions, which establish an infinite periodic arrangement of the volume element model omitting any free surface effects. The periodic arrangement of the volume element model in the reference configuration may be imagined as an infinite spatial lattice, which can be expressed by

$$\mathbb{L}^3 = \{ \mathbf{x} \in \mathbb{R}^3 \mid \mathbf{x} = \sum_{i=1}^{3} \lambda_i \, \mathbf{e}_i, \ \lambda_i \in \mathbb{Z} \} \,, \tag{4.7}$$

with $\mathbf{e}_i$ as the base vectors of the volume element model. To abide a complete tiling of space during loading, opposing surfaces of the volume element have to deform congruently. Therefore the surface of the volume element model is divided into an *active* $\partial\Omega_{\mathrm{m}}^{+}$ and a *passive* $\partial\Omega_{\mathrm{m}}^{-}$ region. The kinematics of the *passive* and *active* region are then coupled by equations.

To split the surface of the volume element model denoted as ve into an *active* and a *passive* domain, the set of vectors

$$\mathbf{A}_{\mathrm{ve}} = (\mathbf{e}_{\mathrm{x}}, \mathbf{e}_{\mathrm{y}}, \mathbf{e}_{\mathrm{z}}) \tag{4.8}$$

containing the base vectors of the volume element model and the set of vectors

$$\mathbf{B} = \{\mathbf{b} \in \mathbb{R}^3 \mid \mathbf{b} = (b_1, b_2, b_3)^{\mathrm{T}} \ \wedge \ b_1, b_2, b_3 \in \{-1, 0, 1\}\} \tag{4.9}$$

containing the linear combinations of the base vectors with the linear combination factors $b_i \in \{-1, 0, 1\}$ are introduced. Initially the whole surface of the volume element is assumed to be *active*. Starting at an arbitrary point $\mathbf{x}^+ \in \partial\Omega_{\mathrm{m}}^+$ of the *active* domain, the set of vectors

$$\mathbf{N} = \{\mathbf{x}_{\mathrm{cp}} \in \mathbb{R}^3 \mid \mathbf{x}_{\mathrm{cp}} = \mathbf{x}^+ + \mathbf{A}_{\mathrm{ve}}\mathbf{b}, \ \mathbf{b} \neq \mathbf{0}\} \tag{4.10}$$

is generated, where $\mathbf{x}_{\mathrm{cp}}$ are possible corresponding points to $\mathbf{x}^+ \in \partial\Omega_{\mathrm{m}}^+$. However, the actual corresponding points to $\mathbf{x}^+ \in \partial\Omega_{\mathrm{m}}^+$ are found as a subset

$$\mathbf{x}^- = \{\mathbf{x}_{\mathrm{cp}} \mid \mathbf{x}_{\mathrm{cp}} \in \partial\Omega_{\mathrm{m}}, \ \mathbf{x}_{\mathrm{cp}} \in \mathbf{N}\} \tag{4.11}$$

of $\mathbf{N}$. The corresponding points are shifted from the *active* to the *passive* set, thus diminishing the *active* set. This routine is repeated until every point of the *active* set ($\mathbf{x}^+$) has at least one corresponding point in the *passive* set ($\mathbf{x}^-$).
This routine does not lead to a unique division of the surface of the volume element model into *active* and *passive* regions. Theoretically an infinite number of possible configurations is possible. However, to enable an automated implementation of the periodic boundary conditions a standardized division of the volume element model surface is defined which complies with the theory introduced above and presented in Figure 4.7. For corresponding points in the *active* and *passive* sets, the periodic boundary conditions can be written as

$$\mathbf{x}^+ - \mathbf{x}^- \ = \ \langle \mathbf{F} \rangle \, (\mathbf{X}^+ - \mathbf{X}^-) \tag{4.12}$$

where $\mathbf{x}^+$ and $\mathbf{x}^-$ denote corresponding surface points of the micromechanical volume element model in the current configuration, $\mathbf{X}^+$ and $\mathbf{X}^-$ denote the reference configuration of these points, and $\langle \mathbf{F} \rangle$ is the homogenized deformation gradient imposed upon the micromechanical volume element (cf. Section 4.2.3).
To implement the periodicity condition given in Equation (4.12) into Abaqus, the homog-

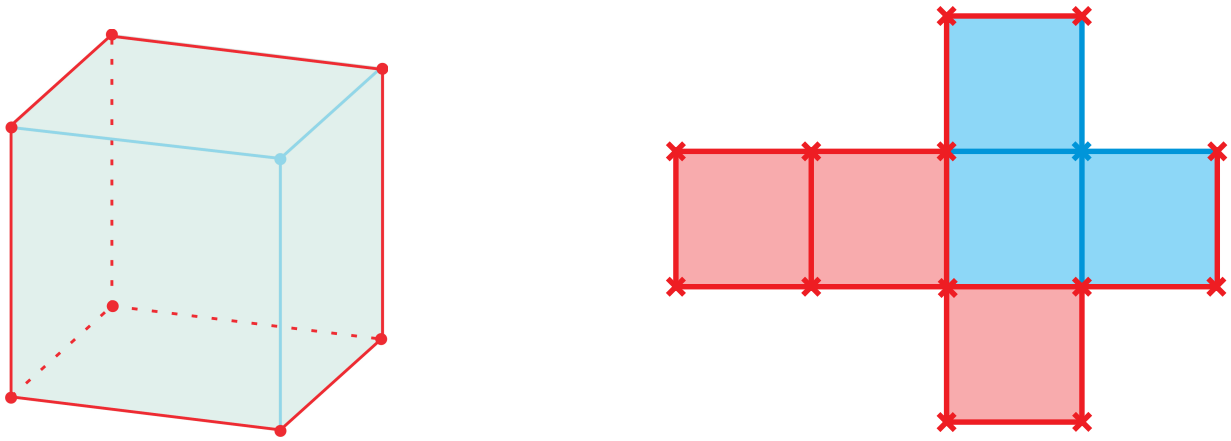

(a) (b)

Figure 4.7: Representation of the *active* and *passive* domains of the volume element model: (a) Three dimensional representation of the volume element model. Red edges are *passive* regions whereas blue edges are *active* regions. (b) Girthed surface of the volume element model with color coded *active* (blue) and *passive* (red) domains.

enized deformation gradient is decomposed into an identity tensor $\mathbf{I}$ and the homogenized displacement gradient tensor $\boldsymbol{\nabla}\langle\mathbf{u}\rangle$

$$\langle\mathbf{F}\rangle \;=\; \mathbf{I} + \boldsymbol{\nabla}\langle\mathbf{u}\rangle \;. \tag{4.13}$$

Within the FE model the displacement gradient tensor is represented by the displacement of three so called dummy nodes

$$\boldsymbol{\nabla}\langle\mathbf{u}\rangle \;=\; (\mathbf{u}^{\mathrm{D_x}}, \mathbf{u}^{\mathrm{D_y}}, \mathbf{u}^{\mathrm{D_z}}) \;. \tag{4.14}$$

The dummy nodes $\mathrm{D_x}, \mathrm{D_y}$ and $\mathrm{D_z}$ are introduced to govern the deformation of the volume element model. Theoretically they can be positioned at arbitrary coordinates, since only their displacement governs the deformation of the volume element model. However, to avoid problems with a visual evaluation of the finite element results (e.g. evaluating stresses predicted by the finite element model in a viewer) it is convenient to ensure that the dummy nodes are placed somewhere within the volume element model, otherwise an automatic fit of the volume element model within the viewer might fail. Hence, within this work the dummy nodes are placed at the origin of the global coordinate system which coincides with the center of the volume element models. The spatial arrangement of the dummy nodes in Figure 4.8 and Figure 4.9 does not represent the actual location of the dummy nodes, but is chosen for a better comprehension.
An implementation where the displacements of the dummy nodes govern the deforma-

tion of the volume element model necessitates to recast the periodicity Equation (4.12) into a displacement based formulation, which is written as

$$\boldsymbol{\nabla}\langle \mathbf{u} \rangle \, \mathbf{b} \; = \; \mathbf{u}^{\mathbf{x}^+} - \mathbf{u}^{\mathbf{x}^-} \qquad \text{with} \qquad \mathbf{A}\mathbf{b} = \mathbf{x}^+ - \mathbf{x}^- \; . \tag{4.15}$$

In order to implement the theory described above, the discrete nodes of the FE model have to be divided into active and passive domains. This is done according to Figure 4.7, even though the nodes on opposing surfaces of the model are not congruent.

However, for the vertex and edge nodes of the micromechanical FE model Equation (4.15) can be immediately implemented since the discrete nodes in the *active* domain have congruent nodes in the *passive* domain. The equations coupling the displacement of the vertices with those of the dummy nodes are written as

$$\begin{aligned}
\mathbf{u}^{b} - \mathbf{u}^{a} + \mathbf{u}^{D_x} + \mathbf{u}^{D_y} + \mathbf{u}^{D_z} &= \mathbf{0} \\
\mathbf{u}^{d} - \mathbf{u}^{a} + \mathbf{u}^{D_x} + \mathbf{u}^{D_y} &= \mathbf{0} \\
\mathbf{u}^{c} - \mathbf{u}^{a} + \mathbf{u}^{D_x} + \mathbf{u}^{D_z} &= \mathbf{0} \\
\mathbf{u}^{e} - \mathbf{u}^{a} + \mathbf{u}^{D_x} &= \mathbf{0} \\
\mathbf{u}^{f} - \mathbf{u}^{a} + \mathbf{u}^{D_y} + \mathbf{u}^{D_z} &= \mathbf{0} \\
\mathbf{u}^{h} - \mathbf{u}^{a} + \mathbf{u}^{D_y} &= \mathbf{0} \\
\mathbf{u}^{g} - \mathbf{u}^{a} + \mathbf{u}^{D_z} &= \mathbf{0} \; ,
\end{aligned} \tag{4.16}$$

following the nomenclature of vertices and dummy nodes as depicted in Figure 4.8 (a). The equations, which couple the displacement of corresponding edge nodes with the dummy node displacements are implemented as

$$\begin{aligned}
\mathbf{u}^{k} - \mathbf{u}^{i} + \mathbf{u}^{D_x} + \mathbf{u}^{D_y} &= \mathbf{0} \\
\mathbf{u}^{j} - \mathbf{u}^{i} + \mathbf{u}^{D_x} &= \mathbf{0} \\
\mathbf{u}^{l} - \mathbf{u}^{i} + \mathbf{u}^{D_y} &= \mathbf{0} \\
\mathbf{u}^{o} - \mathbf{u}^{m} + \mathbf{u}^{D_y} + \mathbf{u}^{D_z} &= \mathbf{0} \\
\mathbf{u}^{p} - \mathbf{u}^{m} + \mathbf{u}^{D_y} &= \mathbf{0} \\
\mathbf{u}^{n} - \mathbf{u}^{m} + \mathbf{u}^{D_z} &= \mathbf{0} \\
\mathbf{u}^{s} - \mathbf{u}^{p} + \mathbf{u}^{D_x} + \mathbf{u}^{D_z} &= \mathbf{0} \\
\mathbf{u}^{t} - \mathbf{u}^{p} + \mathbf{u}^{D_x} &= \mathbf{0} \\
\mathbf{u}^{r} - \mathbf{u}^{p} + \mathbf{u}^{D_z} &= \mathbf{0} \; ,
\end{aligned} \tag{4.17}$$

using the nomenclature conventions of the edges and dummy nodes presented in Figure 4.8 (b). In contrast to the vertex and edge nodes, the nodes on opposing faces of

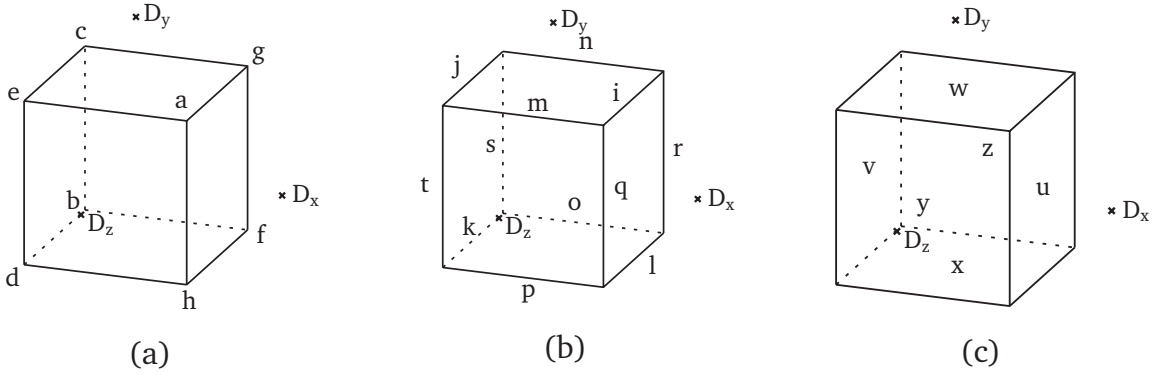

Figure 4.8: Representation of the volume element; (a) vertexes (a-h) and dummy nodes $\mathrm{D_x}$, $\mathrm{D_y}$, $\mathrm{D_z}$; (b) edge nodes excluding vertexes (i-t) and dummy nodes $\mathrm{D_x}$, $\mathrm{D_y}$, $\mathrm{D_z}$; (c) nodes on the faces excluding edge and vertex nodes of the volume element model (u-z) and dummy nodes $\mathrm{D_x}$, $\mathrm{D_y}$, $\mathrm{D_z}$.

the volume element are not necessarily congruent, which is due to the *free mesh* technique used to mesh the volume element model. Thus Equation (4.15) cannot be directly implemented for nodes on the volume element faces. To bypass this shortcoming, the *tie* function of Abaqus/CAE is used. Nodes of *passive* faces are copied and the copy of the *passive* face $(\ )^{\mathrm{pc}}$ is *tied* to the opposing *active* face. The *tie* condition is established between the following faces

$$\mathrm{v^{pc}} \text{ tied to } \mathrm{u}$$
$$\mathrm{x^{pc}} \text{ tied to } \mathrm{w}$$
$$\mathrm{z^{pc}} \text{ tied to } \mathrm{y}$$

and ensures a congruent deformation and displacement of tied faces. Naturally the *passive* face and the copy of the *passive* face exhibit congruent nodes. The relative displacement of the *active* and the *passive* faces as given in Equation (4.14) are governed by node based equations coupling the displacement of the nodes of the copied *passive* face, the original *passive* face and the dummy nodes. The equations can be written as

$$\begin{aligned}
\mathbf{u}^{\mathrm{v}} - \mathbf{u}^{\mathrm{v^{pc}}} + \mathbf{u}^{\mathrm{D_x}} &= \mathbf{0} \\
\mathbf{u}^{\mathrm{x}} - \mathbf{u}^{\mathrm{x^{pc}}} + \mathbf{u}^{\mathrm{D_y}} &= \mathbf{0} \\
\mathbf{u}^{\mathrm{z}} - \mathbf{u}^{\mathrm{z^{pc}}} + \mathbf{u}^{\mathrm{D_z}} &= \mathbf{0}\ .
\end{aligned} \tag{4.18}$$

A schematic representation of the coupling of *active* and *passive* faces for the 2D case is presented in Figure 4.9.

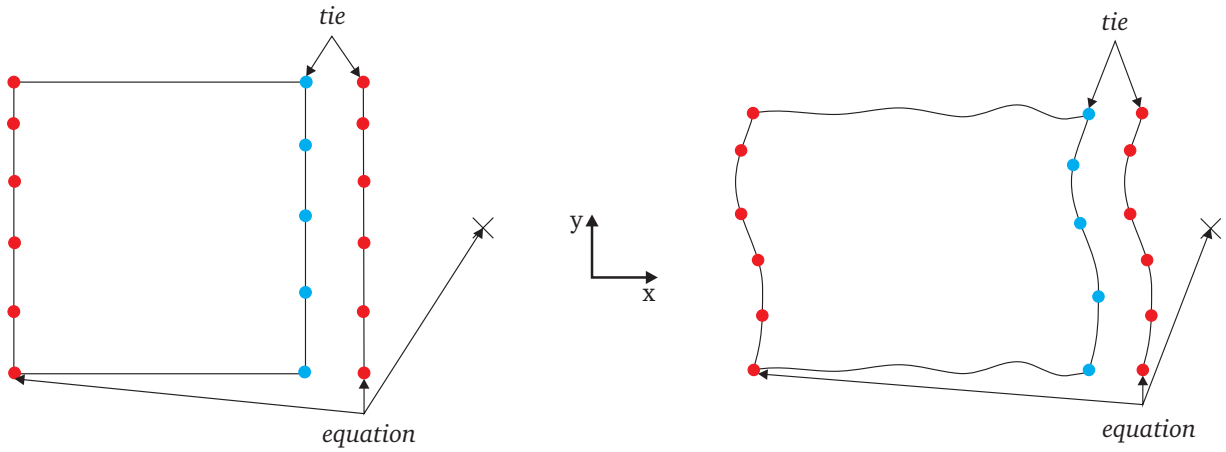

(a) (b)

Figure 4.9: Schematic representation of the periodic boundary conditions on a two dimensional model. The *active* (blue) and *passive* (red) faces of the model have non corresponding nodes. To ensure a congruent deformation of *active* and *passive* surfaces a copy of the *passive* face (shown next to the *active* face) is tied to the *active* face. Naturally the copied and the original *passive* face have corresponding nodes. The relative displacement between those two phases is ensured by an equation coupling the dummy node, the nodes of the copy of the *passive* face and the nodes of the original *passive* face. (a) Two dimensional model in reference configuration; (b) Two dimensional configuration in current configuration (deformed state).

4.2.2.3 Uniform Displacement Boundary Conditions

Complementary to the periodicity conditions, uniform displacement (UD) boundary conditions are implemented to compare the results obtained by periodic boundary conditions. Furthermore the sensitivity of the micromechanical model towards different Dirichlet type boundary conditions is investigated by comparing results from volume element models with prescribed UD and periodicity conditions.

In a general form the UD boundary conditions can be written as

$$\mathbf{x} = \langle \mathbf{F} \rangle \, \mathbf{X} \, , \tag{4.19}$$

where $\mathbf{x} \in \partial\Omega_{\mathrm{m}}$ denotes the current configuration and $\mathbf{X} \in \partial\Omega_{\mathrm{m0}}$ denotes the reference configuration of a point at the surface of the micromechanical volume element model. Within this work the implementation of UD conditions is limited to uni and multi-axial loading, whereas shear deformations are not covered.

To implement the UD conditions the surface of the volume element model is split into six sets, containing the FE nodes of the volume element's faces. Each set includes the FE nodes on the face as well as the adjacent edge and vertex nodes. The nomenclature of the sets corresponds to Figure 4.8 (c). As for the periodicity conditions, the displacement of

the dummy nodes are utilized to govern the deformation of the volume element model. The displacement of the dummy nodes are coupled with the face sets u, w and y by

$$\begin{aligned}(\mathbf{u}^{\mathrm{D_x}} \cdot \mathbf{e}_x)\mathbf{e}_x - (\mathbf{u}^{\mathrm{u}} \cdot \mathbf{e}_x)\mathbf{e}_x = \mathbf{0}\,,\\ (\mathbf{u}^{\mathrm{D_y}} \cdot \mathbf{e}_y)\mathbf{e}_y - (\mathbf{u}^{\mathrm{w}} \cdot \mathbf{e}_y)\mathbf{e}_y = \mathbf{0}\,,\\ (\mathbf{u}^{\mathrm{D_z}} \cdot \mathbf{e}_z)\mathbf{e}_z - (\mathbf{u}^{\mathrm{y}} \cdot \mathbf{e}_z)\mathbf{e}_z = \mathbf{0}\,.\end{aligned} \tag{4.20}$$

The displacement of the remaining faces is locked in the respective direction, which is written as

$$\begin{aligned}\mathbf{u}^{\mathrm{v}}\mathbf{e}_x = 0\,,\\ \mathbf{u}^{\mathrm{x}}\mathbf{e}_y = 0\,,\\ \mathbf{u}^{\mathrm{z}}\mathbf{e}_z = 0\,.\end{aligned} \tag{4.21}$$

4.2.2.4 Constitutive behavior of MAR-M247

As mentioned in Chapter 4.1 the von Mises plasticity theory is used to describe the constitutive behavior of the metal matrix phase. Thus, the grain structure of the material is homogenized by a continuum approach as depicted in Figure 4.10. The material behavior is based on a Ramberg-Osgood type constitutive law [72] describing experimentally determined stress-strain curves of the bulk material. The Ramberg-Osgood constitutive law describes a non-linear elastic material behavior. To allow for a plastic deformation

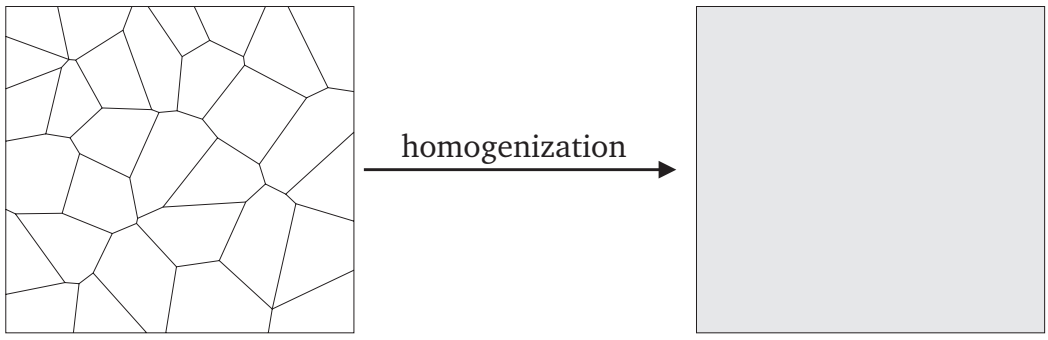

Figure 4.10: Homogenization of the heterogeneous bulk material. (a) microstructural grain structure; (b) homogenized bulk material – the grains are smeared resulting in a continuum.

of the material, the material behavior is implemented in Abaqus as an elastic-plastic constitutive law representing the stress strain curve predicted by the Ramberg-Osgood approximation. For the elastic regime a Young's modulus of 200000 $\frac{\mathrm{N}}{\mathrm{mm}^2}$ is assigned. The

initial yield stress σ_{y0} is defined as 800 $\frac{\mathrm{N}}{\mathrm{mm}^2}$. The plastic regime is defined according to the flow stress depicted in Figure 4.11.

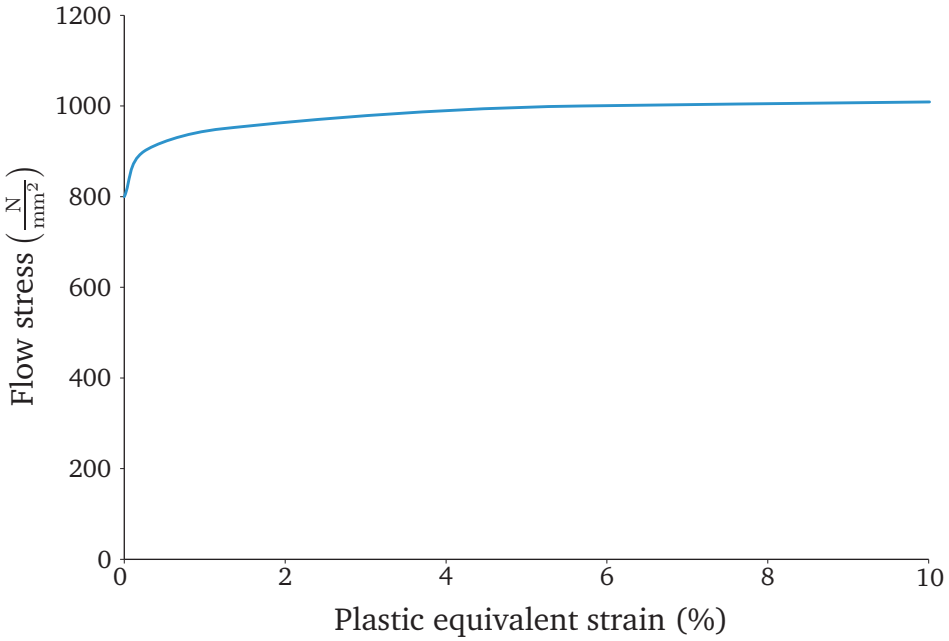

Figure 4.11: Flow curve for the bulk material MAR-M247 as prescribed for the Abaqus simulations.

4.2.3 Computational Homogenization

In this section the evaluation of apparent material properties based on homogenized stress and strain quantities from the micromechanical FE model are described. The homogenization of any quantity $A(\mathbf{x})$ over a continuous region Ω, for example the homogenization of the von Mises stress distribution within the volume element model as presented in Figure 4.12 is expressed by

$$\langle A \rangle \;=\; \frac{1}{V_{\Omega_\mathrm{m}}} \int_{\Omega_\mathrm{m}} A(\mathbf{x})\, \mathrm{d}\Omega \;. \tag{4.22}$$

where V_{Ω_m} is the volume of the continuous region and $\langle A \rangle$ is the homogenized quantity. Since the homogenized deformation gradient tensor $\langle \mathbf{F} \rangle$ is known a priori, and is imposed upon the FE model using Dirichlet type boundary conditions as explained above, the remaining task in order to calculate apparent material properties is to homogenize the stress distribution within the volume element model. The volume averaged Cauchy stress tensor $\langle \boldsymbol{\sigma} \rangle$ is obtained via the transformation

$$\langle \boldsymbol{\sigma} \rangle \;=\; \frac{1}{\det\langle \mathbf{F} \rangle} \langle \mathbf{P} \rangle \, \langle \mathbf{F} \rangle^{\mathrm{T}} \tag{4.23}$$

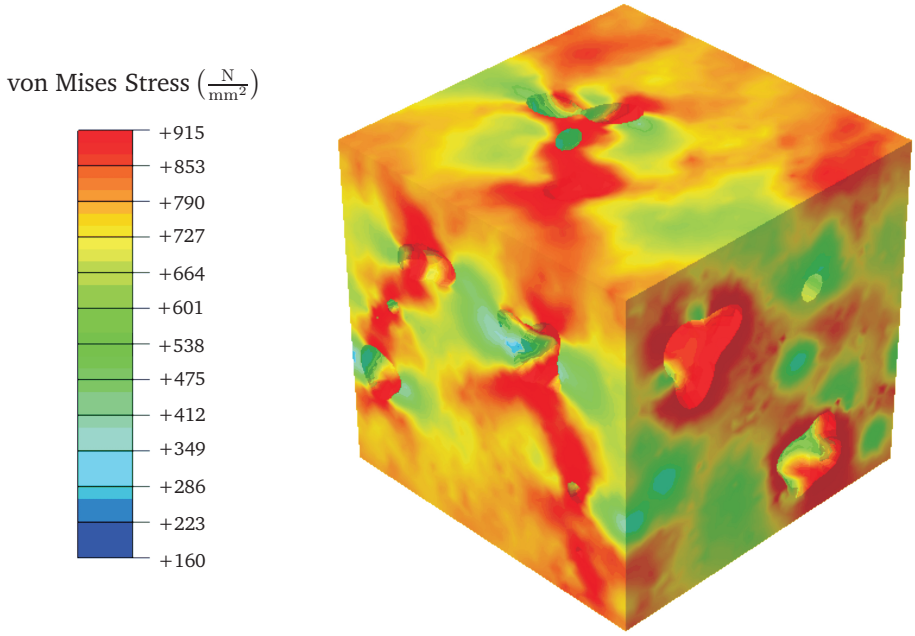

Figure 4.12: Von Mises stress distribution in the bulk material (metal matrix). The volume element model exhibits a pore volume fraction of 10 %. The highest stresses occur in the vicinity of the pores.

of the homogenized first Piola Kirchhoff stress tensor $\langle \mathbf{P} \rangle$ (cf. [73]). According to Equation (4.22) the homogenized first Piola Kirchhoff stress tensor $\langle \mathbf{P} \rangle$ can be written as

$$\langle \mathbf{P} \rangle \;=\; \frac{1}{V_{\mathrm{m0}}} \int_{V_{\mathrm{m0}}} \mathbf{P} \, \mathrm{d}\Omega \; . \tag{4.24}$$

By considering the equilibrium condition $\boldsymbol{\nabla}_{\mathrm{m0}} \cdot \mathbf{P}^{\mathrm{T}} = \mathbf{0}$ and the equality $\boldsymbol{\nabla}_{\mathrm{m0}} \mathbf{X} = \mathbf{I}$, the averaged first Piola Kirchhoff stress tensor $\langle \mathbf{P} \rangle$ can be recast in

$$\mathbf{P} = (\boldsymbol{\nabla}_{\mathrm{m0}} \cdot \mathbf{P}^{\mathrm{T}}) \mathbf{X} + \mathbf{P} \cdot (\boldsymbol{\nabla}_{\mathrm{m0}} \mathbf{X}) \;=\; \boldsymbol{\nabla}_{\mathrm{m0}} \cdot (\mathbf{P}^{\mathrm{T}} \mathbf{X}) \; . \tag{4.25}$$

Substituting this expression into Equation (4.24) allows the application of the divergence theorem as presented by Koutznetsova [7]. With this the homogenized first Piola Kirchhoff stress can be written as

$$\langle \mathbf{P} \rangle \;=\; \frac{1}{V_0} \int_{\Omega \mathrm{m0}} \boldsymbol{\nabla}_{\mathrm{m0}} \cdot (\mathbf{P}^{\mathrm{T}} \mathbf{X}) \, \mathrm{d}\Omega \;=\; \frac{1}{V_{\mathrm{m0}}} \int_{\partial \Omega_{\mathrm{m0}}} \mathbf{p} \otimes \mathbf{X} \, \mathrm{d}\partial\Omega \; , \tag{4.26}$$

where $\mathbf{p} = \mathbf{P} \cdot \mathbf{n}$ denotes the first Piola Kirchhoff stress vector and $\mathbf{n}$ denotes the outward normal vector with respect to the volume element boundary in reference state $(\partial \Omega_{\mathrm{m0}})$. The surface integral in Equation (4.26) is obtained from the volume element model after

solving the boundary value problem by a summation over the traction vectors of the FE nodes at the volume element boundary. This can be written as

$$\langle \mathbf{P} \rangle \;=\; \frac{1}{V_{\mathrm{m0}}} \sum_{i=i}^{N_{\mathrm{p}}} \mathbf{f}_i \otimes \mathbf{X}_i \,. \tag{4.27}$$

In Equation (4.27) $\mathbf{f}_i$ are the external forces at the boundary nodes and $\mathbf{X}_i$ are the corresponding location vectors in the reference configuration. Since the deformation of the volume element model is governed by dummy nodes, Equation (4.27) can be simplified further to

$$\langle \mathbf{P} \rangle \;=\; \frac{1}{V_{\mathrm{m0}}} \left(\mathbf{f}_{\mathrm{D_x}}, \mathbf{f}_{\mathrm{D_y}}, \mathbf{f}_{\mathrm{D_z}}\right);, \tag{4.28}$$

where $\mathbf{f}_{\mathrm{D_x}}$, $\mathbf{f}_{\mathrm{D_y}}$ and $\mathbf{f}_{\mathrm{D_z}}$ denote the reaction forces at the dummy nodes $\mathrm{D_x}, \mathrm{D_y}$ and $\mathrm{D_z}$. The homogenized Cauchy stress tensor is obtained by applying the transformations given in Equation (4.23).

Knowing the homogenized stress and strain quantities, the homogenized material properties are evaluated using Hooke's law

$$\langle \boldsymbol{\varepsilon} \rangle \;=\; \langle \mathbf{S} \rangle \, \langle \boldsymbol{\sigma} \rangle \tag{4.29}$$

where $\langle \boldsymbol{\varepsilon} \rangle$ is the homogenized strain of the volume element model, $\langle \mathbf{S} \rangle$ is the homogenized compliance tensor and $\langle \boldsymbol{\sigma} \rangle$ denotes the homogenized Cauchy stress tensor of the volume element model (cf. [71, 70]). Assuming an isotropic material behavior Equation (4.29) can be recast using the Voigt notation into

$$\begin{bmatrix} \langle \varepsilon_{11} \rangle \\ \langle \varepsilon_{22} \rangle \\ \langle \varepsilon_{33} \rangle \\ \langle \varepsilon_{23} \rangle \\ \langle \varepsilon_{13} \rangle \\ \langle \varepsilon_{12} \rangle \end{bmatrix} = \begin{bmatrix} S_{11} & S_{12} & S_{12} & 0 & 0 & 0 \\ S_{12} & S_{11} & S_{12} & 0 & 0 & 0 \\ S_{12} & S_{12} & S_{11} & 0 & 0 & 0 \\ 0 & 0 & 0 & S_{44} & 0 & 0 \\ 0 & 0 & 0 & 0 & S_{44} & 0 \\ 0 & 0 & 0 & 0 & 0 & S_{44} \end{bmatrix} \begin{bmatrix} \langle \sigma_{11} \rangle \\ \langle \sigma_{22} \rangle \\ \langle \sigma_{33} \rangle \\ \langle \sigma_{23} \rangle \\ \langle \sigma_{13} \rangle \\ \langle \sigma_{12} \rangle \end{bmatrix} . \tag{4.30}$$

In Equation (4.30) $S_{11} = \frac{1}{E}$, $S_{12} = -\nu$ and $S_{44} = \frac{(1+\nu)}{E} = \frac{1}{2G}$. Applying an uniaxial load to the micromechanical volume element model in $\mathbf{x}$ direction leads to strains in $\mathbf{x}, \mathbf{y}$ and $\mathbf{z}$ direction ($\langle \varepsilon_{11} \rangle$, $\langle \varepsilon_{22} \rangle$ and $\langle \varepsilon_{33} \rangle$) as well as to a stress in $\mathbf{x}$ direction ($\langle \sigma_{11} \rangle$). All other stress entities are equal to zero. The homogenized elastic modulus can be evaluated

using the homogenized stress and strain fields from the micromechanical model and solving Equation (4.30) and is expressed by

$$\langle E \rangle = \frac{\langle \sigma_{11} \rangle}{\langle \varepsilon_{11} \rangle} \,. \tag{4.31}$$

To assure the validity of the resulting Young's modulus the plastic dissipation (PD) energy within the micromechanical volume element has to be zero at the stress level used to evaluate the Young's modulus as presented in Figure 4.13. The PD energy is recorded at every increment by Abaqus. Likewise the apparent shear modulus can be obtained by

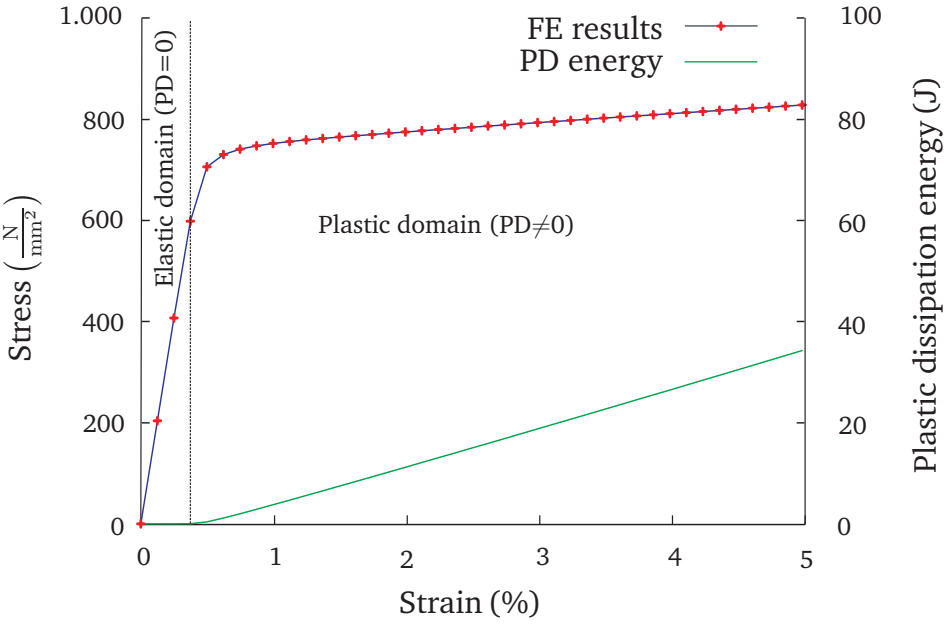

Figure 4.13: Evaluation of the Young's modulus. The Young's modulus can be evaluated as long as the plastic dissipation (PD) energy in the model remains zero.

solving Equation (4.30), which is shown for a volume element model exposed to a pure shear deformation ($\varepsilon_{12} = \varepsilon_{21}$).

$$\langle G \rangle = \frac{\langle \sigma_{12} \rangle}{\langle \varepsilon_{12} \rangle} \tag{4.32}$$

The presented evaluation scheme allows for a treatment of isotropic as well as orthotropic materials. In case of orthotropy the elastic moduli as well as the shear moduli have to be evaluated separately for the **x**, **y**, **z** and **xy**, **xz** and **yz** directions, respectively (cf. [74]). In case of an anisotropic material an evaluation of an elasticity or a shear modulus is not possible. Instead the entities of the compliance or the stiffness tensor can be evaluated by a perturbation approach as described by Temizer [27] which is addressed in more detail in Chapter 4.3.

4.2.4 Evaluation of Local Variables

Contrary to the homogenized material behavior, the prediction of the onset of fracture largely relies on local stresses and strains which are magnified in the vicinity of flaws as e.g. pores [75]. Griffith [76] established a quantitative connection between the size of a flaw and the fracture stress. The theory that flaws, in our case pores have a profound influence on the fracturing of sample is supported by Figure 4.14 depicting a CT scan of a porous tensile test sample before and after the test. The orange structures represent pores which were identified based on the CT scan before the tensile test. The fracture surface is the light blue jagged area. Evidently the fracture evolved along the flawed (porous) region of the sample. To predict the onset of fracture in the vicinity of pores,

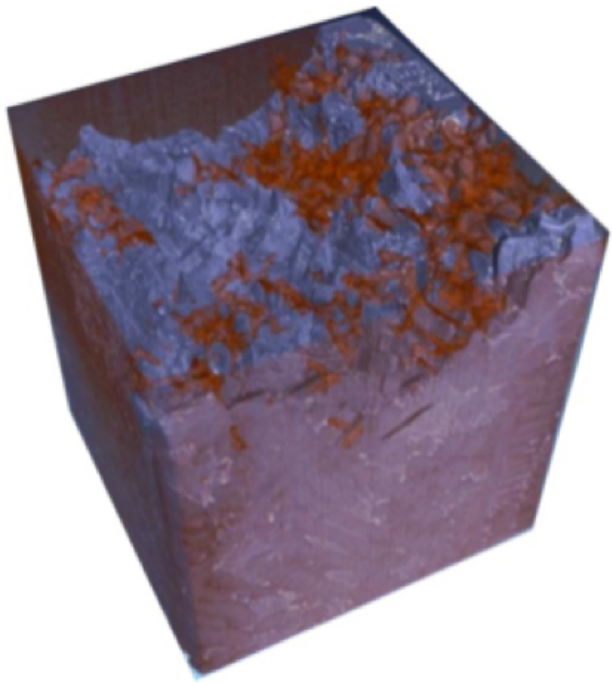

Figure 4.14: Overlay plot of a CT scan of a porous sample before and after a tensile test. The orange areas denote pores within the sample which were identified by CT before the tensile test. The fracture surface is represented by the lighter blue structured area. The fracture evolved along the identified porous regions.

a post processing routine to analyze the local distribution of stresses and strain quantities within the micromechanical model is implemented using the programming language Python. At each integration point the stress and strain quantity and the corresponding integration point volume (IVOL) is read out from the output database file of the micromechanical volume element model. With the obtained data a histogram is generated sorting the stress or strain quantities into bins. The bin height correlates with the cumulative IVOL within a bin divided by the total integration point volume of the whole

volume element model[2]. An example of such a diagram is presented in Figure 4.15. The results obtained from the cumulative distribution function enable a quantile evaluation of the evaluated quantity.

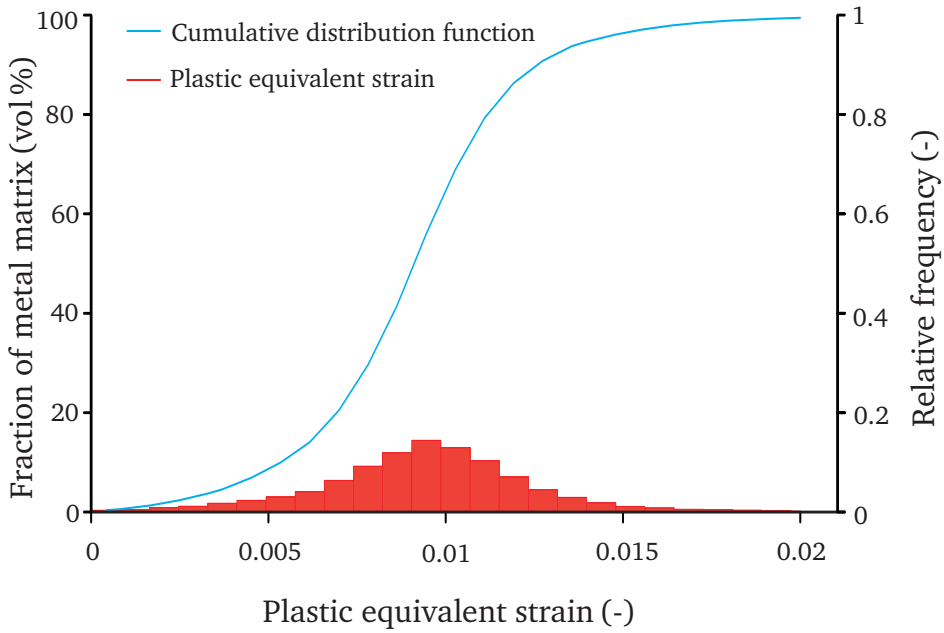

Figure 4.15: The histogram (red) shows the relative frequency of the matrix exhibiting a certain plastic equivalent strain. The blue curve represents the cumulative distribution function of the plastic equivalent strain. The mean plastic equivalent strain is just below 1 % whereas the maximum values of plastic equivalent strain are 2 % and more. The maximum plastic equivalent strain values appear in the vicinity of the pores, where cracks are initiated.

[2]The implementation is based on work from A. Fillafer

4.3 Multiscale Finite Element Modeling

The increasing environmental awareness of the customers as well as a scarcity of raw materials necessitates to save resources and minimize the mass of components. Thus, providing an optimized component design is ever more important for companies to stay competitive. Established optimization tools are mostly based on continuum approaches, which do not consider the microstructure of the materials. However, the microstructure of engineering materials has a substantial influence on the mechanical behavior as shown in the preceding chapters. Furthermore, components such as e.g. cast parts exhibit variations in the microstructure depending on the location within the part. The consideration of these microstructural fluctuations bears the potential to improve the component layout.
So-called multiscale approaches present a promising possibility to exploit this potential. As the name *multiscale* suggests, two (or more) models covering different length scales of the same component are run and certain quantities are exchanged between these models. In the following two different concepts are introduced, namely a concurrent multiscale model and a sequentially coupled multiscale model.

4.3.1 Sequential Multiscale Model

A pragmatic way to link the results gained on the microscopic scale to the macroscopic level is a sequential coupling of these scales. The steps of this sequential multiscale approach are depicted in Figure 4.16. The first step is to divide the macroscopic component into sections, where each section represents a different microstructure (cf. Figure 4.16, the grey region of the casting represents pore free material, whereas the green area represents porous material). In the second step all regions are assigned a constitutive behavior. Pore free regions are assigned the constitutive behavior of the bulk material, whereas the constitutive behavior of a porous region is obtained by the homogenized response of a micromechanical volume element model representing the microstructure of that particular domain. Thus, it is possible to consider the influence of microstructural variations on the constitutive behavior.

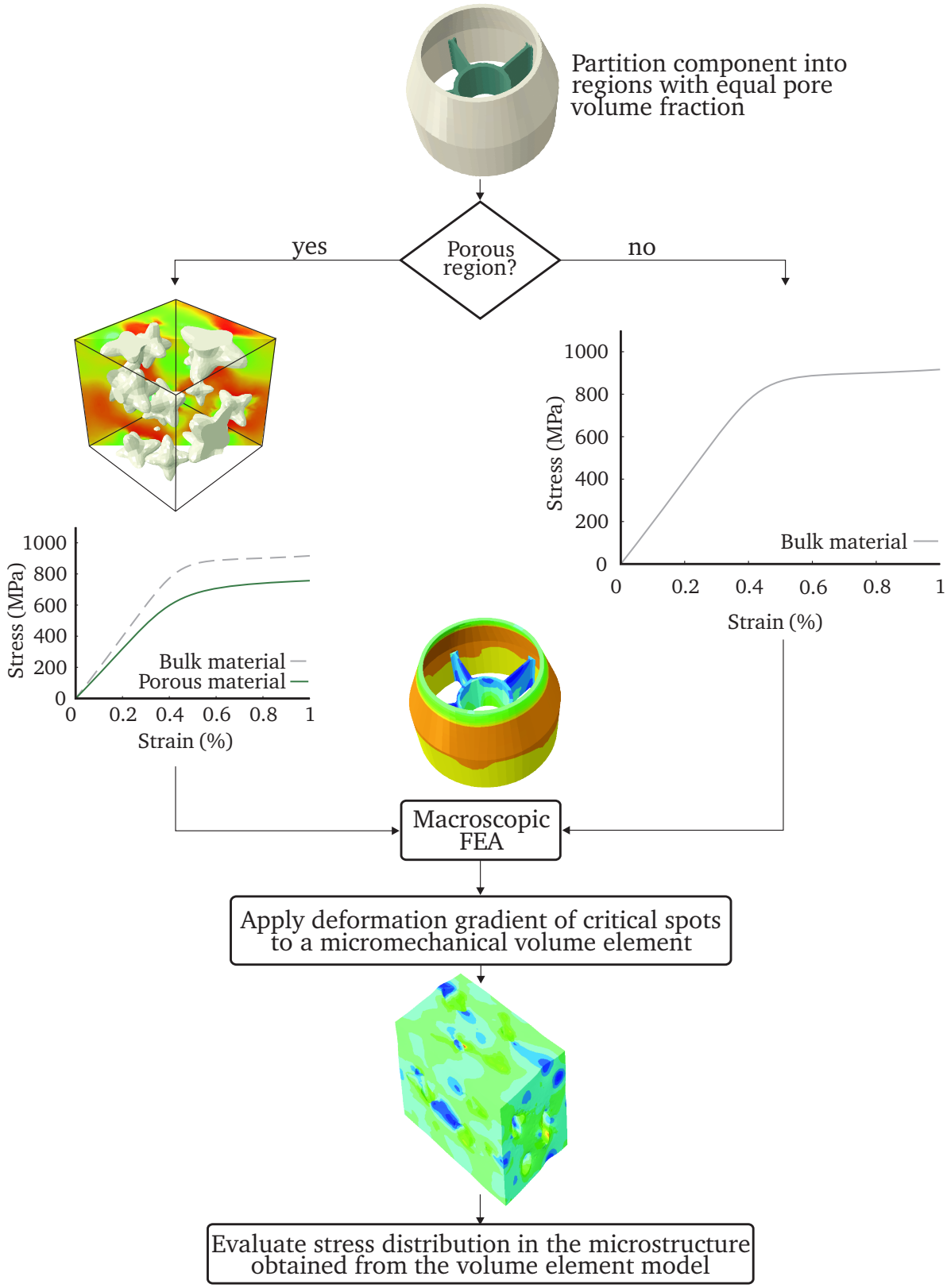

Figure 4.16: Sequential multiscale computation steps. First the component is divided into sections with different microstructures. Depending on the microstructure of the section, either the constitutive behavior of the bulk material, or a constitutive behavior obtained from the homogenized response of a volume element model is assigned for the macroscopic finite element analysis (FEA). The stresses within the microstructure can be evaluated based on a subsequent micromechanical model of critical points.

In the third step the boundary conditions and loads are applied to the component and the macroscopic FEA is performed yielding the stress and strain distributions. To evaluate the stress and strain distributions within the microscale a subsequent micromechanical computation is performed in step four. For this purpose, the deformation gradient tensor is logged at each integration point within a porous region of the macroscopic FE model. To enable the logging of the displacement gradient tensor, the homogenized constitutive behavior of porous regions are defined using a user materials subroutine (UMAT) [68]. The deformation gradient tensor of a critical area (e.g. with a high stress within a porous region) is used to compute the symmetric displacement gradient tensor (cf. Section 4.3.2.2) which is then applied to an RVE. In the last step the stress and strain distributions obtained from the micromechanical model are evaluated.
The presented sequential multiscale approach features a quick and computationally inexpensive method to incorporate microstructural influences into the component layout and thus enabling an industrial application. However, the sequential multiscale method is not able to account for nonlinear loading path dependencies of the material properties, such as an initially isotropic plate with randomly distributed holes which is deformed in two steps as shown in Figure 4.17 (a). In the first step a uniaxial deformation in **x** direction is preformed causing a plastification at the edge of the holes (Figure 4.17 (b)). In the second step the plate is deformed in **y** direction. The plastification caused by the deformation in **x** direction leads to a dependency of the stiffnesses of the plate on the loading direction (Figure 4.17 (c)). The stiffness in **x** direction can be described by the Reuss bound assuming a sequential arrangement of plastified and non plastified material whereas the stiffness in **y** direction can be described by the Voigt bound which assumes a parallel arrangement of the plastified and non plastified portions of the material. The former plastification caused by the deformation in **x** direction has almost no influence on the stiffness of the plate in **y** direction. This loading path dependent behavior of the material can not be accounted for by the sequential multiscale model but necessitates a concurrent multiscale model where the material behavior is updated according to the current loading path as explained in the following chapter.

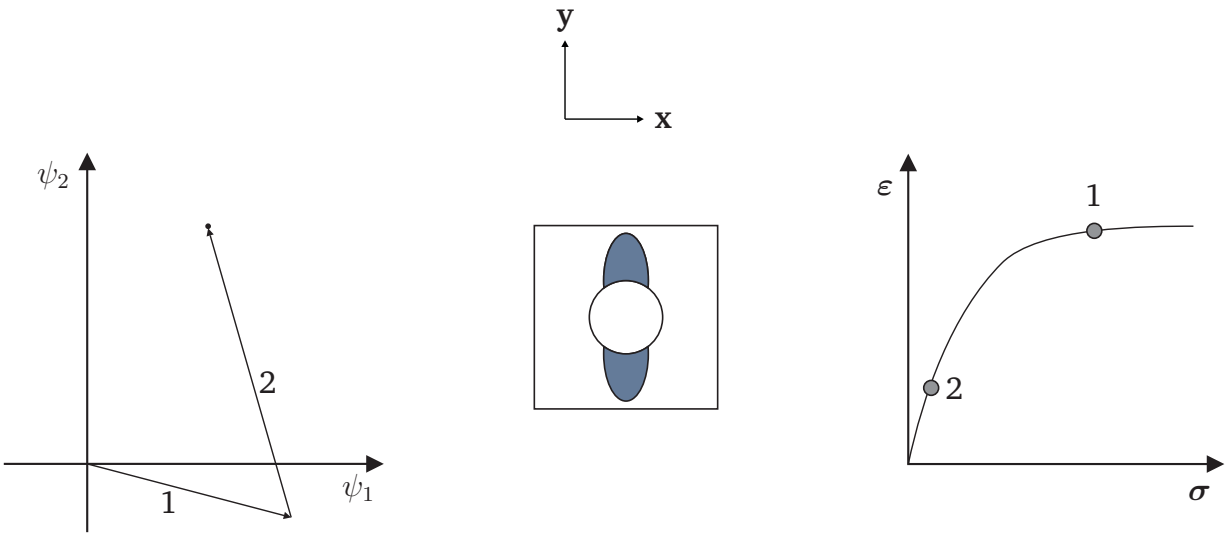

(a) (b) (c)

Figure 4.17: Schematic representation of the loading path dependency of the material behaviors. (a) Loading path to reach the final deformation within two sequential deformations(ψ_1 is the logarithmic strain in **x** direction andψ_2 is the logarithmic strain in **y** direction. (1) the sample is deformed uniaxially in **x** direction, (2) the sample is deformed uniaxially in **y** direction; (b) the grey regions at the hole are plastically deformed by the first deformation step, the sample now shows a stiffness dependency on the loading direction; (c) the sample stiffness in **x** direction has significantly decreased (point 1 in the stress strain curve) whereas the sample stiffness in **y** direction has only changed slightly (point 2 in the stress strain curve). The sequential multiscale model is not capable to account for this loading path dependent constitutive behavior.

4.3.2 Concurrent Multiscale Model

The term concurrent multiscale models means that the models covering different length scales are run in parallel, where certain quantities are exchanged throughout the computation. In in our case the macroscopic model representing a component provides the deformation state and the micromechanical model representing the component materials microstructure provides the constitutive law for the macroscopic model. Thereby a concurrent multiscale computation allows to consider the component's locally varying microstructure and nonlinear loading dependencies of the materials constitutive behavior in the layout process. This yields more accurate results compared to a computation based on a macroscopic continuum theory only.

As of today there is no standard routine to conduct such concurrent multiscale computations using a commercial FE code. Hence there is a clear need to develop concurrent multiscale solution schemes based on commercial FE packages, which will allow an industrial application. In Figure 4.18 the rough concept of the concurrent multiscale approach introduced within this work is depicted.

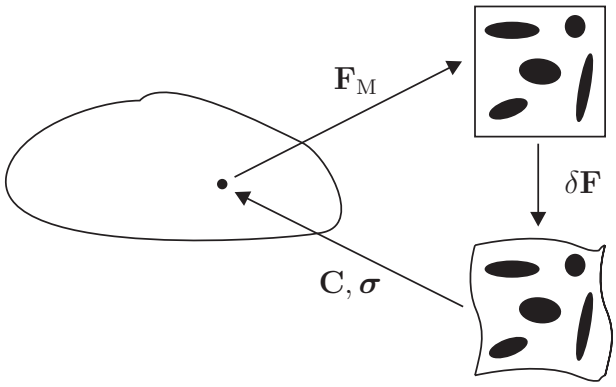

Figure 4.18: Schematic representation of the scale cuppling by a concurrent multiscale approach. The macroscopic model provides the deformation gradient $\mathbf{F}_{\mathrm{M}}$. Based on the deformation gradient the micromechanical model provides the update of the Chauchy stress $\boldsymbol{\sigma}$. Furthermore the updated Jacobian $\mathbf{C}$ is calculated by perturbations of the deformation gradient $\delta\mathbf{F}$.

4.3.2.1 Scale Coupling Concept

The implementation of the multiscale framework is realized using the commercial FE code Abaqus and the programming languages Python and Fortran. It is inspired by the works reported in [7, 27, 29, 30, 77, 78, 79].

A draft of the scale coupling concept is depicted in Figure 4.19. The microstructure of the macroscopic component is represented by periodic representative volume element models, which are coupled to the macroscopic integration points. As can be seen in Figure 4.19, the multiscale computation scheme is realized using the Abaqus solver for the macro and microscale boundary value problems and incorporating user subroutines as well as Python scripts to govern and link the models on the different scales. This will be explained in more detail in the following.

At the beginning of a macroscopic increment the user material subroutine UMAT is called at every integration point. The subroutine obtains the Cauchy stress and the deformation gradient at the beginning of the increment as well as a predicted deformation gradient at the end of the increment. With the aid of these quantities the micromechanical model assigned to the macroscopic integration point provides the update of the macroscopic stress as well as the material Jacobian for the next increment.

- Update of the stress state
  Based on the deformation gradient tensor predicted by Abaqus a symmetric displacement gradient tensor is calculated and imposed upon the micromechanical model. The homogenized stresses obtained from the micromechanical model are used to update the macroscopic stress. The calculation of the symmetric displacement gradient tensor and the micromechanical homogenization are controlled by

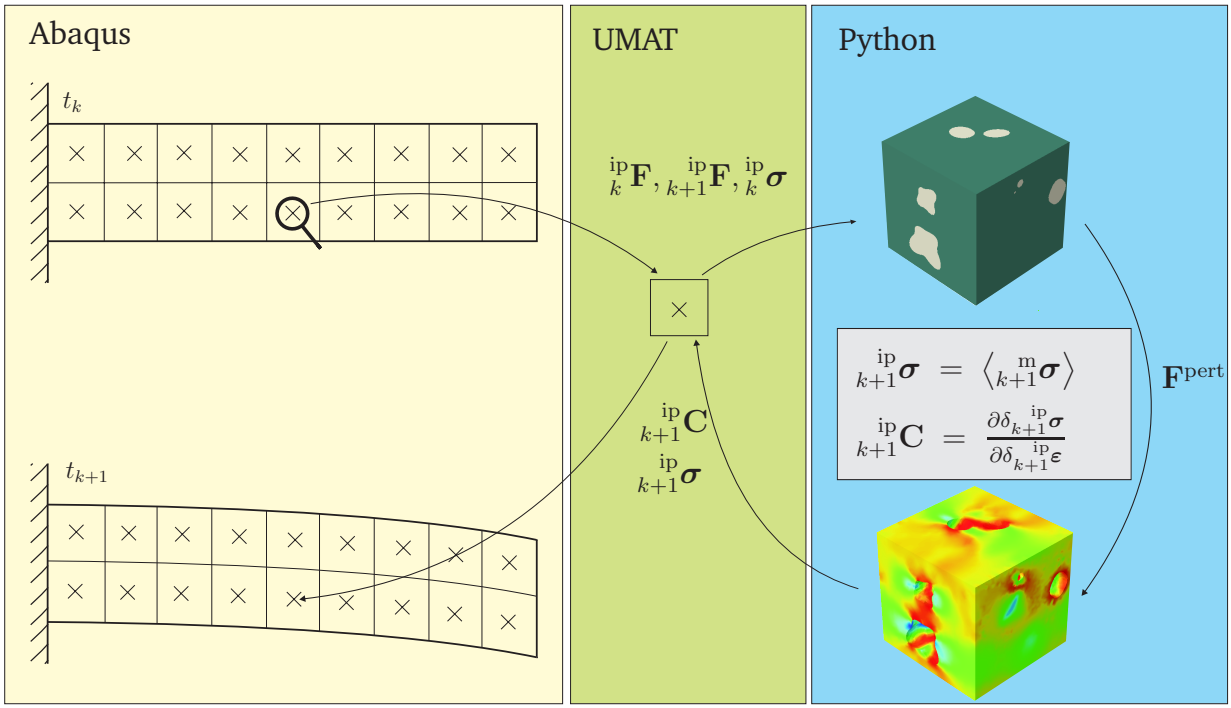

Figure 4.19: Implementation scheme of the multiscale framework. The user subroutine UMAT is used as a mediator between the macro and micro scale.

Python scripts. The resulting homogenized stress values are passed to the macroscopic model using the UMAT subroutine.

- Material Jacobian
  The material Jacobian is calculated in terms of a numerical tangent $\mathbf{C} = \frac{\Delta\boldsymbol{\sigma}}{\Delta\boldsymbol{\varepsilon}}$ based on perturbations of the micromechanical volume element deformation. The homogenized stresses and strains of n closely neighboring deformation states (perturbations of the current deformation) of the micromechanical model are computed [27]. From the homogenized stresses and strains obtained by these micromechanical tests the numerical tangent stiffness tensor $\mathbf{C} = \frac{\Delta\boldsymbol{\sigma}}{\Delta\boldsymbol{\varepsilon}}$ is calculated and returned to the macroscopic FE model using the UMAT subroutine.

A detailed description on how to initialize a multiscale model using Abaqus/CAE is provided in Appendix B.

4.3.2.2 Implementation of the Solution Scheme

The multiscale framework developed within this work incorporates user subroutines as well as Python scripts to control the computation. The user subroutines used by the multiscale framework are the SDVINI to define initial solution dependent state variables, the UMAT to define a material's mechanical behavior and the UVARM to generate element output [68]. At the beginning of the computation the SDVINI subroutine is called at each

integration point to initialize the solution dependent state variables (SDV) [68]. These variables are utilized to govern local microstructural parameters. In case of the cantilever beam treated in Appendix B, the only microstructural parameter, which is varied is the pore volume fraction with respect to the length coordinate (X) of the integration point. After the solution dependent state variables are defined, the UMAT subroutine is called at each integration point of the macroscopic model. Per definition the UMAT must provide updates of the material Jacobian, the stress state and the SDVs as return values [68]. Since the SDVs are only used to define the parameters to initialize the micromechanical volume element models, they are not modified.
The updates of the material Jacobian and the stress state are obtained from micromechanical FE models. This is realized using the UMAT as a mediator between macroscopic and the microscopic scales. When called at a macroscopic integration point, the UMAT obtains a set of variables listed in Table 4.1[3]. These variables are used to control the multiscale computation and are written to a text file. This enables for the variables to be transferred between the different scripts incorporated within the multiscale computation scheme. A Python routine governing the micromechanical model is called from

Table 4.1: Relevant variables for the multiscale framework available within UMAT.

Variable	Identifier
Element number	NOEL
Integration point number	NPT
Increment number	KINC
Step number	KSTEP
Jacobian matrix	DDSDDE
Stresses	STRESS
Deformation gradient at the end of the increment	DFGRD1(3,3)

within the UMAT. The first time this Python script is called at an integration point, the micromechanical volume element model has to be initialized. Therefore an altered version of the automated microstructure model generation algorithm is used. In comparison to the algorithm described in Chapter 4.2 the microstructural parameters are not manually defined by the user. Instead these parameters are set to default values given in Table B.1. Next, the text file containing the parameters to govern the multiscale computation is read. Thereby the therein stored parameter are initialized within the Python script and, in case any SDVs are defined, the respective default microstructural parameters are altered. Based on the resulting parameter set a periodic volume element model is generated. The micromechanical model is assigned to its corresponding integration

[3]A complete list of variables obtained by the UMAT is given in [68]. The given variables are constricted to the ones used to govern the multiscale computation

point in the macroscopic model using a naming convention. The structure of the micromechanical model name is given by

$$\text{mm\_init\_el}\langle\text{NOEL}\rangle\text{\_npt}\langle\text{NPT}\rangle$$

where $\langle$NOEL$\rangle$ is the element number and $\langle$NPT$\rangle$ is the integration point number. This ensures that the micromechanical model is uniquely assigned to its corresponding integration point in the macroscopic model. After the micromechanical model is generated, the simulations to compute the stress state and the material Jacobian are conducted.
For this purpose the deformation gradient at the end of an increment, which is predicted by Abaqus and obtained via the UMAT (cf. Table 4.1) is split into a proper orthogonal tensor $\mathbf{R}$ describing the rigid body rotation and the symmetric tensor $\mathbf{U}$ describing a pure homogeneous deformation

$$\mathbf{F} = \mathbf{R}\,\mathbf{U} \tag{4.33}$$

using a right polar decomposition. The symmetric displacement gradient tensor $\nabla\mathbf{u}$ is calculated by subtracting the identity matrix $\mathbf{I}$ from $\mathbf{U}$

$$\nabla\mathbf{u} = \mathbf{U} - \mathbf{I}\,. \tag{4.34}$$

The tensor $\nabla\mathbf{u}$ is imposed upon the micromechanical volume element model utilizing periodic boundary conditions (cf. Chapter 4.2). The homogenized stress values obtained from the solution of the micromechanical boundary value problem are used to update the macroscopic stress state.
To update the material Jacobian the constitutive law in an incremental formulation

$$\Delta\boldsymbol{\sigma} = \mathbf{C}\,\Delta\boldsymbol{\varepsilon} \tag{4.35}$$

is considered in its most general form where $\mathbf{C}$ is the stiffness tensor and $\Delta\boldsymbol{\sigma}$ and $\Delta\boldsymbol{\varepsilon}$ denote the incremental stress and strain difference, respectively.
Assuming arbitrary anisotropy of the homogenized material requires to identify all 21 independent components[4] of the stiffness tensor $\mathbf{C} = \frac{\partial\boldsymbol{\sigma}}{\partial\boldsymbol{\varepsilon}}$. To compute the stiffness tensor a perturbation approach is employed testing ideally infinitesimally close neighboring deformation states as described by Temizer [27]. This technique allows to approximate the partial derivative $\mathbf{C} = \frac{\partial\boldsymbol{\sigma}}{\partial\boldsymbol{\varepsilon}}$ by the numerical tangent $\mathbf{C} = \frac{\Delta\boldsymbol{\sigma}}{\Delta\boldsymbol{\varepsilon}}$. At each integration point of the macroscopic simulation six perturbations of the micromechanical deformation state at the end of the increment are conducted. The displacement gradient tensors $\nabla\mathbf{u_1} - \nabla\mathbf{u_6}$ defining the boundary value problem to conduct the micromechanical tests are generated

[4]For a theoretical treatment the reader is referred to [80] or [73]

by slightly varying independent components of the symmetric displacement gradient tensor at the end of an increment by small values $0 < \delta \ll 1$. The displacement gradient tensors for the perturbations can be written as

$$\nabla\mathbf{u_1} = \begin{pmatrix} u_{11}+\delta & u_{12} & u_{13} \\ u_{21} & u_{22} & u_{23} \\ u_{31} & u_{32} & u_{33} \end{pmatrix} \qquad \nabla\mathbf{u_2} = \begin{pmatrix} u_{11} & u_{12} & u_{13} \\ u_{21} & u_{22}+\delta & u_{23} \\ u_{31} & u_{32} & u_{33} \end{pmatrix}$$

$$\nabla\mathbf{u_3} = \begin{pmatrix} u_{11} & u_{12} & u_{13} \\ u_{21} & u_{22} & u_{23} \\ u_{31} & u_{32} & u_{33}+\delta \end{pmatrix} \qquad \nabla\mathbf{u_4} = \begin{pmatrix} u_{11} & u_{12}+\delta & u_{13} \\ u_{21}+\delta & u_{22} & u_{23} \\ u_{31} & u_{32} & u_{33} \end{pmatrix}$$

$$\nabla\mathbf{u_5} = \begin{pmatrix} u_{11} & u_{12} & u_{13}+\delta \\ u_{21} & u_{22} & u_{23} \\ u_{31}+\delta & u_{32} & u_{33} \end{pmatrix} \qquad \nabla\mathbf{u_6} = \begin{pmatrix} u_{11} & u_{12} & u_{13} \\ u_{21} & u_{22} & u_{23}+\delta \\ u_{31} & u_{32}+\delta & u_{33} \end{pmatrix}$$

resulting in three normal and three shear perturbations. For each perturbation a separate micromechanical FE simulation is conducted. Therefore the *restart* functionality of Abaqus is used defining a restart step with altered boundary conditions for the stress update simulation. The modified dummy node displacements are updated, whereas the remaining displacement boundary conditions are replaced by traction boundary conditions. The value of the traction force at the respective dummy node is equated to the reaction force obtained from the stress update simulation. Using a micromechanical boundary value problem with mixed boundary conditions [5] proved to be more stable compared to applying Dirichlet type boundary conditions for all degrees of freedom of the dummy nodes. After the micromechanical testing the differences in the homogenized stress and strain results compared to the stress update simulation are calculated. The resulting stress differences $\Delta\boldsymbol{\sigma}_i$ and strains differences $\Delta\boldsymbol{\varepsilon}_i$ are related by the incremental constitutive equation

$$\langle \Delta\boldsymbol{\sigma}_i \rangle = \mathbf{C} \, \langle \Delta\boldsymbol{\varepsilon}_i \rangle \tag{4.36}$$

where $\mathbf{C}$ is the sought-after numerical tangent. The index $i \in \{1, 2, \ldots, 6\}$ denotes the respective perturbation. From the six micromechanical tests a set of linear equations is obtained, which can be written in matrix form as

$$\mathbf{A} \, \mathbf{x}_{\mathrm{hom}} = \mathbf{b}_{\mathrm{hom}} \tag{4.37}$$

[5] Dirichlet type boundary conditions are defined on the degrees of freedom of the dummy nodes corresponding to the direction of the perturbation whereas Neumann type boundary conditions are defined on the remaining degrees of freedom of the dummy nodes.

where the matrix $\mathbf{A}$ contains the homogenized strains obtained from the micromechanical tests, the vector $\mathbf{b}_{\mathrm{hom}}$ contains the homogenized stresses obtained from the micromechanical tests and the vector $\mathbf{x}_{\mathrm{hom}}$ comprises the sought-after components of the numerical tangent stiffness tensor. An expanded version of Equation (4.37) is given in Appendix A. Obviously Equation (4.37) constitutes an overdetermined linear system of equations. Typically an exact solution of Equation (4.37) is not possible. Hence the norm of the residuum

$$\mathbf{r} = \mathbf{A}\ \mathbf{x}_{\mathrm{hom}} - \mathbf{b}_{\mathrm{hom}} \tag{4.38}$$

is minimized (see [81]), which can be written as

$$F(x) = \mathbf{r}(x)^{\mathrm{T}}\mathbf{r}(x) = \mathbf{x}_{\mathrm{hom}}^{\mathrm{T}}\mathbf{A}^{\mathrm{T}}\ \mathbf{A}\ \mathbf{x}_{\mathrm{hom}} - 2\mathbf{x}_{\mathrm{hom}}^{\mathrm{T}}\ \mathbf{A}^{\mathrm{T}}\ \mathbf{b}_{\mathrm{hom}} + \mathbf{b}_{\mathrm{hom}}^{\mathrm{T}}\ \mathbf{b}_{\mathrm{hom}} \rightarrow \text{min!} \tag{4.39}$$

The necessary condition to minimize $F(x)$ is $\nabla F(x) = 0$, which leads to the normal equation

$$\mathbf{A}^{\mathrm{T}}\mathbf{A}\ \mathbf{x}_{\mathrm{hom}} = \mathbf{A}^{\mathrm{T}}\mathbf{b}_{\mathrm{hom}} \tag{4.40}$$

providing a least square fit for the unknown components of $\mathbf{x}$, which are calculated by

$$\mathbf{x}_{\mathrm{hom}} = \left(\mathbf{A}^{\mathrm{T}}\mathbf{A}\right)^{-1}\mathbf{A}^{\mathrm{T}}\ \mathbf{b}_{\mathrm{hom}}\ . \tag{4.41}$$

The obtained entries of the secant stiffness tensor $\mathbf{C}$ (components of $\mathbf{x}$) are passed to the macroscopic FE model by the UMAT subroutine. The update of the stress state and the material Jacobian as explained above is repeated at each increment of the macroscopic computation.

Chapter 5

Results and Discussion

The results obtained from experimental and modeling investigations of porous cast samples presented in the previous chapters will be discussed and compared in the following. The geometrical characteristics of the porous samples and computer generated microstructures are correlated. Furthermore the mechanical behavior of porous samples is compared to the predictions of the micromechanical model.
The aim of this chapter is to study and discuss the results of the micromechanical model as well as to correlate the experiment and modeling approach. This will also provide ideas for further improvement.

5.1 Micromechanical Modeling Results

5.1.1 Microstructural Model Geometries

To compare the results of the micromechanical finite element solution to analytical results, volume element models featuring a spatially random distribution of pores are used. Some realizations with varying pore volume fractions v_p are depicted in Figure 5.1. The volume element models are meshed using linear tetrahedral elements (Abaqus element type: C3D4 [68]) with an average seed size of 0.3. The seed size determines the average edge length of an element. However, the element edge length might vary depending on the local geometry. For contours with a high curvature the edge length of the elements is adjusted to allow for complex geometries to be adequately meshed.

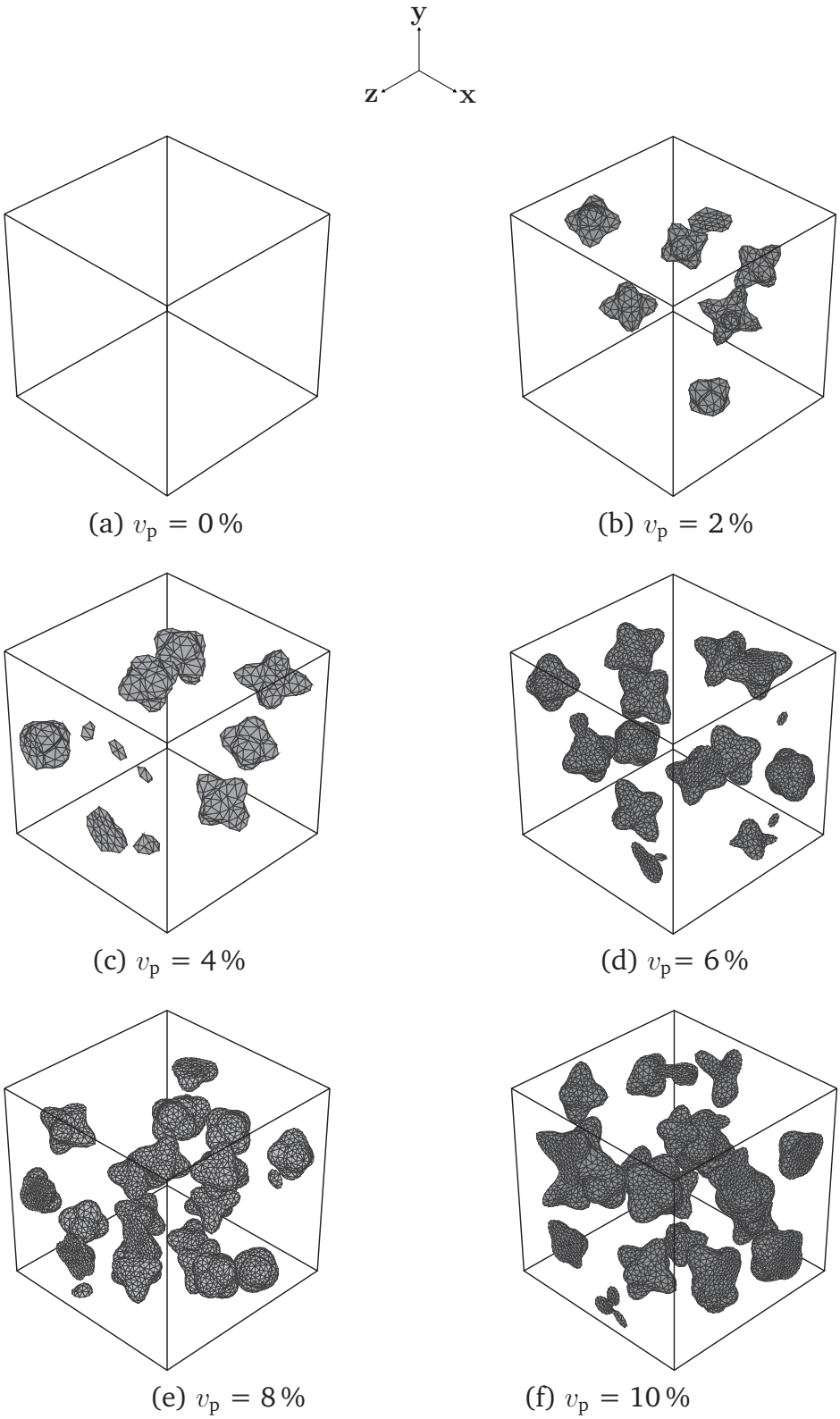

(a) v_p = 0 %

(b) v_p = 2 %

(c) v_p = 4 %

(d) v_p= 6 %

(e) v_p = 8 %

(f) v_p = 10 %

Figure 5.1: Three dimensional representation of volume element models with pores (grey). The models contain a pore volume fraction between 0 % and 10 %. The pores are distributed spatially random.

5.1.2 Convergence Behavior of the Model

In order to obtain reliable results, the FE models have to be examined for mesh and property convergence. In the present work, mesh convergence is defined as reached, if the homogenized response of the micromechanical model does not change by more than 1 % compared to the finest mesh that was tested. The results of a mesh convergence study are presented in Figure 5.2. For this study the same volume element geometry is meshed using an initial seed size of 1.0, 0.7, 0.5, 0.3 and 0.2. This results in 27×10^3 C3D4 elements of the coarsest seed size and 619×10^3 C3D4 elements of the finest mesh. It can be seen in Figure 5.2 that the second finest mesh which is generated prescribing a initial seed size of 0.3 fulfills the convergence requirement. Thus all further studies presented within this work are meshed using a seed size of 0.3. This ensures mesh convergence on one hand, while on the other hand the numerical costs are kept within reasonable limits.

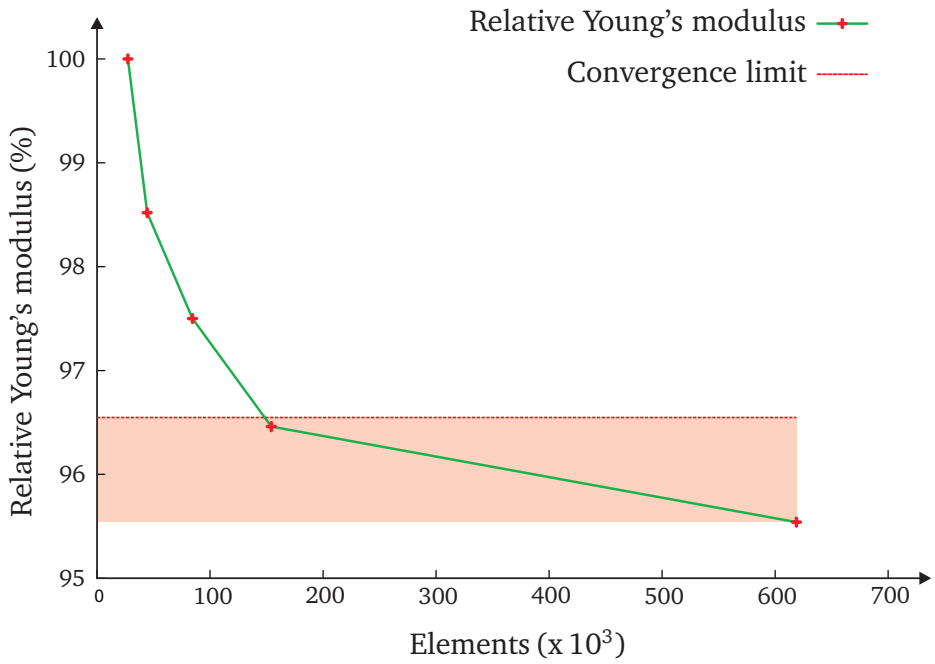

Figure 5.2: Mesh convergence study. A volume element model is meshed with a varying mesh resolution and the homogenized Young's module is evaluated. The meshes are generated using initial seed sizes between 1.0 and 0.2 resulting in 27328 to 618876 elements to discretize the volume element model. The convergence criterion is defined as fulfilled, once the Young's modulus does not vary more than 1 % compared to the finest mesh tested. A seed size of 0.3 resulting in a mesh with 154207 elements is found sufficient to obtain mesh convergence.

To test for property convergence, the size of the volume element model is increased systematically. Both periodic as well as uniform displacement boundary conditions were applied to study the convergence behavior of the micromechanical volume element models. The largest volume element models used within this study have an edge length of

200 μm and contain on average 20 pores, whereas the smallest models have an edge length of 50 μm and contain only 1 pore. Even though the size of the volume element models is varied, the pore volume fraction of all micromechanical models evaluated for the convergency study is 10 %. For each micromechanical model size the mean value and standard deviation of the Young's modulus and the 98 % quantile of the plastic equivalent strain is evaluated from 100 simulations, Figure 5.3. We define property convergence as reached, if the mean of the Young's modulus and the mean of the 98% quantile of the plastic equivalent strain do not change by more than 1 % when increasing the edge length of the volume element model by 50 μm. In Figure 5.3 these restrictions are indicated by the RVE limit size. Clearly, a minimum size of the unit cell is needed in order to obtain viable results. If the micromechanical model is too small, the results are strongly influenced by the boundary conditions. This is especially critical for the quantile evaluation of the plastic equivalent strain as shown in Figure 5.3 (b). The difference between the mean values of the 98 % quantile of the plastic equivalent stress from the smallest and the largest tested volume element models is 17 %. The increase of the mean value of the 98 % quantile of the plastic equivalent strain is due to the higher complexity of the interaction of the increased number of inclusions in larger micromechanical finite element models. An increasing micromechanical volume element size not only leads to convergence of the mean values, but also the standard deviation of the evaluated quantities decreases. The standard deviation of the evaluated Young's modulus decreases by 46 % for models using periodicity boundary conditions and by 36% using uniform displacement boundary conditions when comparing the largest to the smallest models.

As can be seen, the results obtained from the micromechanical model largely depend on the representativeness of the volume elements. In the conducted study a minimum edge length of the micromechanical models corresponding to 150 μm was determined as sufficiently large. This corresponds with a minimum relative volume element size of 0,75 as can be seen in Figure 5.3.

Even though volume element models with an edge length larger than 150 μm can be considered RVEs, the standard deviation of the results can be further decreased by using even larger models, though causing higher computational costs. Bearing these thoughts in mind the volume model size is adjusted based on the problem. Within this convergence study the largest finite element models contain approximately 150000 finite elements. For the simulations the iterative solver from Abaqus/Standard was used. The total CPU time to perform one calculation is between 3000 and 5000 seconds using an Intel Xeon X5550 CPU with a clock speed of 2.66GHz on a system with 12 GB RAM. This is acceptable and all further simulations presented in this work are based on the largest tested micromechanical volume element models corresponding to an edge length of 200 μm.

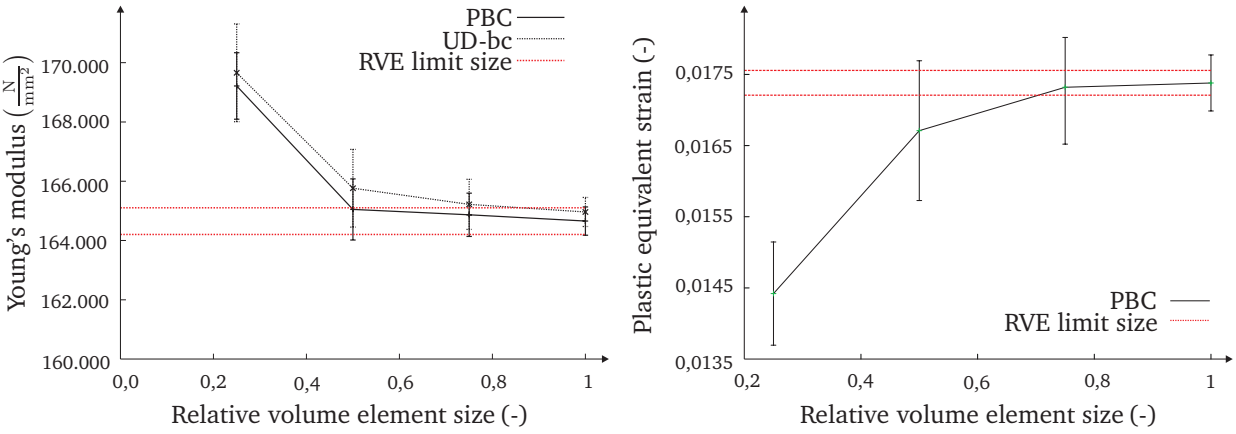

Figure 5.3: Representative volume element size study. The finite element models evaluated for this study exhibit a pore volume fraction of 10 %. Each data point represents 100 simulations: (a) the effective elastic response; (b) the dependence of the 98 % quantile of the plastic equivalent strain on the volume element size (cf. Taxer [82]).

5.1.3 Elastic Behavior

After assuring convergence, the influence of the pore volume fraction on the effective Young's modulus and shear modulus is investigated. To quantify the influence of pores on the Young's modulus and the shear modulus, numerical volume element studies with a varying pore volume fraction are carried out.

Since the sample size did not allow for a standardized evaluation of the effective Young's modulus, the results gained by the numerical volume element model are compared to results gained by analytical methods. For porous materials the lower analytical bounds are vague, since they degrade if pores are considered as a second phase. This leaves a large gap between upper and lower bounds. Thus only upper bounds, namely the Voigt and the upper Hashin-Shtrickman bounds are compared to the results obtained from the finite element model. The results from the analytical as well as the finite element models for the Young's modulus are depicted in Figure 5.4 (a). The Voigt bound constitutes the highest possible bound. If any results obtained from the volume element model would exceed this bound, it would be an indication of an error within the volume element model. The upper Hashin-Shtrikman bound was chosen since the assumptions of Hashin and Shtrickman are very similar to the geometry assumptions of the volume element model: A spatially random distribution of pores. The assumptions differ mainly in the shape of the pores. Whereas Hashin and Shtrickman assume spherical pores, the pore geometry of the numerical model is based upon a Boolean union of ellipsoids, which is considerably more complex.

The comparison of the results obtained form the volume element model and the analytical bounds enables to simultaneously look at two effects: Comparing the FE results to the Voigt bound enables to check for plausibility of the FE results, whereas the comparison of the FE results with the upper Hashin-Shtrickman bound enables to evaluate the influence of the pore shape on the effective Young's modulus. The result presented in Figure 5.4 (a) show that the upper Hashin-Shtrickman bound is congruent to the predictions of the micromechanical model. This indicates that the shape of the pores has a minor influence on the resulting effective Young's modulus. Thus, as long as the pores exhibit a spatially random distribution the Hashin-Shtrickman bounds provide a reliable and quick estimate of the effective Young's modulus.
Similarly to the apparent Young's modulus the apparent shear modulus is evaluated. The results from the finite element models are compared to the Voigt bound and to the upper Hashin-Shtrikman bound as shown in Figure 5.4 (b). Again the Voigt bound overestimates the shear modulus, while the upper Hashin-Shtrikman bound and results obtained from the finite element approach are in good agreement. Hence, the conclusions drawn from the evaluation of the Young's modulus also hold true for the shear modulus. After

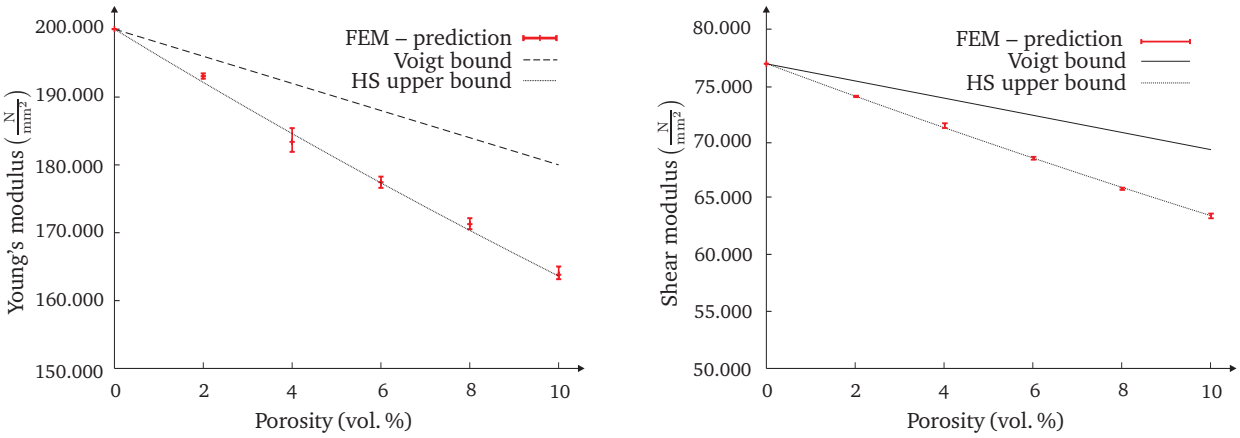

Figure 5.4: Dependency of the Young's modulus (a) and the shear modulus (b) on the pore volume fraction. The pores within the finite element models are distributed uniformly random. The error bars denote the standard deviation. It can be seen that the Hashin-Shtrikman bounds are in good agreement with the finite element solution.

investigating the elastic material behavior a closer look on the plastic material behavior will be taken in the following.

5.1.4 Plastic Behavior

Homogenized stress strain curves for RVEs with a pore volume fraction varying between 0 % and 10 % are depicted in Figure 5.5. Each curve represents the homogenized stress

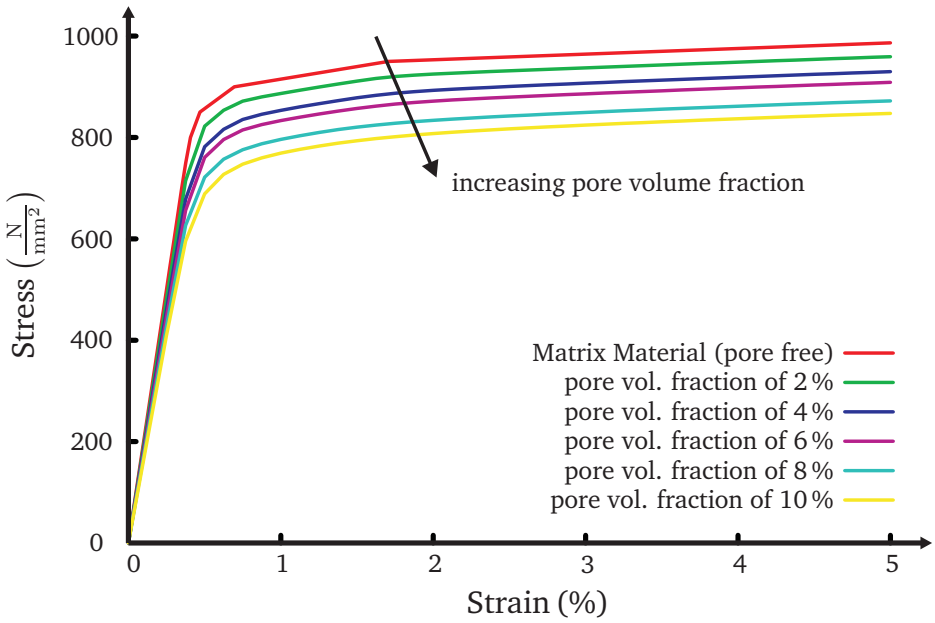

Figure 5.5: Homogenized stress strain curves predicted by the micromechanical finite element model for pore volume fractions between 0 % and 10 %. The Young's modulus as well as the offset yield stress decreases with an increasing pore volume fraction.

strain curve obtained from one RVE. The offset yield stress decreases with increasing pore volume fraction. The dependency of the offset yield stress on the pore volume fraction as predicted by the micromechanical model is given in Figure 5.6. For each pore volume fraction a total of 10 Simulations are considered. The results for the homogenized offset yield stress for a specific pore volume fraction exhibit a negligibly small scatter. This is an indicator that the modeled volume element is representative for the evaluation of the offset yield stress. Next to the homogenized offset yield stress, the onset and evolution of plastic deformation within a porous material is investigated. Furthermore the influence of the pore shape on the plastic deformation of the surrounding material is studied. A local investigation of the stress and strain distributions reveals that plastic deformation is initiated in the vicinity of pores. In Figure 5.7 an RVE with a pore volume fraction of 10 % is depicted. The depicted micromechanical volume element model is exhibited to a uniaxial global strain of 0.35 %. The strain causes a volume averaged Cauchy stress of 637 $\frac{N}{mm^2}$. In Figure 5.7 the red areas designate regions where the local Cauchy stress exceeds the yield stress of the matrix material. The pores are represented in a light blue color. It is noticeable that the matrix material exceeds the plastic limit in the vicinity of the pores even though the global stress level of 637 $\frac{N}{mm^2}$ is well below the yield stress of the pore free material. For the prescribed global strain 5.9 % of the matrix material deforms plastically. The successive plastification of the matrix material is shown in Table 5.1. Furthermore Table 5.1 shows the evolution of the homogenized equiva-

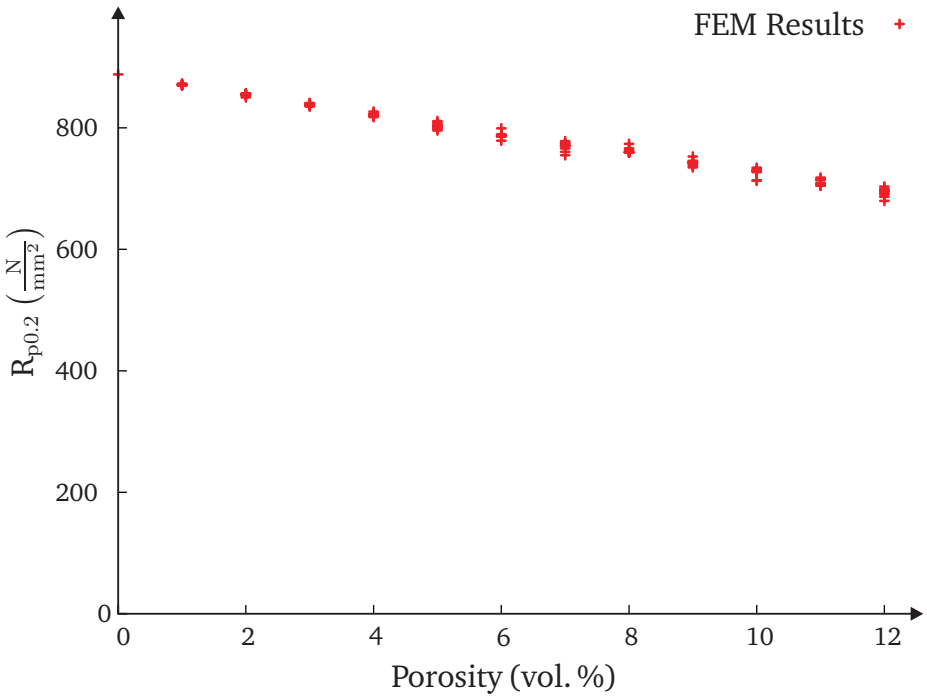

Figure 5.6: Dependency of the homogenized offset yield stress on the pore volume fraction based on the evaluation of micromechanical models. For each pore volume fraction 10 calculations are evaluated. The low scatter of the results indicated, that the volume element models are representative.

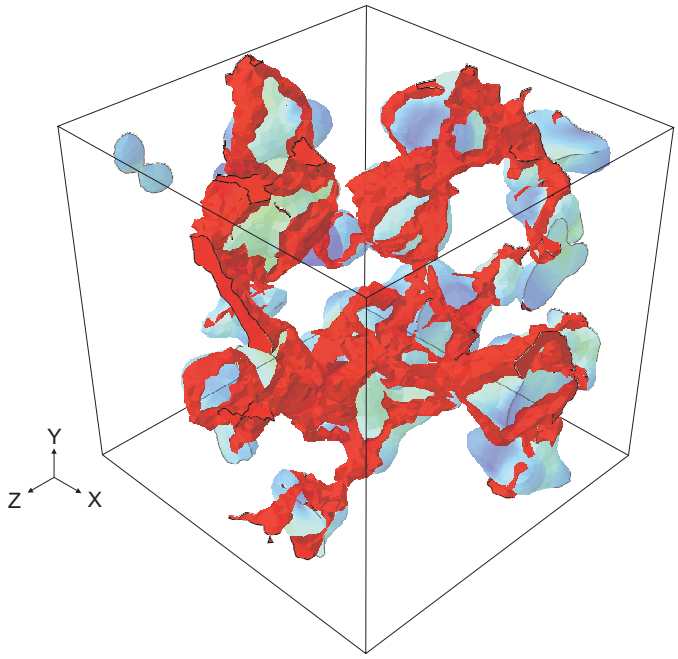

Figure 5.7: Visualization of the plastic regime within the RVE. The plastic region builds a network between the pores. It is assumed that cracks will develop in these areas and thus lead to pore coalescence.

Table 5.1: Evolution of the von Mises stress, plastified volume fraction and homogenized equivalent plastic strain based on the homogenized strain in **X** direction for an RVE with a pore volume fraction of 10%.

Homogenized strain (%)	Homogenized stressσ_{M} (MPa)	Plastified volume fraction (%)	Homogenized $\varepsilon_{\mathrm{peeq}}$ (-)
0.35	637	5.9	0.0000602
0.70	750	79.4	0.0023742
1.15	769	94.6	0.0066178

lent plastic strain (ε_{peeq}) of the matrix material with an increasing averaged strain. The quantile evaluation of the equivalent plastic strain is an important indicator for damage predictions. This emphasizes the relevance of the micromechanical results gained by the introduced FE model for the component layout.

5.2 Comparison of Experimental and Modeling Results

5.2.1 Characteristic Pore Geometries

As shown above, the pore volume fraction and pore shape significantly influence the mechanical behavior of a porous material. Thus, a realistic representation of these characteristics is vital to obtain reliable results from a microstructure model predicting the influence of pores on the mechanical material behavior. To gain an understanding of the geometrical representativeness of the microstructure model, three sets of computer generated microstructures with different pore volume fractions are assessed. The statistically evaluated pore volume fraction, pore volume distribution, pore shape and the spatial pore distribution obtained from the volume element models are correlated to those obtained from CT scans of porous cast samples with an equal pore volume fraction. The samples and their respective pore volume fraction used for this study are

- sample 2-01 with a pore volume fraction of 5.76 %,
- sample 3-03 with a pore volume fraction of 7.60 % and
- sample 4-01 with a pore volume fraction of 9.56 %.

For these samples the afore mentioned characteristics are evaluated based on CT data. The pore size distribution is modeled by a Lognormal distribution, which is commonly used to describe the volume distribution of particles [47]. The pore shape is also modeled using a Lognormal distribution. The results of the CT data evaluation of the samples given above are summarized in Table 5.2.

Table 5.2: Experimentally determined characteristics of the microstructure geometry.

Parameter	Sample 2-01	Sample 3-03	Sample 4-01
Pore volume fraction (vol. %)	5.31	7.60	9.56
Single pore volume distribution σ	1.74	1.40	1.81
Single pore volume distribution μ	6.61	5.43	6.12
Aspect ratio distribution σ	0.64	0.61	0.48
Aspect ratio distribution μ	0.53	0.42	0.58
Maximum aspect ratio	12.42	10.12	9.42
Degree of randomness R	1.05	1.18	1.16

The characteristics of the respective samples given in Table 5.2 are correlated to 500 computer generated models. The input parameters for the model generation are given in Table 5.3. The parameters governing the Lognormal pore shape distribution and the Lognormal pore volume distribution are obtained by linear fits of the experimental data and can be calculated using Equations (3.3) and (3.4) and Equations (3.13) and (3.14), respectively. A linear fit of experimental data naturally entails that the individual pa-

Table 5.3: Input parameter set for the computer generated microstructure models.

Parameters	Sample 2-01	Sample 3-03	Sample 4-01
Pore volume fraction (vol. %)	5.31	7.60	9.56
Single pore volume distribution σ	1.63	1.70	1.76
Single pore volume distribution μ	6.24	6.36	6.46
Aspect ratio distribution σ	0.47	0.48	0.49
Aspect ratio distribution μ	0.66	0.64	0.63
Maximum aspect ratio	10	10	10
Spatial randomness R	1.0	1.0	1.0

rameters given in Table 5.2 are not exactly matched by the input parameters. Since the volume element model is intended as a predictive tool, a certain misfit of the parameters obtained by experimental evaluations and the input parameters for the computer generation of microstructure models is unavoidable.

One restriction of the proposed modeling approach is certainly the use of intersecting ellipsoids to represent the pore shape. The aspect ratio of the ellipsoids is used to model the spatial ramification of the pores. This aspect ratio is obtained by a conversion of the pore volume to bounding box volume ratio. The minimum representable volume ratio by the proposed modeling approach is limited by a spherical pore yielding an aspect ratio of 1.0 and a volume ratio of $V_{\mathrm{R}} = 1.91$. This does not coincide with the minimum volume ratio obtained from the CT data which is considerably lower. A remedy for this limitation

would be using Lame curves [83, 84] to construct the model pores which has not been implemented within this work. This would allow for a more general pore shape and enable to represent arbitrary volume ratios. In a Cartesian reference system Lame curves are defined by

$$\left|\frac{x}{a}\right|^m + \left|\frac{y}{b}\right|^m = 1 \tag{5.1}$$

where a and b are the half axes and x, y and m are positive numbers defining the shape of the Lame curve. Conversely to the minimum aspect ratio, the maximum aspect ratio of pores within the micromechanical model is defined as averaging the maximum experimentally determined aspect ratio.

Next to the pore shape, pore size thresholds have to be defined for the microstructure model. The minimum and maximum pore size thresholds largely depend on the size of the volume element model. Within this study the size of the volume element is defined as $200\times200\times200\,\mu m^3$ for a twofold reason. Firstly, it is the minimum volume element size to yield representative results as presented in Chapter 4.2. Secondly the volume element of $200\times200\times200\,\mu m^3$ allows to define a relevant range of pore sizes. The minimum threshold for the pore size is $6250\,\mu m^3$, which equals to a spherical pore of $22.8\,\mu m$ in diameter, which is just above the detection limit of the CT scans preformed within this work. The maximum pore size is defined as $400000\,\mu m^3$ equal to a spherical pore of $91.4\,\mu m$ in diameter. Larger pores are detectable by standard inspection methods. This emphasizes the technical relevance of the minimum and maximum pore sizes. The characteristics of pores, which are not detectable by standard inspection methods, are obtained by the experimental investigations carried out within this work. Furthermore, their influence on the mechanical material behavior was studied both experimentally as well as by the micromechanical model.

For each set of input parameters a total of 500 models are generated. A comparison of the results obtained by a statistical evaluation of the computer generated models and the corresponding variables obtained from the CT data of the respective sample is given in Table 5.4. The geometry generation algorithm is able to match the pore volume fraction with an accuracy of ±0.1 percent to the desired value. However, one needs to keep in mind that the pore volume fraction given in Table 5.4 is evaluated before the finite element discretization of the model. The pore volume fraction changes after the discretization depending on the mesh size of the FE model.

Even though the pore volume fraction closely matches the input parameter, matching a predefined distribution as for example the pore size distribution is a much more difficult matter. The accuracy of the resulting pore size distribution increases with an increasing size of the volume element model. The volume element size determines the number of pores within the model, which in turn influences the representation of the predefined

Table 5.4: Comparison of experimental and computer generated data. The computer generated data represents the average of the set of 500 generated microstructures. Naturally, the averaged quantities deviate form the input parameters, since thresholds are defined for the pore volume distribution and the aspect ratio distribution which hinders an exact representation.

	2-01		3-03		4-01	
Parameter	Sample	Model	Sample	Model	Sample	Model
Pore volume fraction (vol%)	5.31	5.31±0.1	7.60	7.60±0.1	9.56	9.56±0.1
Single pore volume distribution σ	1.74	1.07	1.40	1.09	1.81	1.10
Single pore volume distribution μ	6.61	6.51	5.43	6.54	6.12	6.59
Aspect ratio distribution σ	0.53	0.41	0.42	0.40	0.48	0.41
Aspect ratio distribution μ	0.64	0.74	0.61	0.72	0.58	0.72
Maximum Aspect Ratio	12.42	8.81	10.12	9.28	9.42	9.28
Degree of randomness R	1.05	1.27	1.18	1.25	1.16	1.26

distribution. The more pores are generated, the better the predefined distribution is represented. Unfortunately, increasing the size of the volume element model infers a higher numerical cost to run the FE analysis. Thus a trade off between the model size and the statistical representativeness is needed. As mentioned above, the presented results are based on volume element models with an edge length of 200 µm. This model size coincides with the minimum volume element size to obtain mechanically representative results as shown in Chapter 5.1. Apart from the size of the volume element model, the minimum and maximum thresholds influence the resulting distribution. The more restrictive the thresholds are defined, the worse the experimental pore volume and pore shape distribution can be represented. Nevertheless a quantitative comparison of the resulting distribution parameters for computer generated and experimental data of the respective samples is given in Table 5.4. A more intuitive understanding of the correlation of experiment and model is gained by comparing histograms of the pore sizes and pore shapes. The histogram in Figure 5.8 (a) depicts the relative frequency of pores with a volume in between 100 voxel and 6250 voxel, identified in sample 2-01 based on the CT data. Figure 5.8 (b) depicts the statistical evaluation of the pore size distribution from 500 computer generated geometries. The two histograms show a similar relative frequency of occurring pore sizes. In all three cases the pore size distribution is well represented by the micromechanical modeling approach.

Next to the pore size distribution, the representation of the pore shape is investigated. A histogram showing the relative frequency of pore aspect ratios obtained based on the CT data of sample 2-01 is presented in Figure 5.9 (a). The aspect ratio distribution obtained from the corresponding model geometries is presented in Figure 5.9 (b). Even though the parameters σ and μ to fit the distribution of aspect ratios which were obtained based on the evaluation of the CT data and the simulation data match well (Table 5.4), the

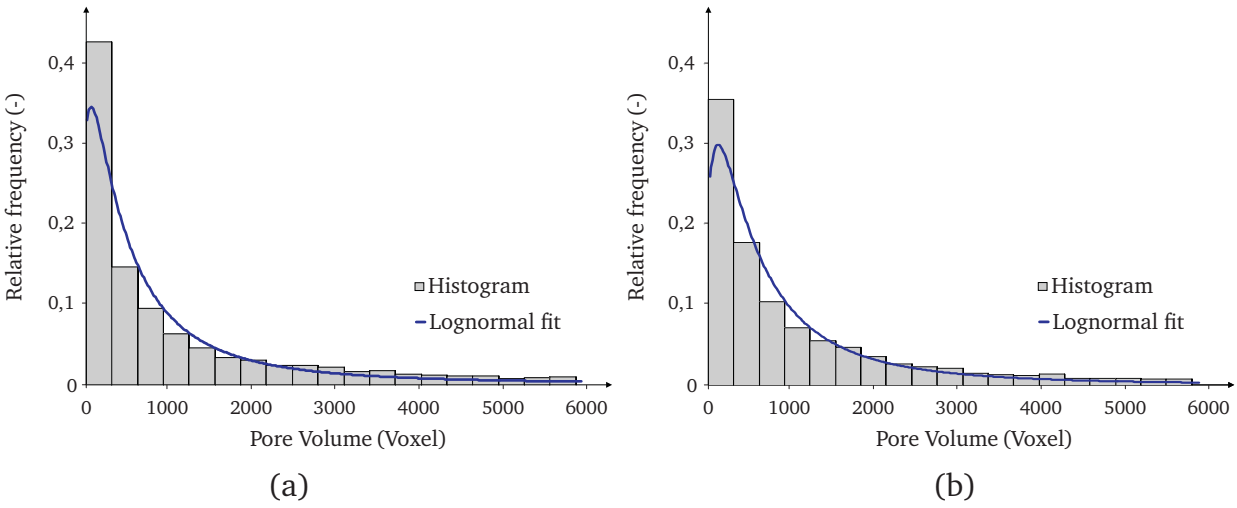

Figure 5.8: Comparison of experimentally observed pore volume fraction in sample 2-01 (a) and simulated (b) pore volume distribution. The pore volume fraction of sample 2-01 is 5.31 %. The simulation yields a very similar pore volume distribution. This is an indicator that the input parameters for the simulation are chosen well.

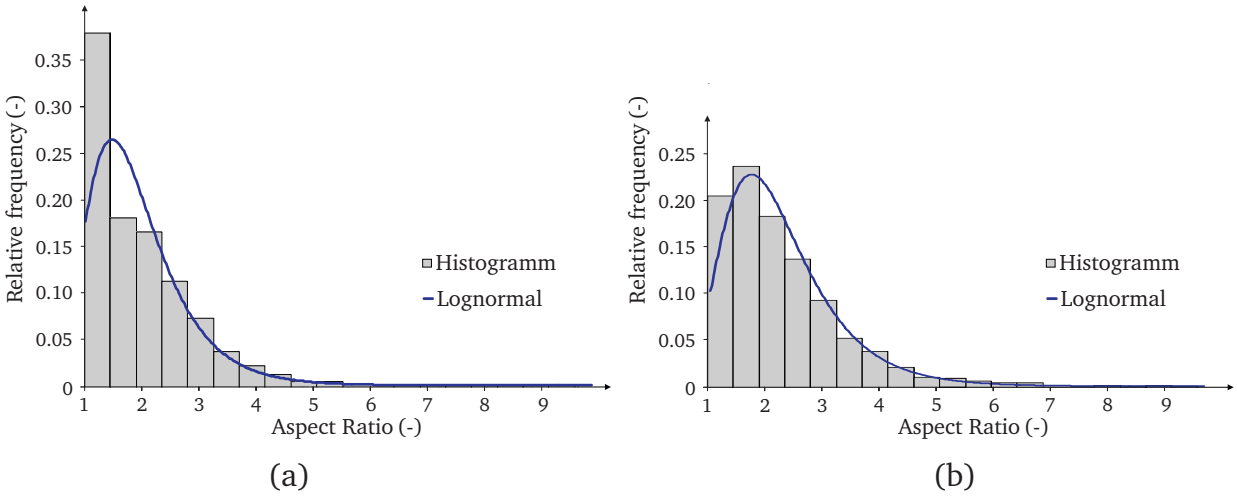

Figure 5.9: Comparison of experimentally observed aspect ratios in sample 2-01 (a) and simulated (b) aspect ratios. The difference is because the all observed pores with a volume ratio $V_{\mathrm{R}} < 1.91$ were counted as spherical pores with an axis ratio of 1.

histograms show significant differences for small aspect ratios. This is because experimentally determined volume ratios below $V_{\mathrm{R}} < 1.91$ were counted as spherical pores in the histogram shown in Figure 5.9 (a). As already mentioned above, a remedy for this mismatch would be to allow generalized ellipsoids.

Finally the spatial distributions of pores is accessed. Even though a spatial random distribution of pores is defined in the input parameters, all three models show a slight tendency towards an ordered distribution of the pores. There are two possible causes, firstly, the random number generation algorithm of Python could be flawed. Secondly,

the pores are placed sequentially within the volume element model and, by definition, need a minimum distance between the pores. This causes an increased limitation of possible locations to place pores with every further pore placed within the model. Naturally this influences the random distribution of points (pores).

The observations presented above allow some conclusions to be drawn with respect to the representation of the characteristic pore geometries by the presented modeling approach. In large, the geometrical characteristics of porous samples can be represented with a high accuracy by the proposed modeling approach. Care has to be taken when defining the input parameters for the model generation, especially defining the minimum and maximum thresholds for the pore size and pore shape distributions as well as the volume element size. An inapt definition of these parameters can cause serious errors in the statistical representation of the geometrical characteristics of a porous material. Finally, the proposed modeling approach is limited in the ability to represent the pore shapes, which should be improved in a future advancement of the modeling approach.

5.2.2 Mechanical Material Behavior

Within this chapter the mechanical material behavior of porous MAR-M247 nickel-base cast alloy as predicted by the numerical micromechanical volume element model as well as the results obtained by mechanical testing are discussed. After studying the effective elastic behavior of porous MAR-M247 cast samples, the offset yield stress is investigated by comparing the micromechanical model predictions to the mechanical tests preformed using the deformation dilatometer as explained in Chapter 3. The resulting offset yield stress obtained from the dilatometer experiments and those obtained form the simulation are compared in Figure 5.10. The models predict slightly to high offset yield stresses. A likely reason for the over-estimation of the offset yield stress by the volume element model is that only pores are considered in the microstructure. However, the real material is far more complex exhibiting other inclusions such as carbides within the microstructure, which also trigger stress concentrations, but are not considered in this modeling approach.

For the small scattering of the model results, this is seen as an indication for a sufficient size of the volume element model to obtain representative results.

However, more compression tests should be conducted to achieve a statistically relevant sample size.

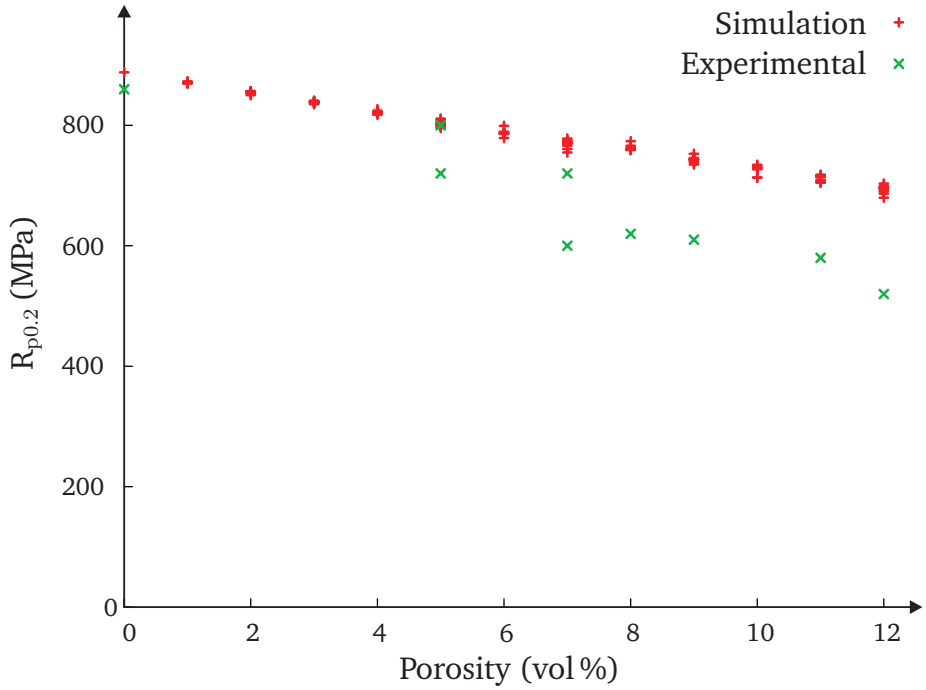

Figure 5.10: Comparison of simulated and experimentally determined offset yield stresses. The simulation seems to overestimate the offset yield stress.

5.3 Multiscale Modeling Results

5.3.1 Sequential Multiscale Modeling Results

As an example of a sequential multiscale model, a fictional component containing porous regions with the dimensions listed in Appendix C is analyzed. A three dimensional representation of the component is given in Figure 5.11. This component guides a fluid from a

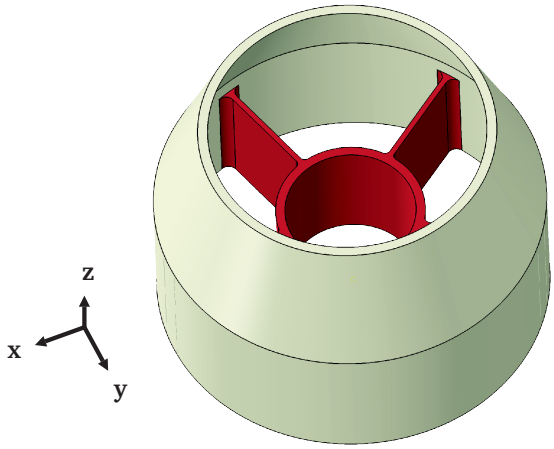

Figure 5.11: Part of the converging nozzle guiding a fluid from a high pressure to a low pressure reservoir. The grey area is assumed to be pore free (bulk) material, whereas the red region is assumed to be porous with a pore volume fraction of 8 %.

high pressured reservoir into a nozzle which is connected to a low pressure reservoir (cf. Figure 5.12). The relative pressure of the high pressure reservoir and the surrounding

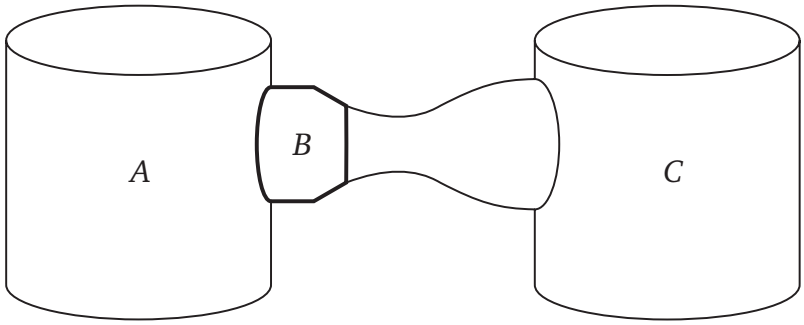

Figure 5.12: Schematic representation of the nozzle setup. The fluid is guided from a high pressure reservoir (*A*) to a low pressure reservoir (*C*). Part of the converging nozzle (*B*) is exposed to a pressure load resulting form the pressure difference of the ambient pressure and the pressure in the high pressure reservoir.

atmosphere is 10 bar, thus causing a pressure loading on the wall of the component. The component is clamped at the flange face (converging end).
In the first step, the stresses caused by the loading are evaluated based on an FEA neglecting any influence of the pores (see Figure 5.13 (a)). The obtained stress distribution is compared to the results from an analysis of the same structure using the sequential multiscale model and thus taking into account the influence of the pores on the constitutive behavior of the porous section (see Figure 5.13 (b)).
For the sequential multiscale analysis the component is partitioned into a porous section with a pore volume fraction of 8 % (red area in Figure 5.11; constitutive behavior is assigned according to the homogenized response of an RVE model) and a pore free section (grey area in Figure 5.11; constitutive behavior of the pore free material is assigned).
The results obtained from the conventional FEA and the sequential multiscale model have significantly different stress distributions (see Figure 5.13). The pores' influence on the constitutive behavior of the porous section leads to a decrease in its load-bearing capacity, which causes an increase of the stress level in certain pore free regions.
However, not only the stresses on the macroscopic level differ between the sequential multiscale model and the FEA neglecting the influence of the pores. The sequential multscale model also enables the investigation of stresses acting on the microscopic level. Therefore, the stress distribution within the porous region of the structure is studied (see Figure 5.14). As previously mentioned, in the sequential multiscale model the constitutive behavior of the porous region is assigned using a UMAT subroutine, which enables a logging of the deformation gradient tensor at every integration point (see Section 4.3.1). After the FEA of the component, the deformation gradient of any area of interest within the porous section can be extracted and used for a microscopic simulation. The de-

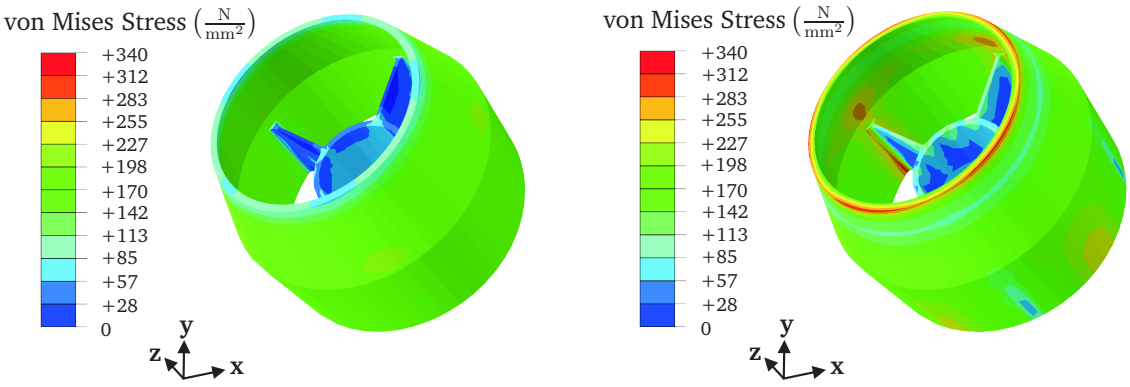

(a) (b)

Figure 5.13: Comparison of the stress distribution obtained from a conventional FEA (a) and from a sequential multiscale model (b). The influence of the pores lead to a redistribution of the stresses. The predicted stresses within the pore free region are considerably higher in the sequential multiscale model due to the decreased load-bearing of the porous structure (red area in Figure 5.11).

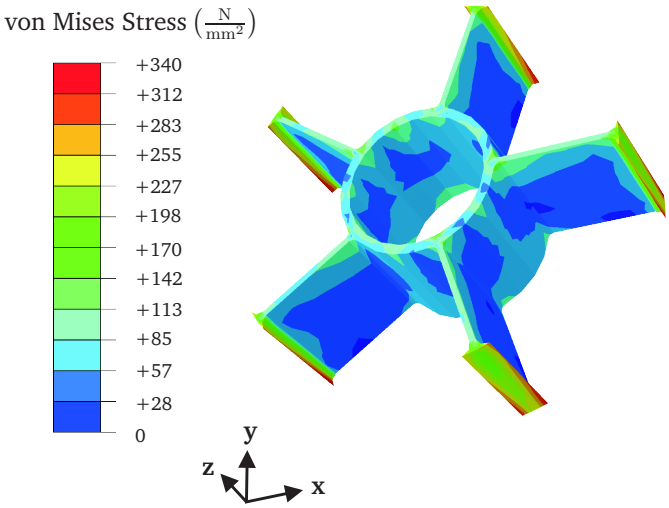

Figure 5.14: Stress distribution within the porous section of the converging nozzle structure. The deformation gradient is logged at each integration point via a UMAT subroutine (cf. Section 4.3.1). The deformation gradient of the highest stressed area is read-out and used for a subsequent computation of the stresses in the microstructure (see Figure 5.15).

formation gradient tensor of the highest stressed point within the porous section (see Figure 5.14) is extracted as

$$\mathbf{F} = \begin{bmatrix} 0.999467 & -0.000132 & -0.000560 \\ -0.001010 & 1.001701 & -0.000383 \\ 0.000660 & 0.000536 & 0.999724 \end{bmatrix} .$$

Using Equations (4.33) and (4.34) the symmetric displacement gradient tensor is derived from the displacement gradient tensor. The symmetric displacement gradient tensor is applied to a micromechanical volume element model representing the microstructure of the highest stressed point. The results obtained from the micromechanical simulation show that the stresses on the microstructural level (see Figure 5.15) are considerably higher than the stresses predicted on the component level (see Figure 5.14). The stress locally exceeds the yield stress of the bulk material of 800 $\frac{\mathrm{N}}{\mathrm{mm}^2}$.

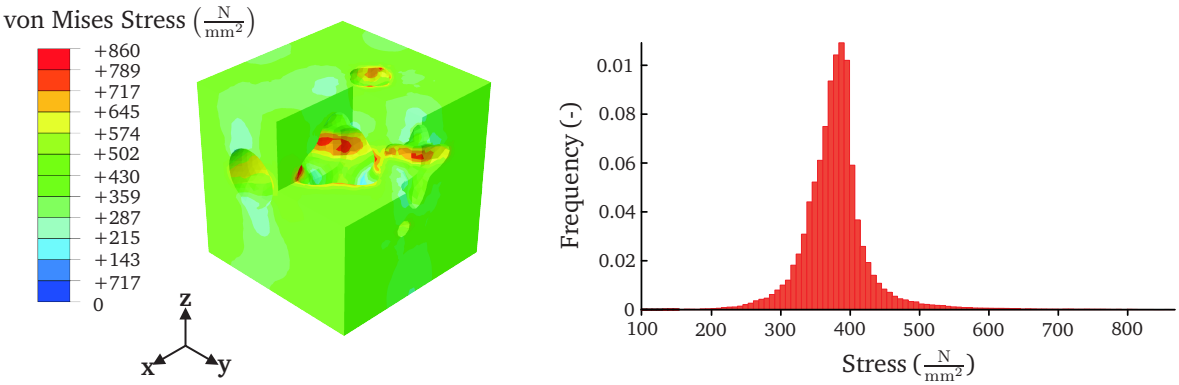

(a) (b)

Figure 5.15: Stress distribution in the microstructure. The RVE depicted in (a) is deformed according to the symmetric displacement gradient tensor of the highest stressed area within the porous region of the converging nozzle structure shown in Figure 5.14. The stresses present in the microstructure are considerably higher than those observed on the macroscopic level. A histogram of the stress distribution within the RVE is depicted in (b).

Based on the results obtained from the sequential multiscale model, the component geometry can be optimized. The presented example clearly demonstrates the importance of taking the microstructural influence into account. Using the sequential multiscale model enables to improves the accuracy of the macroscopic stress prediction and to evaluate the stresses on the microstructural level at a moderate increase of the computational expense. However, it is not feasible for nonlinear loading paths.

5.3.2 Concurrent Multiscale Modeling Results

In order to validate the results obtained by the concurrent multiscale approach a simple uniaxial deformation test is preformed on a cube. The stress response obtained by the concurrent multiscale approach is compared to the result from a conventional FE model. The constitutive law is assumed as bilinear elastic-plastic, which is schematically depicted in Figure 5.17 (b).

On the macroscopic level, the multiscale model consists of one reduced integrated linear brick element (C3D8R). The applied boundary conditions (see Figure 5.16) constitute displacements prescribed on the vertex nodes of the brick element which cause a uniaxial strain of 0.5 % in **x** direction. The microscale model which is coupled to the macroscopic

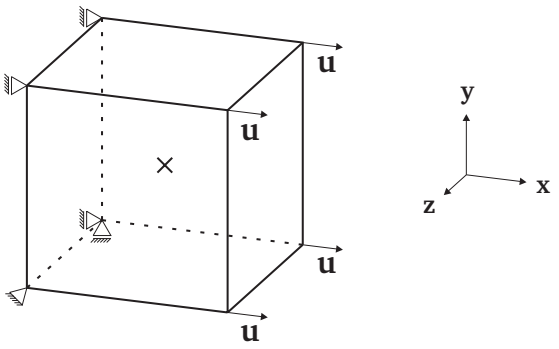

Figure 5.16: Macroscopic element with defined boundary conditions on the nodes. The boundary conditions constitute a uniaxial deformation.

integration point as depicted in Figure 5.17 (a) comprises 1000 fully integrated linear brick elements (C3D8) [68] with prescribed periodic boundary conditions.
Even though the load case is seemingly trivial it is of fundamental importance in order to validate the accuracy of the implemented concurrent multiscale computation scheme. A comparison of the results gained by the multiscale model and the conventional FE model is presented in Figure 5.17 (d). Due to the trivial load case it is sufficient for the conventional FE model to contain only one reduced integrated 8-node linear brick (C3D8R) [68] element. The results show that the concurrent multiscale model provides the same quantitative values of the von Mises stress as the conventional FE model which is depicted in Figure 4.19 (d).
The wall clock time recorded in the data (*.dat) file allows to compare the computational cost of the two modeling approaches. The direct solver of Abaqus/Standard is used for both the conventional and the concurrent multiscale model. The simulations are run using an Intel Xeon X5550 CPU with a clock speed of 2.66GHz on a system with 12 GB RAM. The wall clock time for the concurrent multiscale model is recorded with 381 seconds. By comparison, the wall clock time of the conventional FE model is 1 second. The difference in the wall clock times demonstrates the computational cost of concurrent multiscale simulations. However, it should be noted that the computation time strongly depends on the model at hand and the computer hardware. Thus the comparison of the concurrent multiscale and the conventional FE model only shows a trend and is not directly scalable to other problems.
Nevertheless, a major advantage of the multiscale scheme is, that it offers the possibility to obtain additional information about stress and strain quantities within the microstruc-

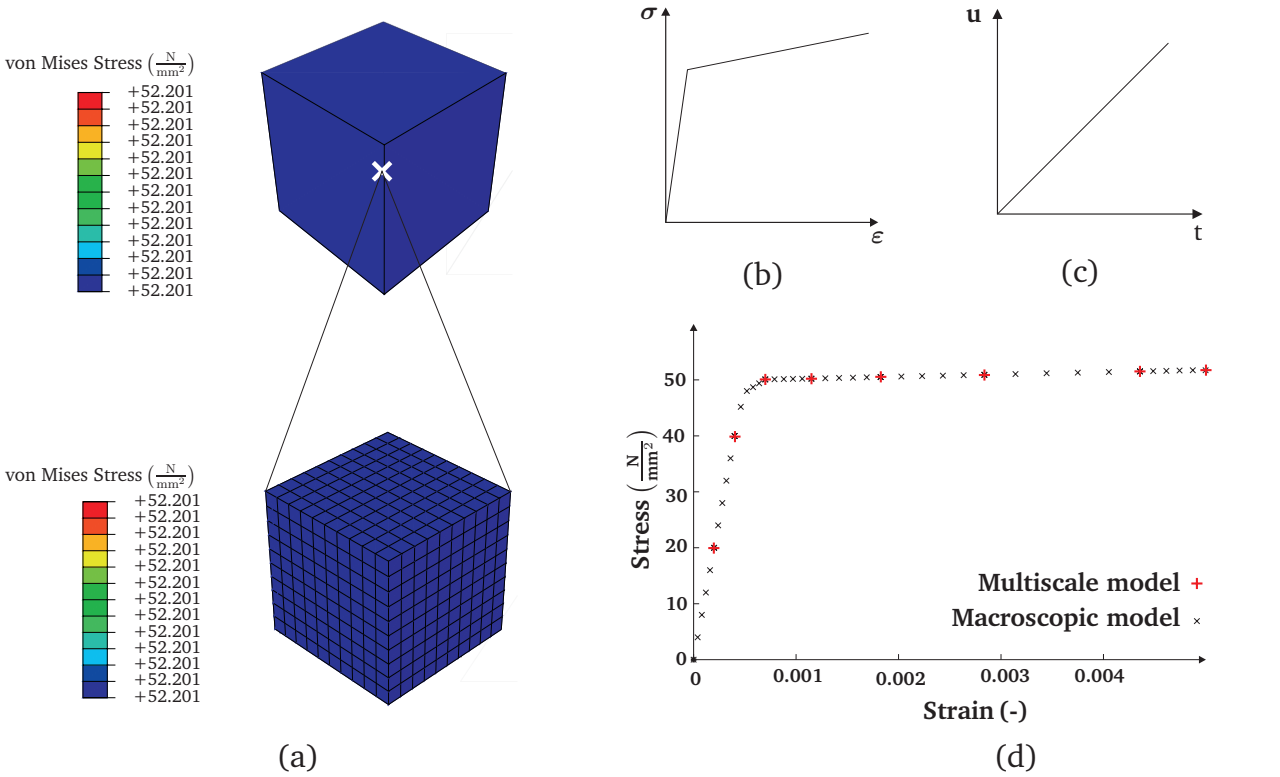

Figure 5.17: Model assumptions for the verification of the concurrent multiscale model. (a) Concurrent multiscale model comprising the macroscopic reduced integrated brick element and the micromechanical volume element coupled to the integration point of the macroscopic element. The von Mises Stress in is depicted for both microscopic and macroscopic models at the end of the deformation. (b) Schematic representation of the bilinear elasto-plastic constitutive model. (c) The displacement of the vertex nodes is linearly ramped. (d) The resulting stress strain curve from the concurrent multiscale model (x) compared to results obtained form a purely macroscopic model (+).

ture. Furthermore the macroscopic stress and strain distributions are based on the underlying microstructure and thus are more accurate compared to the conventional FE approach. This bears the potential to optimize the design of components with respect to the materials' microstructure and the local loading conditions.

The evaluation of the macroscopic stress distribution as well as the ability to evaluate microscopic quantities are demonstrated by the concurrent multiscale model of a beam presented in the following. The beam is clamped at one end whereas the tip is deflected by 1 % of the beam length (cf. Figure 5.18). The beam is supposed to have a pore volume fraction of 2 % at its bearing point. The pore volume fraction is linearly increased over its length to a pore volume fraction of 8 % at the tip of the beam. The macroscopic stress distribution of a deflected beam exhibiting a varying pore volume fraction over its length as predicted by the concurrent multiscale computation is presented in Figure 5.19. The stress distribution of a conventional FE model of the beam without considering any pores

Figure 5.18: Boundary and loading conditions of the beam model. The beam is clamped at its bearing point, where the tip of the beam is displaced by 1 % of the beam length.

is presented in Figure 5.20. The multiscale model predicts a 4.2% lower von Mises stress which can be understood considering that by accounting for porosity some material is removed from the beam. Thus for displacement controlled loading the homogenized stress must be lower compared to the model without considering any porosity. Furthermore the stress distribution of two attached microstructure models are presented in Figure 5.19. The concurrent multiscale beam model contains four fully integrated linear brick elements (C3D8) on the macroscale. A micromechanical model is linked to each of the 32 integration points. The micromechanical models contain between 36343 and 71820 linear tetrahedral elements (C3D4). The wall clock time to complete this simulation is 135221 seconds or 37 hours and 34 minutes. This again demonstrates the immense computational cost of the multiscale computation scheme. An application of the introduced concurrent multiscale framework for the layout of industrial components is not economically profitable at present. Nevertheless it shows the potential to improve component layout processes and resource management in the future.

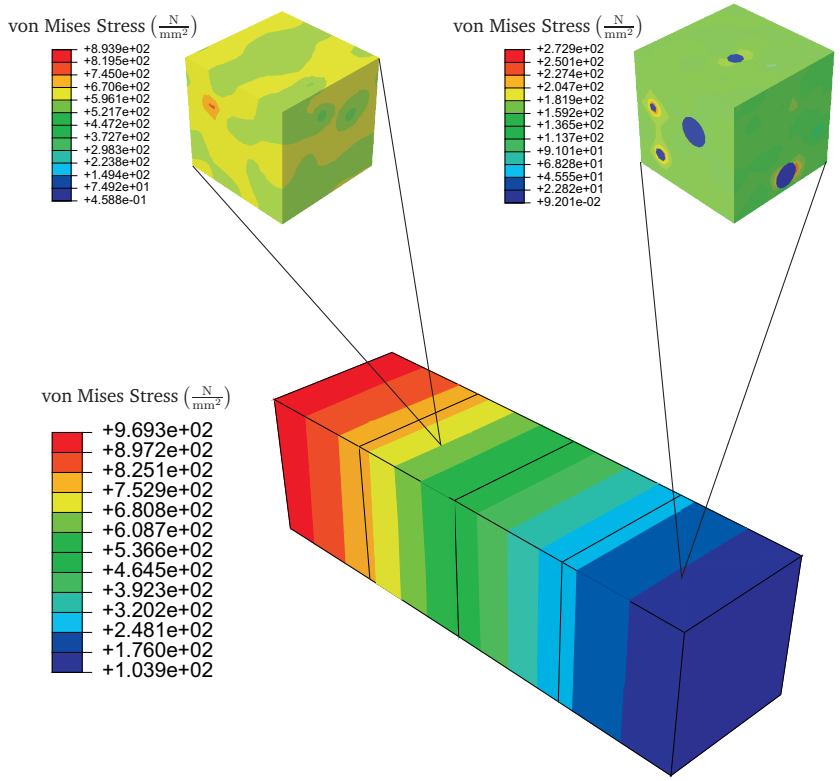

Figure 5.19: Working example of the multiscale approach. The pore volume fraction varies along the beam. Two exemplary underlying microstructures are depicted. The field plots represent the macroscopic and the microscopic stress distributions.

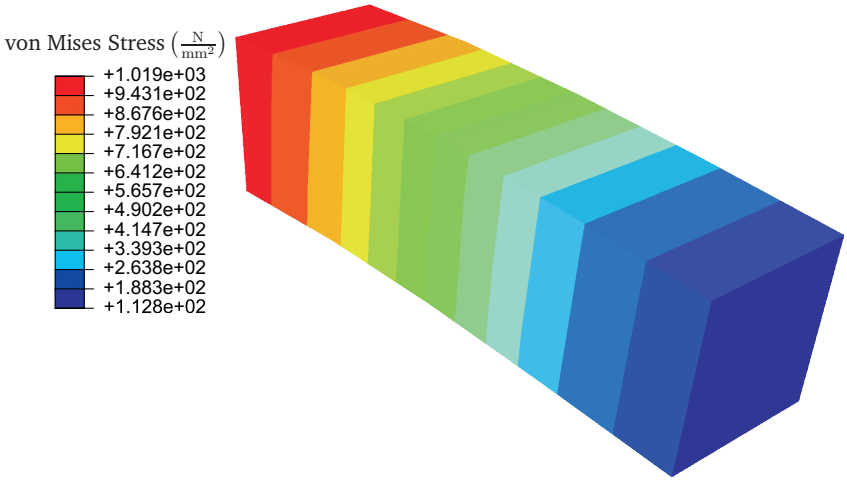

Figure 5.20: Predicted stress distribution obtained from a macroscopic FE model of the deflected beam. The constitutive law is equivalent to the one used for the metal matrix in the multiscale computation (cf. Figure 5.19).

Chapter 6

Conclusions and Outlook

6.1 Conclusions

A micromechancal finite element model to study the influence of pores on the material behavior has been presented within this work. The assumptions for the computer generated modeling approach are based on experimental evaluations of porous MAR-M247 cast samples. The results gained by experimental and computational investigations of porous MAR-M247 samples led to seven important conclusions.

1. The analysis of the CT data shows that the volume distribution of pores is accurately represented by a Lognormal distribution. Attention has to be paid to the threshold for minimum and maximum pore size. These thresholds are strongly depending on the available experimental data, the aim of the model and engineering considerations as e.g. rejection limits. The assumptions used within this work are not universally valid.

2. A spatially random pore distribution is found to be a good approximation for low and medium pore volume fractions ($<$13 %) within the MAR-M247 cast samples. For larger pore volume fraction the assumption of individual, non-intersecting pores looses its validity.

3. The size of the modeled volume element has to be sufficiently large - *representative* - to obtain reliable results. To ensure converged results for low to medium pore volume fractions ($<$13 %) the minimum volume element size is found to be $200\times200\times200$ μm^3. Obviously applying the model to different materials necessitates a reevaluation of the convergency.

4. Attention has to be paid when defining the input parameters for the model volume element generation. As shown in the convergence study of the mechanical behavior

as well as in the statistical evaluation of the geometry parameters, a set of flawed input parameters can cause inadequate results. Thus, the convergence behavior should always be critically assessed before an interpretation and further usage of the results.

5. The results gained by the modeling approach regarding the linear elastic materials behavior supports the analytical solution provided by the Hashin Strickman upper bounds. The main difference between the assumptions made by Hashin and Strickman and the modeling approach presented within this work is the shape of the pores. Since the results from the FE model and the analytical solution coincide we can conclude that the pore shape does not have a significant influence on the elastic materials behavior.

6. The simulations show that pores trigger stress concentrations within the material. Plastification starts in the vicinity of pores. The onset of plastification is governed by the pore volume fraction as well as the pore shape. Plastification starts at a macroscopic load level well below the offset yield stress. Thus pores do influence the offset yield stress and provide a potential site for the initiation of cracks.

7. The sequential multiscale model provides a straight forward method to transfer the results obtained at the microscopic scale to the macroscopic scale. However, the sequential multiscale model is not able to account for nonlinear load path dependencies of the material behavior. To overcome this limitation so-called concurrent multiscale models have to be applied. The basic applicability of such an approach is demonstrated within this work, however, the efficiency of the concurrent multiscale model needs to be improved to enable an application on an industrial scale.

6.2 Outlook

There are several limitations in the experimental investigations of the porous samples. First, the number of samples that were available to base the experimental analysis of the pore characteristics on is very small. Investigating a larger number of samples would help to validate and refine the linear regression of the parameters for the Lognormal distribution of the pore volumes.
Within this work the spatial pore distribution is evaluated based on the centroid coordinates of the pores. However, since the shape of the pores is complex, the distance of the centroids of the pores is just an estimate for the nearest neighbor distance. To improve the evaluation of the nearest neighbor distance, the post processing script for the CT data should be adapted such that the actual minimum distance between two pores

can be evaluated. Considering the actual nearest neighbor distance of pores in the micromechanical model is expected to increase the accuracy of the modeling results, since the minimum distance between two pores does influence the development of stress and strain fields between two pores.
Another area of major interest, which is not tackled within this work is the establishment of a phenomenological fracture criterion. To derive such a criterion tensile tests are necessary, however casting porous tensile specimens is a very difficult matter, which was not part of this project. Nevertheless the micromechanical FE model presented within this work is designed such that a phenomenological fracture criterion based on quantile evaluation of stress or strain fields can be easily implemented.
Regarding the FE approach presented within this work, there are two main areas of interest. Firstly, for the micromechanical FE model of porous materials, more general pore shapes should be implemented. This of course has to be accompanied by more sophisticated experimental evaluations of the pore shape e.g. evaluating local and global curvatures of the pores within the matrix material. Secondly, focus should be directed towards improving the presented concurrent multiscale approach. The concurrent multiscale framework implemented in the course of this project is a first step to directly linking the microscopic to the macroscopic scale in modern component layout. On the one hand the validation and the minimal working example presented in Chapter 5.3 proofs the basic functionality of the concurrent multiscale approach. The immense computational cost on the other hand demonstrates that it is currently not applicable for real world component layouts. However, to optimize the component layout of components the consideration of microstructural features bears a huge potential for the future. The development and implementation of efficient concurrent multiscale frameworks is definitely the most exciting area of research in terms of its potential to improve future component layouts. The multiscale approaches will gain in importance and are vital in order to link microstructural volume element models and macroscopic component layout.

Appendix A

Computation of Numerical Tangent

Expanded version of Equation (4.37). The given linear equation system can be solved to obtain the sought after components of the tangential stiffness tensor **C**.

$$
\begin{bmatrix}
{}^{1}\varepsilon_{11} & {}^{1}\varepsilon_{22} & {}^{1}\varepsilon_{33} & {}^{1}\varepsilon_{12} & {}^{1}\varepsilon_{13} & {}^{1}\varepsilon_{23} & 0 & 0 & 0 & 0 & 0 & 0 & 0 & 0 & 0 & 0 & 0 & 0 & 0 & 0 & 0 \\
0 & {}^{1}\varepsilon_{11} & 0 & 0 & 0 & 0 & {}^{1}\varepsilon_{22} & {}^{1}\varepsilon_{33} & {}^{1}\varepsilon_{12} & {}^{1}\varepsilon_{13} & {}^{1}\varepsilon_{23} & 0 & 0 & 0 & 0 & 0 & 0 & 0 & 0 & 0 & 0 \\
0 & 0 & {}^{1}\varepsilon_{11} & 0 & 0 & 0 & 0 & {}^{1}\varepsilon_{22} & 0 & 0 & 0 & {}^{1}\varepsilon_{33} & {}^{1}\varepsilon_{12} & {}^{1}\varepsilon_{13} & {}^{1}\varepsilon_{23} & 0 & 0 & 0 & 0 & 0 & 0 \\
0 & 0 & 0 & {}^{1}\varepsilon_{11} & 0 & 0 & 0 & 0 & {}^{1}\varepsilon_{22} & 0 & 0 & 0 & {}^{1}\varepsilon_{33} & 0 & 0 & {}^{1}\varepsilon_{12} & {}^{1}\varepsilon_{13} & {}^{1}\varepsilon_{23} & 0 & 0 & 0 \\
0 & 0 & 0 & 0 & {}^{1}\varepsilon_{11} & 0 & 0 & 0 & 0 & {}^{1}\varepsilon_{22} & 0 & 0 & 0 & {}^{1}\varepsilon_{33} & 0 & 0 & {}^{1}\varepsilon_{12} & 0 & {}^{1}\varepsilon_{13} & {}^{1}\varepsilon_{23} & 0 \\
0 & 0 & 0 & 0 & 0 & {}^{1}\varepsilon_{11} & 0 & 0 & 0 & 0 & {}^{1}\varepsilon_{22} & 0 & 0 & 0 & {}^{1}\varepsilon_{33} & 0 & 0 & {}^{1}\varepsilon_{12} & 0 & {}^{1}\varepsilon_{13} & {}^{1}\varepsilon_{23} \\
{}^{2}\varepsilon_{11} & {}^{2}\varepsilon_{22} & {}^{2}\varepsilon_{33} & {}^{2}\varepsilon_{12} & {}^{1}\varepsilon_{13} & {}^{2}\varepsilon_{23} & 0 & 0 & 0 & 0 & 0 & 0 & 0 & 0 & 0 & 0 & 0 & 0 & 0 & 0 & 0 \\
0 & {}^{2}\varepsilon_{11} & 0 & 0 & 0 & 0 & {}^{2}\varepsilon_{22} & {}^{2}\varepsilon_{33} & {}^{2}\varepsilon_{12} & {}^{1}\varepsilon_{13} & {}^{2}\varepsilon_{23} & 0 & 0 & 0 & 0 & 0 & 0 & 0 & 0 & 0 & 0 \\
0 & 0 & {}^{2}\varepsilon_{11} & 0 & 0 & 0 & 0 & {}^{2}\varepsilon_{22} & 0 & 0 & 0 & {}^{2}\varepsilon_{33} & {}^{2}\varepsilon_{12} & {}^{1}\varepsilon_{13} & {}^{2}\varepsilon_{23} & 0 & 0 & 0 & 0 & 0 & 0 \\
0 & 0 & 0 & {}^{2}\varepsilon_{11} & 0 & 0 & 0 & 0 & {}^{2}\varepsilon_{22} & 0 & 0 & 0 & {}^{2}\varepsilon_{33} & 0 & 0 & {}^{2}\varepsilon_{12} & {}^{2}\varepsilon_{13} & {}^{2}\varepsilon_{23} & 0 & 0 & 0 \\
0 & 0 & 0 & 0 & {}^{2}\varepsilon_{11} & 0 & 0 & 0 & 0 & {}^{2}\varepsilon_{22} & 0 & 0 & 0 & {}^{2}\varepsilon_{33} & 0 & 0 & {}^{2}\varepsilon_{12} & 0 & {}^{2}\varepsilon_{13} & {}^{2}\varepsilon_{23} & 0 \\
0 & 0 & 0 & 0 & 0 & {}^{2}\varepsilon_{11} & 0 & 0 & 0 & 0 & {}^{2}\varepsilon_{22} & 0 & 0 & 0 & {}^{2}\varepsilon_{33} & 0 & 0 & {}^{2}\varepsilon_{12} & 0 & {}^{2}\varepsilon_{13} & {}^{2}\varepsilon_{23} \\
{}^{3}\varepsilon_{11} & {}^{3}\varepsilon_{22} & {}^{3}\varepsilon_{33} & {}^{3}\varepsilon_{12} & {}^{1}\varepsilon_{13} & {}^{3}\varepsilon_{23} & 0 & 0 & 0 & 0 & 0 & 0 & 0 & 0 & 0 & 0 & 0 & 0 & 0 & 0 & 0 \\
0 & {}^{3}\varepsilon_{11} & 0 & 0 & 0 & 0 & {}^{3}\varepsilon_{22} & {}^{3}\varepsilon_{33} & {}^{3}\varepsilon_{12} & {}^{1}\varepsilon_{13} & {}^{3}\varepsilon_{23} & 0 & 0 & 0 & 0 & 0 & 0 & 0 & 0 & 0 & 0 \\
0 & 0 & {}^{3}\varepsilon_{11} & 0 & 0 & 0 & 0 & {}^{3}\varepsilon_{22} & 0 & 0 & 0 & {}^{3}\varepsilon_{33} & {}^{3}\varepsilon_{12} & {}^{1}\varepsilon_{13} & {}^{3}\varepsilon_{23} & 0 & 0 & 0 & 0 & 0 & 0 \\
0 & 0 & 0 & {}^{3}\varepsilon_{11} & 0 & 0 & 0 & 0 & {}^{3}\varepsilon_{22} & 0 & 0 & 0 & {}^{3}\varepsilon_{33} & 0 & 0 & {}^{3}\varepsilon_{12} & {}^{3}\varepsilon_{13} & {}^{3}\varepsilon_{23} & 0 & 0 & 0 \\
0 & 0 & 0 & 0 & {}^{3}\varepsilon_{11} & 0 & 0 & 0 & 0 & {}^{3}\varepsilon_{22} & 0 & 0 & 0 & {}^{3}\varepsilon_{33} & 0 & 0 & {}^{3}\varepsilon_{12} & 0 & {}^{3}\varepsilon_{13} & {}^{3}\varepsilon_{23} & 0 \\
0 & 0 & 0 & 0 & 0 & {}^{3}\varepsilon_{11} & 0 & 0 & 0 & 0 & {}^{3}\varepsilon_{22} & 0 & 0 & 0 & {}^{3}\varepsilon_{33} & 0 & 0 & {}^{3}\varepsilon_{12} & 0 & {}^{3}\varepsilon_{13} & {}^{3}\varepsilon_{23} \\
{}^{4}\varepsilon_{11} & {}^{4}\varepsilon_{22} & {}^{4}\varepsilon_{33} & {}^{4}\varepsilon_{12} & {}^{1}\varepsilon_{13} & {}^{4}\varepsilon_{23} & 0 & 0 & 0 & 0 & 0 & 0 & 0 & 0 & 0 & 0 & 0 & 0 & 0 & 0 & 0 \\
0 & {}^{4}\varepsilon_{11} & 0 & 0 & 0 & 0 & {}^{4}\varepsilon_{22} & {}^{4}\varepsilon_{33} & {}^{4}\varepsilon_{12} & {}^{1}\varepsilon_{13} & {}^{4}\varepsilon_{23} & 0 & 0 & 0 & 0 & 0 & 0 & 0 & 0 & 0 & 0 \\
0 & 0 & {}^{4}\varepsilon_{11} & 0 & 0 & 0 & 0 & {}^{4}\varepsilon_{22} & 0 & 0 & 0 & {}^{4}\varepsilon_{33} & {}^{4}\varepsilon_{12} & {}^{1}\varepsilon_{13} & {}^{4}\varepsilon_{23} & 0 & 0 & 0 & 0 & 0 & 0 \\
0 & 0 & 0 & {}^{4}\varepsilon_{11} & 0 & 0 & 0 & 0 & {}^{4}\varepsilon_{22} & 0 & 0 & 0 & {}^{4}\varepsilon_{33} & 0 & 0 & {}^{4}\varepsilon_{12} & {}^{4}\varepsilon_{13} & {}^{4}\varepsilon_{23} & 0 & 0 & 0 \\
0 & 0 & 0 & 0 & {}^{4}\varepsilon_{11} & 0 & 0 & 0 & 0 & {}^{4}\varepsilon_{22} & 0 & 0 & 0 & {}^{4}\varepsilon_{33} & 0 & 0 & {}^{4}\varepsilon_{12} & 0 & {}^{4}\varepsilon_{13} & {}^{4}\varepsilon_{23} & 0 \\
0 & 0 & 0 & 0 & 0 & {}^{4}\varepsilon_{11} & 0 & 0 & 0 & 0 & {}^{4}\varepsilon_{22} & 0 & 0 & 0 & {}^{4}\varepsilon_{33} & 0 & 0 & {}^{4}\varepsilon_{12} & 0 & {}^{4}\varepsilon_{13} & {}^{4}\varepsilon_{23} \\
{}^{5}\varepsilon_{11} & {}^{5}\varepsilon_{22} & {}^{5}\varepsilon_{33} & {}^{5}\varepsilon_{12} & {}^{1}\varepsilon_{13} & {}^{5}\varepsilon_{23} & 0 & 0 & 0 & 0 & 0 & 0 & 0 & 0 & 0 & 0 & 0 & 0 & 0 & 0 & 0 \\
0 & {}^{5}\varepsilon_{11} & 0 & 0 & 0 & 0 & {}^{5}\varepsilon_{22} & {}^{5}\varepsilon_{33} & {}^{5}\varepsilon_{12} & {}^{1}\varepsilon_{13} & {}^{5}\varepsilon_{23} & 0 & 0 & 0 & 0 & 0 & 0 & 0 & 0 & 0 & 0 \\
0 & 0 & {}^{5}\varepsilon_{11} & 0 & 0 & 0 & 0 & {}^{5}\varepsilon_{22} & 0 & 0 & 0 & {}^{5}\varepsilon_{33} & {}^{5}\varepsilon_{12} & {}^{1}\varepsilon_{13} & {}^{5}\varepsilon_{23} & 0 & 0 & 0 & 0 & 0 & 0 \\
0 & 0 & 0 & {}^{5}\varepsilon_{11} & 0 & 0 & 0 & 0 & {}^{5}\varepsilon_{22} & 0 & 0 & 0 & {}^{5}\varepsilon_{33} & 0 & 0 & {}^{5}\varepsilon_{12} & {}^{5}\varepsilon_{13} & {}^{5}\varepsilon_{23} & 0 & 0 & 0 \\
0 & 0 & 0 & 0 & {}^{5}\varepsilon_{11} & 0 & 0 & 0 & 0 & {}^{5}\varepsilon_{22} & 0 & 0 & 0 & {}^{5}\varepsilon_{33} & 0 & 0 & {}^{5}\varepsilon_{12} & 0 & {}^{5}\varepsilon_{13} & {}^{5}\varepsilon_{23} & 0 \\
0 & 0 & 0 & 0 & 0 & {}^{5}\varepsilon_{11} & 0 & 0 & 0 & 0 & {}^{5}\varepsilon_{22} & 0 & 0 & 0 & {}^{5}\varepsilon_{33} & 0 & 0 & {}^{5}\varepsilon_{12} & 0 & {}^{5}\varepsilon_{13} & {}^{5}\varepsilon_{23} \\
{}^{6}\varepsilon_{11} & {}^{6}\varepsilon_{22} & {}^{6}\varepsilon_{33} & {}^{6}\varepsilon_{12} & {}^{1}\varepsilon_{13} & {}^{6}\varepsilon_{23} & 0 & 0 & 0 & 0 & 0 & 0 & 0 & 0 & 0 & 0 & 0 & 0 & 0 & 0 & 0 \\
0 & {}^{6}\varepsilon_{11} & 0 & 0 & 0 & 0 & {}^{6}\varepsilon_{22} & {}^{6}\varepsilon_{33} & {}^{6}\varepsilon_{12} & {}^{1}\varepsilon_{13} & {}^{6}\varepsilon_{23} & 0 & 0 & 0 & 0 & 0 & 0 & 0 & 0 & 0 & 0 \\
0 & 0 & {}^{6}\varepsilon_{11} & 0 & 0 & 0 & 0 & {}^{6}\varepsilon_{22} & 0 & 0 & 0 & {}^{6}\varepsilon_{33} & {}^{6}\varepsilon_{12} & {}^{1}\varepsilon_{13} & {}^{6}\varepsilon_{23} & 0 & 0 & 0 & 0 & 0 & 0 \\
0 & 0 & 0 & {}^{6}\varepsilon_{11} & 0 & 0 & 0 & 0 & {}^{6}\varepsilon_{22} & 0 & 0 & 0 & {}^{6}\varepsilon_{33} & 0 & 0 & {}^{6}\varepsilon_{12} & {}^{6}\varepsilon_{13} & {}^{6}\varepsilon_{23} & 0 & 0 & 0 \\
0 & 0 & 0 & 0 & {}^{6}\varepsilon_{11} & 0 & 0 & 0 & 0 & {}^{6}\varepsilon_{22} & 0 & 0 & 0 & {}^{6}\varepsilon_{33} & 0 & 0 & {}^{6}\varepsilon_{12} & 0 & {}^{6}\varepsilon_{13} & {}^{6}\varepsilon_{23} & 0 \\
0 & 0 & 0 & 0 & 0 & {}^{6}\varepsilon_{11} & 0 & 0 & 0 & 0 & {}^{6}\varepsilon_{22} & 0 & 0 & 0 & {}^{6}\varepsilon_{33} & 0 & 0 & {}^{6}\varepsilon_{12} & 0 & {}^{6}\varepsilon_{13} & {}^{6}\varepsilon_{23}
\end{bmatrix}
\begin{bmatrix}
C_{11} \\ C_{12} \\ C_{13} \\ C_{14} \\ C_{15} \\ C_{16} \\ C_{22} \\ C_{23} \\ C_{24} \\ C_{25} \\ C_{26} \\ C_{33} \\ C_{34} \\ C_{35} \\ C_{36} \\ C_{44} \\ C_{45} \\ C_{46} \\ C_{55} \\ C_{56} \\ C_{66}
\end{bmatrix}
=
\begin{bmatrix}
{}^{1}\sigma_{11} \\ {}^{1}\sigma_{22} \\ {}^{1}\sigma_{33} \\ {}^{1}\sigma_{12} \\ {}^{1}\sigma_{13} \\ {}^{1}\sigma_{23} \\ {}^{2}\sigma_{11} \\ {}^{2}\sigma_{22} \\ {}^{2}\sigma_{33} \\ {}^{2}\sigma_{12} \\ {}^{2}\sigma_{13} \\ {}^{2}\sigma_{23} \\ {}^{3}\sigma_{11} \\ {}^{3}\sigma_{22} \\ {}^{3}\sigma_{33} \\ {}^{3}\sigma_{12} \\ {}^{3}\sigma_{13} \\ {}^{3}\sigma_{23} \\ {}^{4}\sigma_{11} \\ {}^{4}\sigma_{22} \\ {}^{4}\sigma_{33} \\ {}^{4}\sigma_{12} \\ {}^{4}\sigma_{13} \\ {}^{4}\sigma_{23} \\ {}^{5}\sigma_{11} \\ {}^{5}\sigma_{22} \\ {}^{5}\sigma_{33} \\ {}^{5}\sigma_{12} \\ {}^{5}\sigma_{13} \\ {}^{5}\sigma_{23} \\ {}^{6}\sigma_{11} \\ {}^{6}\sigma_{22} \\ {}^{6}\sigma_{33} \\ {}^{6}\sigma_{12} \\ {}^{6}\sigma_{13} \\ {}^{6}\sigma_{23}
\end{bmatrix}
$$

Appendix B

Initialization of the Concurrent Multiscale Model

The macroscopic model intended for a multiscale computation is conventionally set up using Abaqus/CAE. The macroscopic part geometry can be meshed using any predefined solid elements provided by the Abaqus element library. Since the constitutive behavior on the macroscopic scale is provided by micromechanical models, a *User Material* is defined to incorporate the UMAT subroutine. The UMAT is used to control the link between the macroscopic and microscopic models. Next the load steps are defined in the step module and the desired field output and history output variables are specified. To complete the model definition in Abaqus/CAE, Dirichlet type boundary conditions[1] are applied.
The local variation of microstructural parameters of the macroscopic component is governed by solution-dependent state variables (SDVs). These are defined by the SDVINI subroutine. As an example a cantilever of 35 mm length exhibiting a locally differing pore volume fraction is considered. The pore volume fraction should be 2.0% at the root and 8.0% at the tip of the cantilever. Thus a function in the form

```
STATEV(1)=2.D0+(COORDS(1)/35.D0)*6.D0
```

using the X coordinate of the cantilever is implemented resulting in a state variable field as depicted in Figure B.1. Naturally the definition of multiple SDVs in the macroscopic model allows to control further micromechanical quantities as for example the pore volume distribution, the spatial distribution of the pores and the aspect ratio of the pores represented in the micromechanical volume element models. Caution has to be paid when defining these variables since different SDV names are reserved for certain microstructural parameters as given in Table B.1. For the variation of any further variables which are not listed in Table B.1 the source code has to be adopted. Each SDV defined

[1] The implementation of the multiscale framework is restricted to Dirichlet type boundary conditions

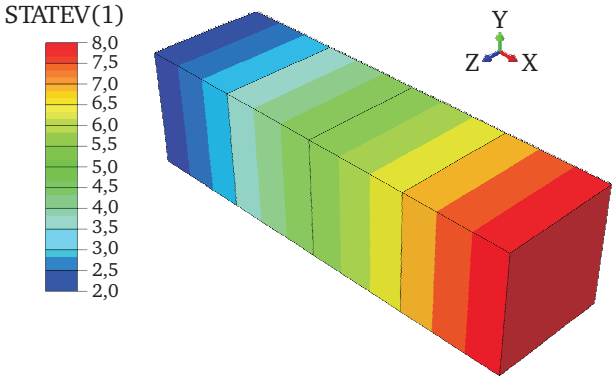

Figure B.1: State variable depending on x position of the cantilever.

Table B.1: Default micromechancial geometry parameters.

Parameter	Default value	Corresponding SDV name
Aspect ratio of pores	1	SDV1
Pore volume fraction	0	SDV2
Clustering in X, Y and Z direction	off	SDV3 - SDV6
Pore volume distribution algorithm	Lognormal*)	
Minimum and maximum pore volume	0.001-0.005	SDV8 & SDV9

*) Change of pore volume distribution algorithm is not supported

by the user requires the allocation of memory. The memory allocation is ensured by inserting

```
*DEPVAR
1
```

into the Abaqus input file using the Keyword editor tool. The integer in the second line indicates the number of state variables that are defined. After the state variables are defined, and the memory is allocated a job is created in Abaqus/CAE and the input file is written.

Appendix C

Draft of Converging Nozzle

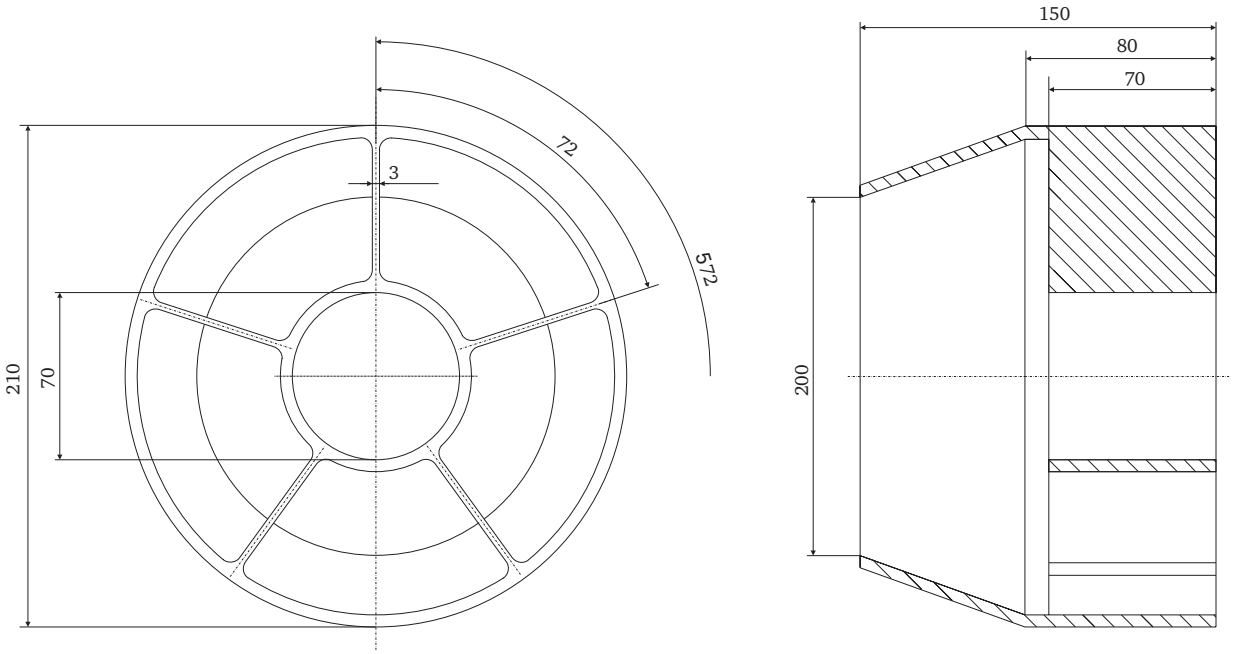

Figure C.1: Draft of the nozzle structure. All non dimensioned cast radii are 5 mm.

Bibliography

[1] Bräunling W.J.G. *Flugzeugtriebwerke – Grundlagen, Aero Thermodynamik, Kreisprozesse, Thermische Turbomaschinen, Komponenten und Emissionen*. Springer Verlag, 2009.

[2] Jones S. and Yuan C. Advances in shell moulding for investment casting. *Journal of Materials Processing Technology*, 135:258–265, 2003.

[3] Campbell J. *Castings*. Reed International Books, 1991.

[4] Sigloch H. *Strömungsmaschinen – Grundlagen und Anwendungen*. Carl Hanser Verlag München Wien, 1993.

[5] Reed R. *The superalloys, fundamentals and application*. Cambridge University Press, 2006.

[6] Smarsly W. Triebwerkswerkstoffe – Quo vadis. Technical report, MTU Aero Engines GmbH, 2008.

[7] Kouznetsova V. *Computational homogenization for the multi-scale analysis of mulitphase materials*. PhD thesis, Technische Universität Eindhoven, 2002.

[8] Ohser J. and Mücklich F. *Statistical analysis of microstructures in materials science*. John Wiley & Sons Ltd., 2000.

[9] Dunne F.P.E., Grant P.S., Peng H.X., and Cantor B. Dynamic densification of metal matrix-coated fibre composites: Modelling and processing. *Acta Materialia*, 53:617–628, 2005.

[10] Voigt W. Über die Beziehung Zwischen den Beiden Elastizitätskonstanten Isotroper Körper. *Annals of Physics*, 38:573–587, 1889.

[11] Reuss A. Berechnung der Fließgrenze von Mischkristallen auf Grund der Plastizitätsbedingung für Einkristalle. *Zeitschrift für Angewandte Mathematik und Mechanik*, 9:49–58, 1929.

[12] Eshelby J.D. The determination of the elastic field of an ellipsoidal inclusion and related problems. *Proceeding of the Royal Society A*, 241:376–396, 1957.

[13] Hashin Z. and Shtrikman S. A variational approach to the theory of the elastic behavior of multiphase materials. *Journal of Applied Mechanics*, 11:127–140, 1963.

[14] Patscheider J. Implementierung Analytischer und Finite Element Basierter Homogenisierungsverfahren zur Charakterisierung Heterogener Werkstoffe. Technical report, Lehrstuhl für Werkstoffkunde und Werkstoffmechanik, 2010.

[15] Mori T. and Tanaka K. Average stress in the matrix and average elastic energy of materials with misfitting inclusions. *Acta Metallurgica*, 21:571–574, 1973.

[16] Hill R. A self consistent mechanics of composite materials. *Journal of the Mechanics and Physics of Solids*, 13:213–222, 1965.

[17] Nement-Nassar S. and Hori M. *Micromechanics: Overall properties of heterogenous materials*. Elsevier Ltd, 1993.

[18] Nakamura T. and Suresh S. Effects of thermal residual stresses and fiber packing on defomration of metal-matrix composites. *Acta Metallurgica et Materialia*, 41:1665–1681, 1993.

[19] van der Sluis O., Schreurs P.J.G., Brekelmans W.A.M., and Meijer H.E.H. Overall behaviour of heterogeneous elastoviscoplastic materials: Effect of microsstructural modelling. *Mechanics of Materials*, 32:449–462, 2000.

[20] Werner E., Siegmund T., Weinhandl H., and Fischer F.D. Properties of random polycrystalline two-phase materials. *Applied Mechanics Reviews*, 47:231–240, 1994.

[21] Böhm H.J. and Han W. Comparisons between three-dimensional and two-dimensional multi-particle unit cell models for particle reinforced metal matrix composites. *Modelling and Simulation in Materials Science and Engineering*, 9:47–65, 2001.

[22] Böhm H.J., Eckschlager A., and Han W. Multi-inclusion unit cell models for metal matrix composites with randomly oriented discontinuous reinforcements. *Computational Materials Science*, 25:42–53, 2002.

[23] Ghosh S. and Moorthy S. Three dimensional Voronoi cell finite element model for microstructures with ellipsoidal heterogeneities. *Computational Mechanics*, 34:510–531, 2004.

[24] Shan Z. and Gokhale A.M. Micromechanics of complex three-dimensional microstructures. *Acta Materialia*, 49:2001–2015, 2001.

[25] Lee S.G., Gokhale A.M., and Sreeranganathan A. Reconstruction and visualization of complex 3D pore morphologies in a high pressure die cast magnesium alloy. *Materials Science and Engineering A*, 427:92–98, 2006.

[26] Suresh S., Mortensen A., and Needleman A. *Fundamentals of metal matrix composites*. Butterworth-Heinemann, 1993.

[27] Temizer I. and Wriggers P. On the computation of the macroscopic tangent for multiscale volumetric homogenization problems. *Computational Methods in Applied Mechanics and Engineering*, 198:495–510, 2008.

[28] Ghosh S., Lee K., and Moorthy S. Two scale analysis of heterogeneous elastic-plastic materials with asymptotic homogenization and Voronoi cell finite element model. *Computational Methods in Applied Mechanics and Engineering*, 132:63–116, 1996.

[29] Miehe C. and Bayreuther C. G. On multiscale fe analyses of heterogeneous structures: From homogenization to multigrid solvers. *International Journal for Numerical Methods in Engineering*, 71:1135–1180, 2007.

[30] Miehe C. Computational micro-to-macro transitions for discretized microstructures of heterogeneous materials at finite strains based on the minimization of averaged incremental energy. *Computer Methods in Applied Mechanics and Engineering*, 192:559–591, 2003.

[31] Ibrahimbegovic A. and Markovic D. Strong coupling methods in multi-phase and multi-scale modeling of inelastic behavior of heterogeneous structures. *Computer Methods in Applied Mechanics and Engineering*, 192:3089–3107, 2003.

[32] Bhadeshia H.K.D.H. Nickel based superalloys, accessed 15.11.2011. `http://www.msm.cam.ac.uk/phase-trans/2003/Superalloys/superalloys.html`.

[33] Hillier S. *Defect energies and deformation mechanisms of single crystal superalloys*. PhD thesis, University of Cambridge, 1984.

[34] Harada H. and Murakami H. Design of Ni-base superalloys. *Springer Series in Materials Science*, 34:39–70, 1999.

[35] Kattus J.R. Aerospace structural metals handbook, NiCo, MAR-M247. 1999.

[36] Haruna Y. Removal of inclusions from cast suparalloy revert. Master's thesis, University of British Columbia, 1994.

[37] Huang H.E. and Koo C.H. Characteristics and mechanical properties of polycrystalline CM 247 LC superalloy casting. *Materials Translations*, 45:562–568, 2004.

[38] Taylor P.R. An illustrated history of lost wax casting. *Proceedings of the 17th Annual BICTA Conference*, September 1983.

[39] Schlatter R. Vacuum induction melting. *Journals of Metals*, 5:17–25, 1972.

[40] Hasenhündl R., Presoly P., Schützenhöfer W., Tanzer R., Hildebrand F., and Reiter G. Vacuum induction melting: Optimisation of pressure dependent reactions. 2007.

[41] Beeley P. R. *Investment casting*. Institute of Materials, 1st edition, 1995.

[42] Fisher J. C. The fracture of liquids. *Journal of Applied Physics*, 19:1062–1067, 1948.

[43] Brillo J. and Egry I. Surface tension of nickel, copper, iron and their binary alloys. *Journal of Materials Science*, 40:2213–2216, 2005.

[44] Edelson B. I. and Baldwin W. M. The effect of second phases on the mechanical properties of alloys. Technical report, Department of Metallurgical Engineering Case Institute of Technology, 1959.

[45] Schumann H. and Oettel H. *Metallographie*, volume 13. Deutscher Verlag für Grundstoffindustrie Stuttgart, 1991.

[46] Vander Voort G.F. *Metallography principles and practice*. ASM International, 1999.

[47] Waters A. M. *Three-dimensional analysis of voids in AM60B magnesium tensile bars using computed tomography imagery*. PhD thesis, Johns Hopkins University, 2001.

[48] Salvo L., Cloetens P., Maire E., Zabler S., Blandin J.J., Buffiere J.Y., Ludwig W., Boller E., Bellet D., and Josserond C. X-ray micro-tomography an attractive characterisation technique in materials science. *Nuclear Instruments and Methods in Physics Research B*, 200:273–286, 2003.

[49] Heering W. Elektrophysik – Eine Einführung in die Quantenmechanik und Quantenstatistik. Lichttechnisches Institut, Universität Karlsruhe (TH), Lecture Notes, 2002.

[50] *Encyclopædia Britannica Online*, s. v. ”pair production”, accessed 14. 05. 2012. `http://www.britannica.com/EBchecked/topic/438692/pair-production`.

[51] Zeng G.L. Image reconstruction – A tutorial. *Computerized Medical Imaging and Graphics*, 25:97–103, 2001.

[52] Reimers W., Pyzalla A. R., Schreyer A., and Clemens H. *Neutrons and synchrotron radiation in engineering materials science*. Wiley-VCH Verlag GmbH & Co KGaA, 2008.

[53] Knoll G.F. *Radiation detection and measurement*. John Wiley & Sons, Inc., 1979.

[54] Smith W. *The scientist and engineer's guide to digital signal processing*. California Technical Publishing, 1997.

[55] You J. Image reconstruction from projections in tomography. Technical report, 2005.

[56] Kak A.C. *Image reconstruction from projection*, volume 2 of *Image Processing Techniques*, pages 111–169. Academic Press, Orlando, FL., 1984.

[57] Brownrigg D.R.K. The weighted median filter. *Communications of the ACM*, 27:807–818, 1984.

[58] *DIN 50 106: Prüfung Metallischer Werkstoffe – Druckversuch*, 1978.

[59] Ries M. *Experimentelle und Numerische Analyse von Porositäten in einer Nickelbasis-Guss-Superlegierung zur Prognose des Mechanischen Verhaltens*. PhD thesis, Technische Universität München, 2010.

[60] Clark J.P. and Evans F.C. Distance to nearest neighbor as a measure of spatial relationships in populations. *Ecology*, 35:445–453, 1954.

[61] Torquato S., Lu B., and Rubinstein J. Nearest-neighbor distribution function for systems of interacting particles. *Journal of Physics A: Mathematical and General*, 23:103–107, 1990.

[62] Ghosh S., Lee K., and Raghavean P. A multi-level computational model for mulit-scale damage analysis in composite and porous materials. *International Journal of Solid Structures*, 38:2335–3285, 2001.

[63] Antretter T., Pankensteiner A.F., Fischer F.D., and Rammerstorfer F.G. Multiscale modeling of highly heterogeneous MMCs. *ZAMM Zeitschrift für Angewandte Mathematik und Mechanik*, 79:128–130, 1999.

[64] Ostoja-Starzewski M. Material spatial randomness: From statistical to representative volume element. *Probabilistic Engineering Mechanics*, 21:112–132, 2006.

[65] Reinecker C. Mikromechanische Modellierung des Eigenschaftseinflusses von Gussporen in Ni-Superlegierungen. Technical report, Lehrstuhl für Werkstoffkunde und Werkstoffmechanik, 2009.

[66] Böhm H.J. A short introduction to basic aspects of continuum micromechnics. ILSB Report 206, 2008.

[67] Torquato S. *Random heterogeneous materials*, volume 16. Springer Science, 2001.

[68] Dassault Systems Simulia Corporation. *Abaqus Manuals, Version 6.10*, 2010.

[69] Gross D., Hauger W., Schnell W., and Wriggers P. *Technische Mechanik 4*. Springer Verlag Berlin Heidelberg New York, 1995.

[70] Temizer I. Micromechanics – Analysis of heterogeneous materials. Institute of Mechanics and Computational Mechanics, Leibnitz University of Hanover, Lecture Notes, 2007.

[71] Hill R. Elastic properties of reinforced solids: Some theoretical principles. *Jounal of the Mechanics and Physics of Solids*, 11:357–372, 1963.

[72] Ramberg W. and Osgood W.R. Description of stress strain curves by three parameters. Technical report, National Bureau of Standards, 1943.

[73] Lai W.M., Rubin D., and Krempl E. *Introduction to continuum mechanics*. Butterworth-Heinemann, 3rd edition, 1999.

[74] Rössler J., Harders H., and Bäker M. *Mechnisches Verhalten der Werkstoffe*. Vieweg + Teubner, 2008.

[75] Anderson T. L. *Fracture mechanics, fundamentals and application*. Taylor & Francis Group, 3rd edition, 2005.

[76] Griffith A.A. The phenomena of rupture and flow in solids. *Philosophical Transactions*, 221:163–198, 1920.

[77] Balzani D. Schröder J. and Brands D. FE^2-simulation of microheterogeneous steels based on statistically similar RVEs. In Hackl K., editor, *IUTAM Symposium on Variational Concepts with Applications to the Mechanics of Materials*, pages 15–28, 2010.

[78] Feyel F. A multilevel finite element method (FE^2) to describe the response of highly non-linear structures using generalized continua. *Computer Methods in Applied Mechanics and Engineering*, 192:3233–3244, 2003.

[79] Feyel F. and Chaboche J.L. FE^2 multiscale approach for modelling the elastoviscoplastic behaviour of long fibre SiC/Ti composite materials. *Computer Methods in Applied Mechanics and Engineering*, 183:309–3030, 1998.

[80] George E.D. *Mechanical metallurgy*. McGraw-Hill, 3rd edition, 1986.

[81] Höpcke W. *Fehlerlehre und Ausgleichsrechnung*. Walter de Gruyter & Co, 1980.

[82] Taxer T. and Werner E. Finite element modeling of porous nickel base cast alloys with representative volume elements. In *Simulia Customer Conference*, 2011.

[83] Lawrence J.D. *A catalog of special plane curves*. Dover Publications, New York, 1972.

[84] Lockwood E.H. *A book of curves*. Cambridge University Press, 1963.